Surface-Induced Decoherence and Heating of Charged Particles

Lukas Martinetz, Klaus Hornberger, and Benjamin A. Stickler*
University of Duisburg-Essen, Lotharstraße 1, 47048 Duisburg, Germany

(Received 7 April 2022; accepted 11 July 2022; published 24 August 2022)

Levitating charged particles in ultrahigh vacuum provides a preeminent platform for quantum information processing, for quantum-enhanced force and torque sensing, for probing physics beyond the standard model, and for high-mass tests of the quantum superposition principle. Existing setups, ranging from single atomic ions to ion chains and crystals to charged molecules and nanoparticles, are crucially impacted by fluctuating electric fields emanating from nearby electrodes used to control the motion. In this article, we provide a theoretical toolbox for describing the rotational and translational quantum dynamics of charged nano- to microscale objects near metallic and dielectric surfaces, as characterized by macroscopic dielectric response functions. The resulting quantum master equations describe the coherent surface-particle interaction, due to image charges and Casimir-Polder potentials, as well as surface-induced decoherence and heating, with the experimentally observed frequency and distance scaling. We explicitly evaluate the master equations for relevant setups, thereby providing the framework for describing and mitigating surface-induced decoherence as required in future quantum technological applications.

DOI: 10.1103/PRXQuantum.3.030327

I. INTRODUCTION

A. Quantum technologies with charged particles

Electrically charged, levitated objects are at the core of numerous cutting-edge quantum experiments and technologies. Atomic ions are amongst the most promising platforms for quantum computation and simulation [1,2]; trapped ion crystals act as ultraprecise sensors [3,4] and enable studies of novel quantum phases of matter [5,6]; charged molecules will enable encoding of quantum information [7–14], hold the prospects of state-controlled quantum chemistry [15–20], and allow probing the fundamental laws of nature [21–26]; electrically trapped microscale particles [27] can be cooled via embedded paramagnetic spins [28] or via electric feedback cooling [29–31], preparing future tests of quantum foundations [32–35].

Unlike atomic ions, molecules and nanoparticles possess higher charge moments so that the trapping fields can exert torques. Already the free quantum rotation dynamics of rigid bodies are intrinsically nonharmonic, rendering them attractive for quantum applications [36–38]. For instance, the rotation states of molecular ions have been proposed for quantum information processing [7,8,10,12,13,39,40], promising significant advantages in comparison to harmonic degrees of freedom due to the special topology of rotations in three dimensions [11]. At the same time, experiments with levitated nanorotors [41–51] reach millikelvin rotational temperatures [48,50,52], pointing the path towards ultraprecise torque sensors [41,43,44,46,47,49,51,53], the search for new physics [54], and tests of the quantum superposition principle with massive objects [52,55–58].

Controlling atomic, molecular, and nanoscale ions with electrodes and superconducting circuits [59–62] brings them close to metallic and dielectric surfaces. Thermally fluctuating charges and currents in the surface then unavoidably induce decoherence and motional heating of the trapped particle [10,63–66]. Given that building a quantum sensing device or a quantum computer will likely require chip-based miniaturization [65], the role of surface-induced heating and decoherence can be expected to become worse in future devices. This calls for a universal theoretical framework quantitatively describing charge-induced decoherence and heating close to surfaces, which points the way towards noise mitigation techniques.

B. Heating and decoherence by nearby surfaces

The experimental characterization of surface noise and decoherence relies on measuring heating rates and coherence times of trapped ions near the surface [2,65–71] and of interfering free electron beams traveling above a plane [72–74]. While different setups can exhibit distinct noise spectral densities, most experiments seem to agree

*benjamin.stickler@uni-due.de

on a characteristic inverse frequency scaling and on a proportionality to the fourth power of inverse distance [66]. That said, the microscopic origin of surface noise is still debated [2,65,66,71]. Theoretical models range from the damping of conduction electrons [75], the dissipative formation of image charges [76], the excitation of surface plasmons [77], to the fluctuations of surface-bound [78,79] or diffusing [80] adatoms, to patch potentials [81–84], and to thermally activated two-level adsorbates [85]. In an approach that does not require specifying a microscopic mechanism for surface-induced heating and decoherence, one may characterize the surface material solely by means of its dielectric response function [86–90].

This mechanism-independent approach can be formalized by using the framework of macroscopic quantum electrodynamics [91,92], which describes the quantum and thermal noise of the quantized electromagnetic field in terms of fluctuating bound charges and currents. This framework expresses the observable forces on the particle through empirically accessible response functions, while providing a versatile, i.e., nonmaterial-specific, description. Macroscopic quantum electrodynamics can reproduce the classical field fluctuations found above lossy dielectric layers [89,90,93], including the experimentally observed magnitude, distance, and frequency scaling [66]. This supports the theory that the noise originates from a thin surface layer. In addition, macroscopic quantum electrodynamics has been employed to quantitatively describe the decoherence of fast electrons [74,88], of spins [94], and of the center-of-mass motion of magnetic [95] and polarizable [96] spheres above surfaces.

Future quantum technologies will require a comprehensive framework to predict surface-induced heating and decoherence for arbitrary charge distributions and surface configurations, especially when utilizing molecules and nanoparticles in microtraps near electrodes and microstructured surfaces. We provide such a toolbox in the form of Lindblad master equations for the rotranslational quantum dynamics of arbitrarily charged particles in front of general dielectrics.

C. A framework of surface-induced decoherence

This article develops a theoretical framework to describe the quantum dynamics of charged objects near surfaces and uses it to derive quantum master equations for specific situations. These equations contain a coherent particle-surface potential, accounting for the formation of image charges and Casimir-Polder interactions, and a dissipator, describing surface-induced decoherence and heating. The latter serves to pinpoint the respective roles of the particle charge distribution, the surface geometry, temperature, and dielectric response for the ensuing decoherence and heating. Based on the general theory, we provide specific formulas for typical charge distributions, surface dielectric functions, and motion types. This includes the oscillation of monopoles, the libration of dipoles, and the rotation of quadrupoles above metallic and superconducting surfaces covered by thin dielectric layers, whose noise spectrum can decohere the particle motion either resonantly or off resonantly.

The chosen framework facilitates a pragmatic description of surface-induced decoherence and heating in terms of macroscopic dielectric response functions. The latter are accessible both by *in situ* and *ex situ* measurements as well as by microscopic *ab initio* calculations [97,98] and molecular-dynamics simulations [99]. By disentangling the effects of the surface geometry from the influence of the surface material, the derived master equations will be instrumental for the design of surfaces with favorable noise properties given a specific charge distribution and rotranslational motion. Our theoretical framework thus provides a bridge to device engineering and materials design to understand and mitigate surface noise, as required for the next generation of trapped-ion quantum devices [66]. In addition, we expect the here presented toolbox to be relevant for a variety of state-of-the art setups ranging from trapped ion quantum computers [66] to hybrid quantum devices with charged atoms or molecules [10] to nanoparticles in electric and optical traps for fundamental tests of physics [38]. Fully exhausting the technological potential of the latter requires a quantitative and unified understanding of surface noise, and our work presents a first step towards this goal.

The article is structured as follows. Section II summarizes the theoretical framework of surface-induced decoherence and presents the resulting master equations in their most generic form. The master equations are then specified in Secs. III and IV for typical charge distributions, for metallic, dielectric, and superconducting surfaces, and for planar and layered surface geometries. In Sec. V we discuss criteria for how the presented toolbox can be utilized, and we illustrate this with two examples. Finally, Sec. VI discusses possible future research directions and provides our conclusions. The technical details of the derivation are presented in Appendices A to C. Appendix D discusses the rotranslational decoherence due to elastic photon scattering (Thomson scattering).

II. SUMMARY OF MAIN RESULTS

A. Particle-surface coupling

We consider the motion of a particle of mass m and with moments of inertia I_1, I_2, I_3 moving in vacuum at center-of-mass position $\mathbf{R}$. The particle orientation Ω is specified by the rotation tensor R_Ω, relating the space-fixed axes $\mathbf{e}_i$ to the body-fixed principal axes $\mathbf{n}_i = \mathsf{R}_\Omega \mathbf{e}_i$, so that the inertia tensor is $\mathrm{I}_\Omega = \sum_i I_i \mathbf{n}_i \otimes \mathbf{n}_i$. The body carries a rigid charge distribution $\varrho(\mathbf{r}) = \varrho_0[\mathsf{R}_\Omega^{\mathrm{T}}(\mathbf{r} - \mathbf{R})]$, where ϱ_0 is the charge

distribution at the reference position $\mathbf{R} = 0$ and orientation $\mathsf{R}_\Omega = \mathbb{1}$.

The particle interacts with the fluctuating electromagnetic field emanating from a nearby surface; see Fig. 1. This field is due to thermal polarization currents in the surface material and can be expressed via the scalar and vector gauge potentials $\phi(\mathbf{r}, t)$ and $\mathbf{A}(\mathbf{r}, t)$. The resulting particle dynamics are described by the minimal coupling Hamiltonian

$$\begin{aligned} H = \frac{1}{2m}\left[\mathbf{P} - \int d^3r \varrho_0(\mathbf{r})\mathbf{A}\left(\mathbf{R} + \mathsf{R}_\Omega \mathbf{r}, t\right)\right]^2 \\ + \frac{1}{2}\left[\mathbf{J} - \int d^3r \varrho_0(\mathbf{r})\left(\mathsf{R}_\Omega \mathbf{r}\right) \times \mathbf{A}\left(\mathbf{R} + \mathsf{R}_\Omega \mathbf{r}, t\right)\right] \\ \cdot \mathrm{I}_\Omega^{-1}\left[\mathbf{J} - \int d^3r \varrho_0(\mathbf{r})\left(\mathsf{R}_\Omega \mathbf{r}\right) \times \mathbf{A}\left(\mathbf{R} + \mathsf{R}_\Omega \mathbf{r}, t\right)\right] \\ + \int d^3r \varrho_0(\mathbf{r})\phi(\mathbf{R} + \mathsf{R}_\Omega \mathbf{r}, t). \end{aligned} \tag{1}$$

Here, $\mathbf{P}$ and $\mathbf{J}$ are the canonical linear and angular momentum vectors. The canonical angular momentum vector is understood in terms of the canonical momentum coordinates p_Ω, conjugate to the orientation coordinates Ω; see Appendix A 1. (It is not identical to the kinetic angular momentum due to gauge coupling to the transverse field.)

Promoting the gauge fields to Heisenberg-picture operators, their dynamics can be described within the framework of *macroscopic quantum electrodynamics* [91,100]. This theory relates the gauge fields at position $\mathbf{r}$ to the quantized polarization currents $-i\omega\mathbf{P}_N(\mathbf{r}', \omega)$ at position $\mathbf{r}'$ and frequency ω, which fluctuate in the dielectric with complex-valued permittivity $\varepsilon_r(\mathbf{r}', \omega)$ (Appendix A 2). The polarization noise field is modeled by

$$\mathbf{P}_N(\mathbf{r}, \omega) = i\sqrt{4\pi\hbar\varepsilon_0 \operatorname{Im}[\varepsilon_r(\mathbf{r}, \omega)]}\mathbf{f}_e(\mathbf{r}, \omega) \tag{2}$$

with bosonic annihilation operators $\mathbf{f}_e(\mathbf{r}, \omega)$, which are from now on dubbed polarization oscillators. They satisfy the standard (dyadic) canonical commutation relations [91], e.g.,

$$[\mathbf{f}_e(\mathbf{r}, \omega), \mathbf{f}_e^\dagger(\mathbf{r}', \omega')] = \mathbb{1}\delta(\mathbf{r} - \mathbf{r}')\delta(\omega - \omega'). \tag{3}$$

In the following, we assume that the oscillators are always in a thermal state characterized by the surface temperature T, so that

$$\langle \mathbf{f}_e^\dagger(\mathbf{r}, \omega) \otimes \mathbf{f}_e(\mathbf{r}', \omega')\rangle = n(\omega)\delta(\mathbf{r} - \mathbf{r}')\delta(\omega - \omega')\mathbb{1}, \tag{4}$$

with the Bose-Einstein occupation factor $n(\omega) = 1/[\exp(\hbar\omega/k_B T) - 1]$.

The polarization noise field (2) induces an electromagnetic field at the particle position, as given by Maxwell's

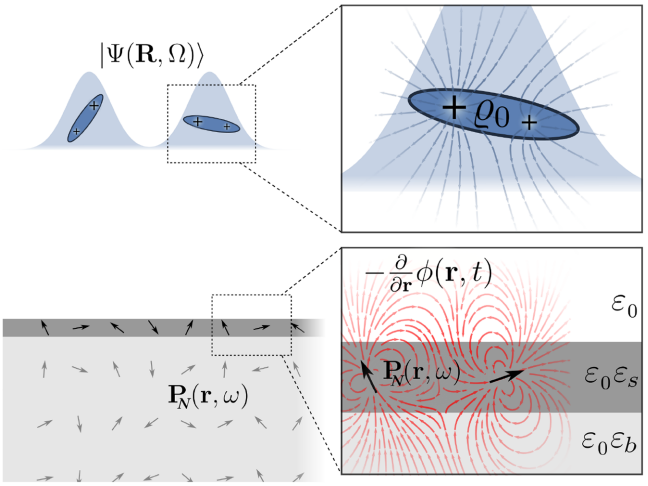

FIG. 1. A charged particle (blue) with charge distribution ϱ_0 evolving in a spatio-orientational superposition state $|\Psi(\mathbf{R}, \Omega)\rangle$ will suffer from motional decoherence due to electric fields (red lines) originating from a fluctuating polarization (black arrows) in nearby metallic or dielectric surfaces. The fluctuation strength of the polarization at a position $\mathbf{r}$ depends on the dielectric material response $\varepsilon_0\varepsilon_r(\mathbf{r}, \omega)$ and the temperature T. For small distances, the electric field propagates quasistatically from each fluctuation to the particle, as can be described by a scalar potential $\phi(\mathbf{r}, t)$. A layered dielectric consisting of a surface layer with $\varepsilon_0\varepsilon_s(\omega)$ and a bulk dielectric with $\varepsilon_0\varepsilon_b(\omega)$ can explain the noise levels and scalings measured in ion traps [89].

equations. In most experimental setups, this field is well approximated by its longitudinal part, and therefore described by a quasistatic scalar Green function (Appendix C)

$$\frac{\partial}{\partial \mathbf{r}} \cdot \left[\varepsilon_0\varepsilon_r(\mathbf{r}, \omega)\frac{\partial}{\partial \mathbf{r}}g(\mathbf{r}, \mathbf{r}', \omega)\right] = -\delta(\mathbf{r} - \mathbf{r}'). \tag{5}$$

The Green function $g(\mathbf{r}, \mathbf{r}', \omega)$ determines the electrostatic potential at $\mathbf{r}$ of a charge oscillating in magnitude with frequency ω at position $\mathbf{r}'$ in the presence of a dielectric. This Green function fulfills the relation

$$\begin{aligned} \operatorname{Im}[g(\mathbf{r}, \mathbf{r}', \omega)] = -\varepsilon_0 \int d^3s \operatorname{Im}[\varepsilon_r(\mathbf{s}, \omega)]\left[\frac{\partial}{\partial \mathbf{s}}g(\mathbf{r}, \mathbf{s}, \omega)\right] \\ \cdot \left[\frac{\partial}{\partial \mathbf{s}}g^*(\mathbf{s}, \mathbf{r}', \omega)\right], \end{aligned} \tag{6}$$

which will be useful in the following. In Appendix C we derive this relation together with further properties of $g(\mathbf{r}, \mathbf{r}', \omega)$.

In the quasistatic approximation (C5) the vector potential vanishes in Coulomb gauge so that the particle-surface interaction is determined by the operator-valued scalar

potential

$$\phi(\mathbf{r},t) = i\sqrt{\frac{\varepsilon_0\hbar}{\pi}}\int d^3r' \int_0^\infty d\omega \sqrt{\mathrm{Im}[\varepsilon_r(\mathbf{r}',\omega)]}e^{-i\omega t} \times \mathbf{f}_e(\mathbf{r}',\omega)\cdot\frac{\partial}{\partial \mathbf{r}'}g(\mathbf{r},\mathbf{r}',\omega) + \mathrm{H.c.}, \tag{7}$$

where $\mathrm{Im}[\varepsilon_r(\mathbf{r},\omega)] \geq 0$ for positive frequencies [91]. The hermitian Heisenberg-picture operator (7) acts on the Hilbert space of the polarization oscillators.

Having specified how the particle-field coupling Hamiltonian relates to the surface noise, one can obtain the reduced quantum dynamics of the particle by tracing out the field dynamics in the weak-coupling approximation [101]. This requires calculating the spectral density

$$\mathsf{J}(\mathbf{s},\mathbf{s}',\omega) = -\frac{1}{\pi}\frac{\partial}{\partial \mathbf{s}}\otimes\frac{\partial}{\partial \mathbf{s}'}\,\mathrm{Im}[g(\mathbf{s},\mathbf{s}',\omega)], \tag{8}$$

which specifies the tensorial autocorrelation of the surface contribution to Eq. (7) (see Appendix B) in terms of the dissipation kernel

$$\mathsf{D}(\mathbf{s},\mathbf{s}',\tau) = \frac{2\hbar}{(4\pi)^2}\int_0^\infty d\omega \mathsf{J}(\mathbf{s},\mathbf{s}',\omega)\sin(\omega\tau) \tag{9}$$

and the noise kernel

$$\mathsf{N}(\mathbf{s},\mathbf{s}',\tau) = \frac{2\hbar}{(4\pi)^2}\int_0^\infty d\omega \mathsf{J}(\mathbf{s},\mathbf{s}',\omega)\coth\left(\frac{\hbar\omega}{2k_BT}\right)\cos(\omega\tau). \tag{10}$$

These kernels determine the timescale on which surface-fluctuation correlations decay, which will be relevant in the following.

For realistic experimental situations, the weak-coupling Born-Markov approximation is justified (Sec. V B). The resulting quantum master equation depends on the relation of the involved timescales. We start with the *slow-particle limit* before discussing the case of *resonant motion*.

B. Slow-particle motion

In the slow-particle limit, the surface-free particle dynamics due to the Hamiltonian H_0 and the surface-induced particle dynamics are much slower than the surface-fluctuation correlation time. As shown in Appendix B 2, the resulting master equation

$$\frac{\partial\rho}{\partial t} = -\frac{i}{\hbar}[H_0 + H_{\mathrm{SI}},\rho] + \mathcal{L}\rho \tag{11}$$

takes Lindblad form

$$\mathcal{L}\rho = \frac{\varepsilon_0}{\hbar}\lim_{\omega\downarrow 0}\frac{2k_BT}{\hbar\omega}\int d^3r\frac{\mathrm{Im}[\varepsilon_r(\mathbf{r},\omega)]}{|\varepsilon_r(\mathbf{r},\omega)|^2} \times\left(\mathbf{L}_e(\mathbf{r})\cdot\rho\mathbf{L}_e^\dagger(\mathbf{r}) - \frac{1}{2}\{\mathbf{L}_e^\dagger(\mathbf{r})\cdot\mathbf{L}_e(\mathbf{r}),\rho\}\right) \tag{12}$$

with Lindblad operators

$$\mathbf{L}_e(\mathbf{r}) = \int d^3s\varrho_0[\mathsf{R}_\Omega^{\mathrm{T}}(\mathbf{s}-\mathbf{R})]\lim_{\omega\downarrow 0}\varepsilon_r(\mathbf{r},\omega)\frac{\partial}{\partial\mathbf{r}}g(\mathbf{r},\mathbf{s},\omega). \tag{13}$$

The limit is taken from above because $\mathrm{Im}[\varepsilon_r(\mathbf{r},\omega)]$ can exhibit a discontinuity at $\omega = 0$ due to the Schwarz reflection principle. The surface-interaction Hamiltonian H_{SI} describes the coherent interaction with image charges in the dielectric,

$$H_{\mathrm{SI}} = \frac{1}{2}\int d^3r d^3r'\, g(\mathbf{r},\mathbf{r}',0)\varrho_0[\mathsf{R}_\Omega^{\mathrm{T}}(\mathbf{r}-\mathbf{R})] \times\varrho_0[\mathsf{R}_\Omega^{\mathrm{T}}(\mathbf{r}'-\mathbf{R})]. \tag{14}$$

Equations (11)–(13) describe rotranslational decoherence and heating in terms of (i) the dielectric properties of the surface material, (ii) the surface geometry, and (iii) the particle charge distribution. As one expects, only the dielectric regions of space, where $\mathrm{Im}[\varepsilon_r(\mathbf{r},\omega)] > 0$, contribute to the integral in Eq. (12). Note that the form (13) implies that the Lindblad operators correspond to the (negative) displacement field induced by the particle charge distribution located at position $\mathbf{R}$ and orientation Ω.

Using relation (6), one can disentangle the contributions of charge distribution and surface properties by showing that (Appendix B 2)

$$\mathcal{L}\rho = \frac{2}{\hbar}\int d^3r d^3r' h(\mathbf{r},\mathbf{r}') \times\left(\varrho_0[\mathsf{R}_\Omega^{\mathrm{T}}(\mathbf{r}-\mathbf{R})]\rho\varrho_0[\mathsf{R}_\Omega^{\mathrm{T}}(\mathbf{r}'-\mathbf{R})] - \frac{1}{2}\{\varrho_0[\mathsf{R}_\Omega^{\mathrm{T}}(\mathbf{r}'-\mathbf{R})]\varrho_0[\mathsf{R}_\Omega^{\mathrm{T}}(\mathbf{r}-\mathbf{R})],\rho\}\right). \tag{15}$$

Here, the surface geometry and response function enter through the *surface-fluctuation kernel*

$$h(\mathbf{r},\mathbf{r}') = -\lim_{\omega\downarrow 0} n(\omega)\,\mathrm{Im}[g(\mathbf{r},\mathbf{r}',\omega)]. \tag{16}$$

The particle charge distribution takes the role of the Lindblad operators, leading to a localization in position and

orientation. The decoherence rate in this basis, defined via

$$\langle \mathbf{R}, \Omega | \, \mathcal{L}\rho \, | \mathbf{R}', \Omega' \rangle = -\Gamma_{\Omega\Omega'}(\mathbf{R}, \mathbf{R}') \, \langle \mathbf{R}, \Omega | \, \rho \, | \mathbf{R}', \Omega' \rangle \, , \tag{17}$$

takes the form

$$\begin{aligned}\Gamma_{\Omega\Omega'}(\mathbf{R}, \mathbf{R}') = \frac{1}{\hbar} \int d^3r d^3r' \, h(\mathbf{r}, \mathbf{r}') \big(& \varrho_0[\mathsf{R}^{\mathrm{T}}_{\Omega}(\mathbf{r} - \mathbf{R})] \\ & - \varrho_0[\mathsf{R}^{\mathrm{T}}_{\Omega'}(\mathbf{r} - \mathbf{R}')] \big) \\ & \times \big(\varrho_0[\mathsf{R}^{\mathrm{T}}_{\Omega}(\mathbf{r}' - \mathbf{R})] - \varrho_0[\mathsf{R}^{\mathrm{T}}_{\Omega'}(\mathbf{r}' - \mathbf{R}')] \big),\end{aligned} \tag{18}$$

where we have used $g(\mathbf{r}, \mathbf{r}', \omega) = g(\mathbf{r}', \mathbf{r}, \omega)$ (see Appendix C 2).

The decoherence rate is non-negative, as follows from Eq. (6), it vanishes for $\mathbf{R} = \mathbf{R}'$ and $\Omega = \Omega'$, and remains bounded for large lateral superposition sizes. It thus describes how superposition states of the charged particle gradually lose coherence due to their interactions with surface charge fluctuations.

The Lindblad operators are specified in Sec. III for common charge distributions, while the form of the surface-fluctuation kernel (16) is discussed in Sec. IV for typical surface geometries and generic material responses. Table I summarizes the master equations for particles characterized by their first multipole moments and for typical types of particle motion. Table II gives the surface-fluctuation kernel for a half-space and a layered surface geometry.

C. Resonant motion

The resonant limit applies if both the free particle motion and the decay of surface-fluctuation correlations are much faster than the surface-induced particle dynamics. The resulting master equation can be stated by diagonalizing the surface-free particle dynamics,

$$\begin{aligned}H_0 &= \frac{\mathbf{P}^2}{2m} + \frac{1}{2}\mathbf{J} \cdot \mathrm{I}_{\Omega}^{-1}\mathbf{J} + V_{\mathrm{ext}}(\mathbf{R}, \Omega) \\ &= \sum_n E_n |\Psi_n\rangle\langle\Psi_n|,\end{aligned} \tag{19}$$

including a possible external trapping potential V_{ext}. This allows expanding the particle charge density by means of the operators

$$c_\ell(\mathbf{r}) = \sum_{\substack{n,m \\ E_m - E_n = \hbar\omega_\ell > 0}} c_{nm}(\mathbf{r}) \, |\Psi_n\rangle \, \langle\Psi_m| \tag{20}$$

with coefficients

$$c_{nm}(\mathbf{r}) = \langle \Psi_n | \, \varrho_0[\mathsf{R}^{\mathrm{T}}_{\Omega}(\mathbf{r} - \mathbf{R})] \, | \Psi_m \rangle \, , \tag{21}$$

where ω_ℓ labels the level spacings of H_0.

A rotating-wave approximation of the interaction Hamiltonian with respect to the particle dynamics yields a dissipator of Lindblad form (Appendix B 3),

$$\begin{aligned}\mathcal{L}\rho = \frac{\varepsilon_0}{\hbar} \sum_{\omega_\ell > 0} \int d^3r \frac{\mathrm{Im}[\varepsilon_r(\mathbf{r}, \omega_\ell)]}{|\varepsilon_r(\mathbf{r}, \omega_\ell)|^2} \Big[& [n(\omega_\ell) + 1] \\ & \times \left(\mathbf{L}^e_\ell(\mathbf{r}) \cdot \rho \mathbf{L}^{e\dagger}_\ell(\mathbf{r}) - \frac{1}{2}\{\mathbf{L}^{e\dagger}_\ell(\mathbf{r}) \cdot \mathbf{L}^e_\ell(\mathbf{r}), \rho\} \right) \\ & + n(\omega_\ell) \left(\mathbf{L}^{e\dagger}_\ell(\mathbf{r}) \cdot \rho \mathbf{L}^e_\ell(\mathbf{r}) - \frac{1}{2}\{\mathbf{L}^e_\ell(\mathbf{r}) \cdot \mathbf{L}^{e\dagger}_\ell(\mathbf{r}), \rho\} \right) \Big]\end{aligned} \tag{22}$$

with

$$\mathbf{L}^e_\ell(\mathbf{r}) = \sqrt{2} \int d^3s \, c_\ell(\mathbf{s}) \varepsilon_r(\mathbf{r}, \omega_\ell) \frac{\partial}{\partial \mathbf{r}} g(\mathbf{r}, \mathbf{s}, \omega_\ell). \tag{23}$$

The Lindblad operators thus describe the displacement field smeared out over the field-free motion of the charged particle.

Only the dielectric regions contribute to the integral in the master equation (22). The latter describes resonant transitions between the particle motion (19) and the dielectric, as weighted by the energy loss function $\mathrm{Im}[\varepsilon_r(\mathbf{r}, \omega_\ell)]/|\varepsilon_r(\mathbf{r}, \omega_\ell)|^2$. The first term in Eq. (22) accounts for spontaneous and stimulated deexcitation of the particle motion; the second term accounts for surface-induced excitations of the particle dynamics. This leads to heating, damping, and thermalization of the particle motion with the surface temperature.

The associated surface-interaction Hamiltonian (Lamb shift) in the zero-temperature limit reads

$$\begin{aligned}H_{\mathrm{SI}} = \frac{1}{2} \int d^3r d^3r' \sum_{\omega_\ell > 0} \Big(& \mathrm{Re}[g(\mathbf{r}, \mathbf{r}', \omega_\ell)] - \frac{1}{4\pi\varepsilon_0} \frac{1}{|\mathbf{r} - \mathbf{r}'|} \Big) \\ & \times \{c^\dagger_\ell(\mathbf{r}), c_\ell(\mathbf{r}')\} + \int d^3r d^3r' \sum_{\omega_\ell > 0} \frac{\omega_\ell}{\pi} \mathsf{P} \int_0^\infty d\omega \\ & \times \frac{\mathrm{Im}\left[g(\mathbf{r}, \mathbf{r}', \omega)\right]}{\omega^2 - \omega_\ell^2} [c^\dagger_\ell(\mathbf{r}), c_\ell(\mathbf{r}')].\end{aligned} \tag{24}$$

It contains two contributions. The first accounts for the interaction of the particle charge distribution with the particle-induced surface polarization—i.e., the image-charge potential (see Appendix B 3). The second contribution describes modifications of the particle dynamics induced by zero-point fluctuations in the surface, similar to the Casimir-Polder potential.

TABLE I. Selection of quantum master equations for typical charge distributions and types of motion; see Sec. III. The prefactors in lines *a*, *b*, and *c* are special cases of the spatio-orientational decoherence rate (18).

	Illustration	Dissipator
a	*Slow monopole* 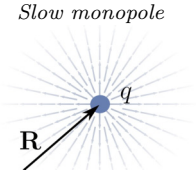	$\langle \mathbf{R},\Omega\vert\mathcal{L}\rho\vert\mathbf{R}',\Omega'\rangle = -\frac{q^2}{\hbar}[h(\mathbf{R},\mathbf{R})+h(\mathbf{R}',\mathbf{R}')-2h(\mathbf{R},\mathbf{R}')]\langle\mathbf{R},\Omega\vert\rho\vert\mathbf{R}',\Omega'\rangle$ with $h(\mathbf{R},\mathbf{R}') = -\lim_{\omega\downarrow 0} n(\omega)\,\mathrm{Im}[g(\mathbf{R},\mathbf{R}',\omega)]$
b	*Slow dipole* 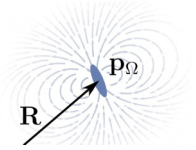	$\langle \mathbf{R},\Omega\vert\mathcal{L}\rho\vert\mathbf{R}',\Omega'\rangle = -\frac{1}{\hbar}\left[h^{(2)}_{\Omega\Omega}(\mathbf{R},\mathbf{R})+h^{(2)}_{\Omega'\Omega'}(\mathbf{R}',\mathbf{R}')-2h^{(2)}_{\Omega\Omega'}(\mathbf{R},\mathbf{R}')\right]\langle\mathbf{R},\Omega\vert\rho\vert\mathbf{R}',\Omega'\rangle$ with $h^{(2)}_{\Omega\Omega'}(\mathbf{R},\mathbf{R}') = \left(\mathbf{p}_\Omega\cdot\frac{\partial}{\partial\mathbf{R}}\right)\left(\mathbf{p}_{\Omega'}\cdot\frac{\partial}{\partial\mathbf{R}'}\right)h(\mathbf{R},\mathbf{R}')$
c	*Slow quadrupole* 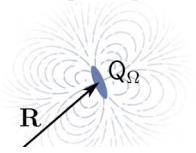	$\langle \mathbf{R},\Omega\vert\mathcal{L}\rho\vert\mathbf{R}',\Omega'\rangle = -\frac{1}{\hbar}\left[h^{(4)}_{\Omega\Omega}(\mathbf{R},\mathbf{R})+h^{(4)}_{\Omega'\Omega'}(\mathbf{R}',\mathbf{R}')-2h^{(4)}_{\Omega\Omega'}(\mathbf{R},\mathbf{R}')\right]\langle\mathbf{R},\Omega\vert\rho\vert\mathbf{R}',\Omega'\rangle$ with $h^{(4)}_{\Omega\Omega'}(\mathbf{R},\mathbf{R}') = \frac{1}{36}\left(\frac{\partial}{\partial\mathbf{R}}\cdot\mathsf{Q}_\Omega\frac{\partial}{\partial\mathbf{R}}\right)\left(\frac{\partial}{\partial\mathbf{R}'}\cdot\mathsf{Q}_{\Omega'}\frac{\partial}{\partial\mathbf{R}'}\right)h(\mathbf{R},\mathbf{R}')$
d	*Oscillating monopole* 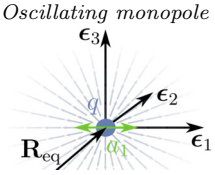	$\mathcal{L}\rho = \sum_{k=1,2,3}\frac{q^2}{m\omega_k}h_k(\mathbf{R}_{\mathrm{eq}})\left[[n(\omega_k)+1]\left(a_k\rho a_k^\dagger-\frac{1}{2}\left\{a_k^\dagger a_k,\rho\right\}\right)+n(\omega_k)\left(a_k^\dagger\rho a_k-\frac{1}{2}\left\{a_k a_k^\dagger,\rho\right\}\right)\right]$ with $h_k(\mathbf{R}_{\mathrm{eq}}) = -\left(\boldsymbol{\epsilon}_k\cdot\frac{\partial}{\partial\mathbf{r}}\right)\left(\boldsymbol{\epsilon}_k\cdot\frac{\partial}{\partial\mathbf{r}'}\right)\mathrm{Im}\left[g(\mathbf{r},\mathbf{r}',\omega_k)\right]\Big\vert_{\mathbf{r}=\mathbf{r}'=\mathbf{R}_{\mathrm{eq}}}$
e	*Oscillating dipole* 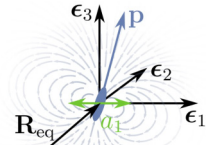	$\mathcal{L}\rho = \sum_{k=1,2,3}\frac{1}{m\omega_k}h_k(\mathbf{R}_{\mathrm{eq}})\left[[n(\omega_k)+1]\left(a_k\rho a_k^\dagger-\frac{1}{2}\{a_k^\dagger a_k,\rho\}\right)+n(\omega_k)\left(a_k^\dagger\rho a_k-\frac{1}{2}\{a_k a_k^\dagger,\rho\}\right)\right]$ with $h_k(\mathbf{R}_{\mathrm{eq}}) = -\left(\boldsymbol{\epsilon}_k\cdot\frac{\partial}{\partial\mathbf{r}}\right)\left(\boldsymbol{\epsilon}_k\cdot\frac{\partial}{\partial\mathbf{r}'}\right)\left(\mathbf{p}\cdot\frac{\partial}{\partial\mathbf{r}}\right)\left(\mathbf{p}\cdot\frac{\partial}{\partial\mathbf{r}'}\right)\mathrm{Im}[g(\mathbf{r},\mathbf{r}',\omega_k)]\Big\vert_{\mathbf{r}=\mathbf{r}'=\mathbf{R}_{\mathrm{eq}}}$
f	*Oscillating quadrupole* 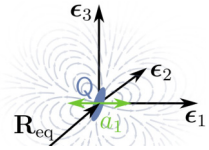	$\mathcal{L}\rho = \sum_{k=1,2,3}\frac{1}{36m\omega_k}h_k(\mathbf{R}_{\mathrm{eq}})\left[[n(\omega_k)+1]\left(a_k\rho a_k^\dagger-\frac{1}{2}\{a_k^\dagger a_k,\rho\}\right)+n(\omega_k)\left(a_k^\dagger\rho a_k-\frac{1}{2}\{a_k a_k^\dagger,\rho\}\right)\right]$ with $h_k(\mathbf{R}_{\mathrm{eq}}) = -\left(\boldsymbol{\epsilon}_k\cdot\frac{\partial}{\partial\mathbf{r}}\right)\left(\boldsymbol{\epsilon}_k\cdot\frac{\partial}{\partial\mathbf{r}'}\right)\left(\frac{\partial}{\partial\mathbf{r}}\cdot\mathsf{Q}\frac{\partial}{\partial\mathbf{r}}\right)\left(\frac{\partial}{\partial\mathbf{r}'}\cdot\mathsf{Q}\frac{\partial}{\partial\mathbf{r}'}\right)\mathrm{Im}[g(\mathbf{r},\mathbf{r}',\omega_k)]\Big\vert_{\mathbf{r}=\mathbf{r}'=\mathbf{R}_{\mathrm{eq}}}$
g	*Librating dipole* 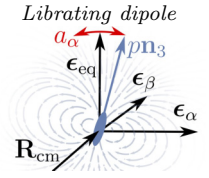	$\mathcal{L}\rho = \sum_{\ell=\alpha,\beta}\frac{p^2}{I\omega_\ell}h_\ell(\mathbf{R}_{\mathrm{cm}})\left[[n(\omega_\ell)+1]\left(a_\ell\rho a_\ell^\dagger-\frac{1}{2}\{a_\ell^\dagger a_\ell,\rho\}\right)+n(\omega_\ell)\left(a_\ell^\dagger\rho a_\ell-\frac{1}{2}\left\{a_\ell a_\ell^\dagger,\rho\right\}\right)\right]$ with $h_\ell(\mathbf{R}_{\mathrm{cm}}) = -\left(\boldsymbol{\epsilon}_\ell\cdot\frac{\partial}{\partial\mathbf{r}}\right)\left(\boldsymbol{\epsilon}_\ell\cdot\frac{\partial}{\partial\mathbf{r}'}\right)\mathrm{Im}[g(\mathbf{r},\mathbf{r}',\omega_\ell)]\Big\vert_{\mathbf{r}=\mathbf{r}'=\mathbf{R}_{\mathrm{cm}}}$
h	*Librating quadrupole* 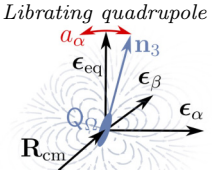	$\mathcal{L}\rho = \sum_{\ell=\alpha,\beta}\frac{Q_{33}^2}{4I\omega_\ell}h_\ell(\mathbf{R}_{\mathrm{cm}})\left[[n(\omega_\ell)+1]\left(a_\ell\rho a_\ell^\dagger-\frac{1}{2}\{a_\ell^\dagger a_\ell,\rho\}\right)+n(\omega_\ell)\left(a_\ell^\dagger\rho a_\ell-\frac{1}{2}\{a_\ell a_\ell^\dagger,\rho\}\right)\right]$ with $h_\ell(\mathbf{R}_{\mathrm{cm}}) = -\left(\boldsymbol{\epsilon}_\ell\cdot\frac{\partial}{\partial\mathbf{r}}\right)\left(\boldsymbol{\epsilon}_\ell\cdot\frac{\partial}{\partial\mathbf{r}'}\right)\left(\boldsymbol{\epsilon}_{\mathrm{eq}}\cdot\frac{\partial}{\partial\mathbf{r}}\right)\left(\boldsymbol{\epsilon}_{\mathrm{eq}}\cdot\frac{\partial}{\partial\mathbf{r}'}\right)\mathrm{Im}[g(\mathbf{r},\mathbf{r}',\omega_\ell)]\Big\vert_{\mathbf{r}=\mathbf{r}'=\mathbf{R}_{\mathrm{cm}}}$

TABLE I. (Continued)

i	*Rotating dipole* 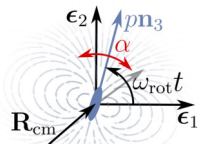	$\mathcal{L}\rho = \sum_{\ell=1,2} \frac{p^2}{2\hbar} h_\ell(\mathbf{R}_{\rm cm}, \omega_{\rm rot}) \left[[n(\omega_{\rm rot})+1](e^{-i\alpha}\rho e^{i\alpha} - \rho) + n(\omega_{\rm rot})(e^{i\alpha}\rho e^{-i\alpha} - \rho)\right]$ with $h_\ell(\mathbf{R}_{\rm cm}, \omega_{\rm rot}) = -\left(\boldsymbol{\epsilon}_\ell \cdot \frac{\partial}{\partial \mathbf{r}}\right)\left(\boldsymbol{\epsilon}_\ell \cdot \frac{\partial}{\partial \mathbf{r}'}\right) \mathrm{Im}[g(\mathbf{r}, \mathbf{r}', \omega_{\rm rot})]\Big\|_{\mathbf{r}=\mathbf{r}'=\mathbf{R}_{\rm cm}}$
j	*Rotating quadrupole* 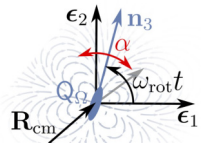	$\mathcal{L}\rho = \frac{Q_{33}^2}{128\hbar} h_{12}(\mathbf{R}_{\rm cm}) \left[[n(\omega_{\rm rot})+1](e^{-2i\alpha}\rho e^{2i\alpha} - \rho) + n(\omega_{\rm rot})(e^{2i\alpha}\rho e^{-2i\alpha} - \rho)\right]$ with $h_{12}(\mathbf{R}_{\rm cm}) = -\left[(\boldsymbol{\epsilon}_1 - i\boldsymbol{\epsilon}_2)\cdot\frac{\partial}{\partial \mathbf{r}}\right]^2 \left[(\boldsymbol{\epsilon}_1 + i\boldsymbol{\epsilon}_2)\cdot\frac{\partial}{\partial \mathbf{r}'}\right]^2 \mathrm{Im}[g(\mathbf{r}, \mathbf{r}', \omega_{\rm rot})]\Big\|_{\mathbf{r}=\mathbf{r}'=\mathbf{R}_{\rm cm}}$

One can again disentangle the contribution of particle and surface properties by using Eq. (6). This yields

$$\mathcal{L}\rho = -\frac{2}{\hbar}\int d^3r d^3r' \sum_{\omega_\ell>0} \mathrm{Im}[g(\mathbf{r}, \mathbf{r}', \omega_\ell)]\Big[[n(\omega_\ell)+1] \times \left(c_\ell(\mathbf{r}')\rho c_\ell^\dagger(\mathbf{r}) - \frac{1}{2}\{c_\ell^\dagger(\mathbf{r})c_\ell(\mathbf{r}'), \rho\}\right) + n(\omega_\ell)\left(c_\ell^\dagger(\mathbf{r})\rho c_\ell(\mathbf{r}') - \frac{1}{2}\{c_\ell(\mathbf{r}')c_\ell^\dagger(\mathbf{r}), \rho\}\right)\Big], \tag{25}$$

where the surface properties now enter through the imaginary part of the Green function in Eq. (5), evaluated on resonance with the particle motion. The Lindblad operators $c_\ell(\mathbf{r})$ are fully specified by the particle charge distribution ϱ_0 and the field-free Hamiltonian H_0, implying that the integrands in Eq. (25) are localized within the smeared-out charge distribution.

The form of these Lindblad operators is discussed in Sec. III for typical charge distributions. The *resonant surface-fluctuation kernel* $\mathrm{Im}[g(\mathbf{r}, \mathbf{r}', \omega_\ell)]$ of typical surface geometries and generic material responses is then specified in Sec. IV, and Sec. V discusses the resulting heating and decoherence rates for state-of-the-art setups. Master equations for typical charge distributions and types of motion are illustrated in Table I. The resonant surface-fluctuation kernel is given in Table II for a half-space and a layered surface geometry.

III. LINDBLAD OPERATORS FOR CHARGE MULTIPOLES

In the master equations (15) and (25) the particle properties, entering through the Lindblad operators, are separated from the dielectric surface, entering through the surface-fluctuation kernel. In the slow-particle limit, only the instantaneous charge distribution appears, while the resonant limit blurs the charge over the fast particle motion, as described by the operators $c_\ell(\mathbf{s})$. This section gives the Lindblad operators for typical experimental setups. The resulting master equations are provided in Table I.

A. Slow-particle motion

a. Slow monopole.—The Lindblad operator of a point monopole with total charge q at position $\mathbf{r}$ is independent of the particle orientation,

$$\varrho_0[\mathsf{R}_\Omega^{\rm T}(\mathbf{r} - \mathbf{R})] = q\delta(\mathbf{r} - \mathbf{R}). \tag{26}$$

b. Slow dipole.—A point particle with a body-fixed dipole moment $\mathbf{p}_0$, but no other multipoles, is characterized by $\varrho_0(\mathbf{r}) = -\mathbf{p}_0 \cdot \partial_{\mathbf{r}}\delta(\mathbf{r})$, yielding the Lindblad operator

$$\varrho_0[\mathsf{R}_\Omega^{\rm T}(\mathbf{r} - \mathbf{R})] = -(\mathsf{R}_\Omega\mathbf{p}_0)\cdot\frac{\partial}{\partial \mathbf{r}}\delta(\mathbf{r} - \mathbf{R}), \tag{27}$$

which involves the orientation state-dependent dipole vector $\mathbf{p}_\Omega = \mathsf{R}_\Omega\mathbf{p}_0$. After inserting Eq. (27) into the master equation (15), the spatial derivatives of the δ distributions can be shifted to $h(\mathbf{r}, \mathbf{r}')$ by partial integration.

c. Slow quadrupole.—A point particle with a body-fixed quadrupole tensor Q_0, but no other multipoles, is characterized by $\varrho_0(\mathbf{r}) = \partial_{\mathbf{r}} \cdot \mathsf{Q}_0\partial_{\mathbf{r}}\delta(\mathbf{r})/6$, leading to the Lindblad operators

$$\varrho_0[\mathsf{R}_\Omega^{\rm T}(\mathbf{r} - \mathbf{R})] = \frac{1}{6}\frac{\partial}{\partial \mathbf{r}} \cdot \mathsf{R}_\Omega\mathsf{Q}_0\mathsf{R}_\Omega^{\rm T}\frac{\partial}{\partial \mathbf{r}}\delta(\mathbf{r} - \mathbf{R}). \tag{28}$$

Similar to the case of a slow dipole, the Liouvillan (15) depends on the orientation state-dependent quadrupole tensor $\mathsf{Q}_\Omega = \mathsf{R}_\Omega\mathsf{Q}_0\mathsf{R}_\Omega^{\rm T}$ and the Hessian of $h(\mathbf{r}, \mathbf{r}')$ at the particle position.

General charge distribution.—The dissipator for a particle with a charge distribution characterized by several multipole moments is not simply obtained by adding the

TABLE II. The resonant surface-fluctuation kernel for particles in front of a homogeneous planar surface (top) and a planar surface covered by a dielectric layer (bottom). For the latter case, we assume the particle to be at a large distance from the surface, $\mathbf{r}\cdot\mathbf{e}_3, \mathbf{r}'\cdot\mathbf{e}_3 \ll d_s$, as described in Sec. IV. In both expressions $\mathbf{r}$ and $\mathbf{r}'$ are evaluated in vacuum, and the mirror tensor $\mathsf{M} = \mathbb{1} - 2\mathbf{e}_3\otimes\mathbf{e}_3$ serves to reflect a vector at the surface plane.

Illustration	Surface-fluctuation kernel
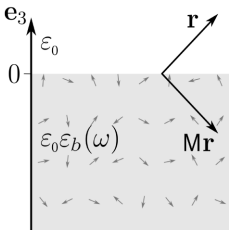	$\mathrm{Im}[g(\mathbf{r},\mathbf{r}',\omega)] = -\frac{2}{4\pi\varepsilon_0}\frac{\mathrm{Im}[\varepsilon_b(\omega)]}{\lvert\varepsilon_b(\omega)+1\rvert^2}\frac{1}{\lvert\mathbf{r}-\mathsf{M}\mathbf{r}'\rvert}$
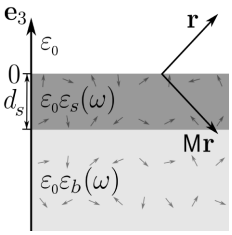	$\mathrm{Im}[g(\mathbf{r},\mathbf{r}',\omega)] = \frac{2d_s}{4\pi\varepsilon_0}\mathrm{Im}\left[\frac{\varepsilon_s^2(\omega)-\varepsilon_b^2(\omega)}{\varepsilon_s(\omega)[\varepsilon_b(\omega)+1]^2}\right]\mathbf{e}_3\cdot\frac{\partial}{\partial\mathbf{r}}\frac{1}{\lvert\mathbf{r}-\mathsf{M}\mathbf{r}'\rvert} - \frac{2}{4\pi\varepsilon_0}\frac{\mathrm{Im}[\varepsilon_b(\omega)]}{\lvert\varepsilon_b(\omega)+1\rvert^2}\frac{1}{\lvert\mathbf{r}-\mathsf{M}\mathbf{r}'\rvert}$

multipole dissipators. The Lindblad operator in Eq. (15) is given by the operator-valued charge distribution, implying that the master equation contains cross-terms involving different multipole moments.

B. Resonant motion

d. Oscillating monopole.—The quantum dynamics of an oscillating monopole at position $\mathbf{R} = \mathbf{R}_{\mathrm{eq}}$ can be decomposed into three bosonic modes with operators a_ℓ, frequencies ω_ℓ, and oscillation directions $\boldsymbol{\epsilon}_\ell$,

$$U_0^\dagger(t)\mathbf{R}U_0(t) = \mathbf{R}_{\mathrm{eq}} + \sum_{\ell=1}^{3}\sqrt{\frac{\hbar}{2m\omega_\ell}}(a_\ell e^{-i\omega_\ell t} + \mathrm{H.c.})\boldsymbol{\epsilon}_\ell. \tag{29}$$

If the frequencies are sufficiently well separated, so that the rotating-wave approximation applies, and for amplitudes sufficiently small, so that the field can be approximated locally, the Lindblad operators take on the form (Appendix B 3)

$$c_\ell(\mathbf{r}) = -q\sqrt{\frac{\hbar}{2m\omega_\ell}}\boldsymbol{\epsilon}_\ell\cdot\frac{\partial}{\partial\mathbf{r}}\delta(\mathbf{r}-\mathbf{R}_{\mathrm{eq}})a_\ell. \tag{30}$$

e. Oscillating dipole.—The corresponding calculation for an oriented dipole with time-independent dipole vector $\mathbf{p}$ whose center of mass is oscillating yields the Lindblad operators

$$c_\ell(\mathbf{r}) = \sqrt{\frac{\hbar}{2m\omega_\ell}}\left(\mathbf{p}\cdot\frac{\partial}{\partial\mathbf{r}}\right)\left(\boldsymbol{\epsilon}_\ell\cdot\frac{\partial}{\partial\mathbf{r}}\right)\delta(\mathbf{r}-\mathbf{R}_{\mathrm{eq}})a_\ell. \tag{31}$$

f. Oscillating quadrupole.—Likewise, for an oscillating oriented quadrupole with time-independent quadrupole tensor Q, one obtains

$$c_\ell(\mathbf{r}) = -\frac{1}{6}\sqrt{\frac{\hbar}{2m\omega_\ell}}\left(\frac{\partial}{\partial\mathbf{r}}\cdot\mathsf{Q}\frac{\partial}{\partial\mathbf{r}}\right)\left(\boldsymbol{\epsilon}_\ell\cdot\frac{\partial}{\partial\mathbf{r}}\right)\delta(\mathbf{r}-\mathbf{R}_{\mathrm{eq}})a_\ell. \tag{32}$$

g. Librating dipole.—A linear rotor with moment of inertia I and dipole operator $\mathbf{p}_\Omega = p\mathbf{n}_3$ parallel to the symmetry axis $\mathbf{n}_3$ is assumed to librate at $\mathbf{R}_{\mathrm{cm}}$ (cm stands for center of mass) in the two directions $\boldsymbol{\epsilon}_\alpha$, $\boldsymbol{\epsilon}_\beta$ perpendicular to its equilibrium orientation $\boldsymbol{\epsilon}_{\mathrm{eq}}$. Denoting the frequencies of the libration modes by ω_α, ω_β and the bosonic operators by a_α, a_β, the rotor symmetry axis evolves as

$$U_0^\dagger(t)\mathbf{n}_3U_0(t) = \boldsymbol{\epsilon}_{\mathrm{eq}} + \sum_{\ell=\alpha,\beta}\sqrt{\frac{\hbar}{2I\omega_\ell}}(a_\ell e^{-i\omega_\ell t} + \mathrm{H.c.})\boldsymbol{\epsilon}_\ell. \tag{33}$$

For sufficiently well-separated libration frequencies, the Lindblad operators take the form

$$c_\ell(\mathbf{r}) = -p\sqrt{\frac{\hbar}{2I\omega_\ell}}\boldsymbol{\epsilon}_\ell \cdot \frac{\partial}{\partial \mathbf{r}}\delta(\mathbf{r}-\mathbf{R}_{\rm cm})a_\ell. \tag{34}$$

h. Librating quadrupole.—Likewise, if the linear rotor is a quadrupole $\mathsf{Q}_\Omega = Q_{33}[3\mathbf{n}_3\otimes\mathbf{n}_3 - \mathbb{1}]/2$ with symmetry axis $\mathbf{n}_3$, librating as in Eq. (33), the Lindblad operators are given by

$$c_\ell(\mathbf{r}) = \frac{Q_{33}}{2}\sqrt{\frac{\hbar}{2I\omega_\ell}}\left(\boldsymbol{\epsilon}_{\rm eq}\cdot\frac{\partial}{\partial\mathbf{r}}\right)\left(\boldsymbol{\epsilon}_\ell\cdot\frac{\partial}{\partial\mathbf{r}}\right)\delta(\mathbf{r}-\mathbf{R}_{\rm cm})a_\ell. \tag{35}$$

i. Rotating dipole.—A linear rotor located at $\mathbf{R}_{\rm cm}$ is assumed to rotate in a plane spanned by $\boldsymbol{\epsilon}_1$ and $\boldsymbol{\epsilon}_2$. For sufficiently sharp angular momentum p_α, the symmetry axis $\mathbf{n}_3$ rotates approximately at a frequency $\omega_{\rm rot} = p_\alpha/I$ determined by the moment of inertia I,

$$U_0^\dagger(t)\mathbf{n}_3 U_0(t) \simeq \tfrac{1}{2}e^{-i\omega_{\rm rot}t}e^{-i\alpha}(\boldsymbol{\epsilon}_1 + i\boldsymbol{\epsilon}_2) + \text{H.c.} \tag{36}$$

with Euler-angle operator α. For a dipolar charge distribution $\mathbf{p}_\Omega = p\mathbf{n}_3$ with symmetry axis $\mathbf{n}_3$, the Lindblad operators read

$$c_{\rm rot}(\mathbf{r}) = -\frac{p}{2}(\boldsymbol{\epsilon}_1 + i\boldsymbol{\epsilon}_2)\cdot\frac{\partial}{\partial\mathbf{r}}\delta(\mathbf{r}-\mathbf{R}_{\rm cm})e^{-i\alpha}. \tag{37}$$

j. Rotating quadrupole.—Likewise, for a quadrupolar charge distribution with quadrupole tensor $\mathsf{Q}_\Omega = Q_{33}[3\mathbf{n}_3\otimes\mathbf{n}_3 - \mathbb{1}]/2$ rotating as in Eq. (36), one obtains the Lindblad operators

$$c_{\rm rot}(\mathbf{r}) = \frac{Q_{33}}{16}\left[(\boldsymbol{\epsilon}_1 + i\boldsymbol{\epsilon}_2)\cdot\frac{\partial}{\partial\mathbf{r}}\right]^2\delta(\mathbf{r}-\mathbf{R}_{\rm cm})e^{-2i\alpha}. \tag{38}$$

k. Freely rotating dipole.—Finally, we derive the Lindblad operators of a freely rotating linear rotor at a position $\mathbf{R}_{\rm cm}$ with the dipole operator specified by the Euler angle operators α and β,

$$p\mathbf{n}_3 = p(\sin\beta\cos\alpha\boldsymbol{\epsilon}_1 + \sin\beta\sin\alpha\boldsymbol{\epsilon}_2 + \cos\beta\boldsymbol{\epsilon}_3). \tag{39}$$

The energy eigenstates entering Eqs. (20) and (21) are given by the spherical harmonics $\langle\alpha,\beta|\ell,m\rangle = Y_{\ell m}(\beta,\alpha)$, with associated energies $E_\ell = \hbar^2\ell(\ell+1)/2I$. Expanding the dipole operator in the angular momentum basis

$$\langle\ell,m|\,p\mathbf{n}_3\,|\ell'm'\rangle = p\sum_{i=1}^{3} n^{(i)}_{\ell m\ell'm'}\boldsymbol{\epsilon}_i \tag{40}$$

yields

$$n^{(1)}_{\ell m\ell'm'} = (-1)^m\frac{1}{\sqrt{2}}\sqrt{(2\ell+1)(2\ell'+1)} \times\begin{pmatrix}\ell & \ell' & 1\\ 0 & 0 & 0\end{pmatrix}\left[\begin{pmatrix}\ell & \ell' & 1\\ -m & m' & -1\end{pmatrix} - \begin{pmatrix}\ell & \ell' & 1\\ -m & m' & 1\end{pmatrix}\right], \tag{41a}$$

$$n^{(2)}_{\ell m\ell'm'} = (-1)^m\frac{i}{\sqrt{2}}\sqrt{(2\ell+1)(2\ell'+1)} \times\begin{pmatrix}\ell & \ell' & 1\\ 0 & 0 & 0\end{pmatrix}\left[\begin{pmatrix}\ell & \ell' & 1\\ -m & m' & -1\end{pmatrix} + \begin{pmatrix}\ell & \ell' & 1\\ -m & m' & 1\end{pmatrix}\right], \tag{41b}$$

$$n^{(3)}_{\ell m\ell'm'} = (-1)^m\sqrt{(2\ell+1)(2\ell'+1)} \times\begin{pmatrix}\ell & \ell' & 1\\ 0 & 0 & 0\end{pmatrix}\begin{pmatrix}\ell & \ell' & 1\\ -m & m' & 0\end{pmatrix}. \tag{41c}$$

The expansion coefficients (21) thus depend on four quantum numbers,

$$c_{\ell m\ell'm'}(\mathbf{r}) = \langle\ell,m|\,\varrho_0[\mathsf{R}_\Omega^{\rm T}(\mathbf{r}-\mathbf{R}_{\rm cm})]\,|\ell'm'\rangle = -p\frac{\partial}{\partial\mathbf{r}}\delta(\mathbf{r}-\mathbf{R}_{\rm cm})\cdot\sum_{i=1}^{3} n^{(i)}_{\ell m\ell'm'}\boldsymbol{\epsilon}_i, \tag{42}$$

which are nonzero only for $|\ell'-\ell| = 1$ and $m - m' = \pm1, 0$ due to the Wigner 3-j symbols in Eq. (41). Since Eq. (20) is restricted to positive energy spacings, only the Lindblad operators

$$c_\ell(\mathbf{r}) = \sum_{m,m'} c_{\ell m\ell+1m'}\,|\ell,m\rangle\,\langle\ell+1,m'| \tag{43}$$

with frequencies $\omega_\ell := (E_{\ell'} - E_\ell)/\hbar = \hbar(\ell+1)/I$ contribute. We use the operators (43) in Sec. V D to simulate the rotational decoherence of a dipole above a superconducting surface covered with a dielectric layer.

General charge distribution.—The dissipator for a charge distribution characterized by several multipole moments does in general not decompose into a sum of pure multipole dissipators. However, this sum may be a

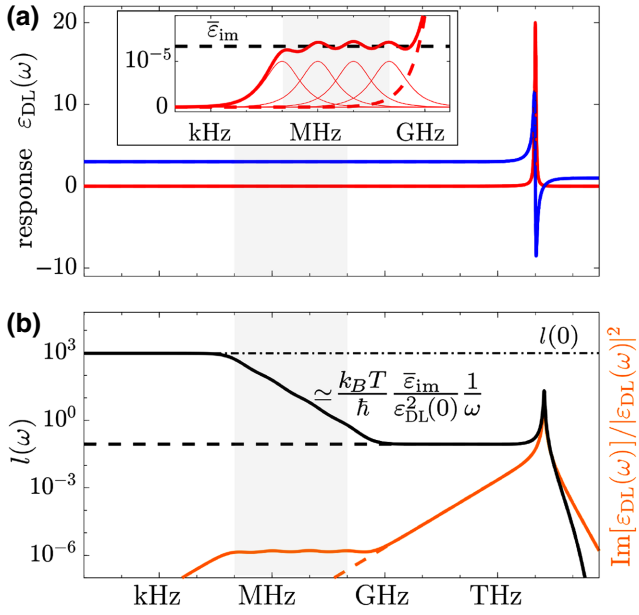

FIG. 2. Panel (a) shows the real (blue) and imaginary (red) parts of the dielectric permittivity (44), characterized by a single strong terahertz resonance ($\omega_5 = 10^{13}$ s^{-1}, $\gamma_5 = 10^{12}$ s^{-1}, $f_5 = 2$) and weak low-frequency resonances (thin red lines), as illustrated in the inset. The weak resonance forms a broad region (gray area) of approximately constant imaginary part. Panel (b) shows the energy loss function $\mathrm{Im}[\varepsilon_{\rm DL}(\omega)]/|\varepsilon_{\rm DL}(\omega)|^2$ (orange) and its thermal version $l(\omega)$ (black) in the presence (solid) and absence (dashed) of low-frequency resonances. For small frequencies, the low-frequency peaks determine $l(\omega)$ despite their small weights, and therefore dominate the surface-induced decoherence, while the energy loss is negligible. In the region of nearly flat imaginary part (gray area), $l(\omega)$ exhibits the characteristic $1/\omega$ scaling. We used $T = 300$ K, $f_n = 2\times10^{-5}$, $\omega_n = 10^{6+n}$ s^{-1}, and $\gamma_n = 10^{8+n}$ s^{-1} for $n = 1,\ldots,4$.

good approximation if the characteristic frequencies associated with the motion of the distinct multipole components are sufficiently well separated, so that all cross-terms effectively average to zero.

IV. SURFACE-FLUCTUATION KERNEL

Having specified the Lindblad operators, we now discuss the surface-fluctuation kernel, which depends on the geometry of the surface and its dielectric response, as characterized by the relative permittivity $\varepsilon_r(\mathbf{r},\omega)$. The latter is subject to the Kramers-Kronig relations, implying that high-frequency resonances described by peaks in the imaginary part of $\varepsilon_r(\mathbf{r},\omega)$ contribute to the low-frequency behavior of the real part (Fig. 2). As we will see below, even weak resonances due to surface-adsorbed molecules and imperfections can strongly affect the energy loss function at the typical trapping frequencies of ions and nanoparticles.

A simple model for the dielectric response is given by a sum of Drude-Lorentz oscillators [102]

$$\varepsilon_{\rm DL}(\omega) = 1 + \sum_{n\geq 0}\frac{f_n\omega_n^2}{\omega_n^2 - \omega^2 - i\gamma_n\omega}. \tag{44}$$

The imaginary part exhibits peaks at the resonance frequencies ω_n, whose relative weights are determined by the (real-valued) coefficients f_n, and whose widths are determined by the damping rates γ_n. The special case of a single resonance at $\omega_n = \omega_r$ with $f_n = \omega_p^2/\omega_r^2$ yields the Drude-Lorentz model for a single oscillator

$$\varepsilon_{\rm SDL}(\omega) = 1 + \frac{\omega_p^2}{\omega_r^2 - \omega^2 - i\gamma\omega}. \tag{45}$$

In the limit that the resonance frequency vanishes, this is referred to as the *Drude metal*,

$$\varepsilon_m(\omega) = 1 - \frac{\omega_{\rm pm}^2}{\omega^2 + i\gamma_m\omega}. \tag{46}$$

We also discuss decoherence close to a superconducting surface, with critical temperature T_c, at temperature $T < T_c$. Its permittivity can be written in the two-fluid model as [103,104]

$$\varepsilon_{\rm sc}(\omega) = 1 - \frac{\omega_{\rm pm}^2}{\omega^2 + i\gamma_m\omega}\left(\frac{T}{T_c}\right)^4 - \frac{1}{\omega^2\Lambda_0\varepsilon_0} \times\left[1 - \left(\frac{T}{T_c}\right)^4\right], \tag{47}$$

where pm stands for the plasma frequency of the metal, Λ_0 is a material-specific constant. For temperatures T approaching T_c from below, this superconductor turns into a normal metal. At much smaller temperatures it behaves like an ideal electron gas without damping.

A. Homogeneous half-space

We consider a particle levitated in vacuum at $\mathbf{r}\cdot\mathbf{e}_3 > 0$ above a semi-infinite dielectric half-space at $\mathbf{r}\cdot\mathbf{e}_3 < 0$ with homogeneous permittivity $\varepsilon_b(\omega)$. The Green function (5) for this configuration can be found in Appendix C 4. For the special case that $\mathbf{r}$ and $\mathbf{r}'$ are both in vacuum, as appearing in master equations (15) and (25), it is given in Table II. The imaginary part of the Green function decays with the inverse distance between location $\mathbf{r}$ and the mirror image of $\mathbf{r}'$ at location $\mathsf{M}\mathbf{r}'$, with the mirror tensor $\mathsf{M} = \mathbb{1} - 2\mathbf{e}_3\otimes\mathbf{e}_3$. In the special case of the

Drude-Lorentz model (44) one obtains

$$h(\mathbf{r},\mathbf{r}') = \frac{1}{4\pi\varepsilon_0}\frac{2k_BT}{\hbar}\frac{1}{|\mathbf{r}-\mathsf{M}\mathbf{r}'|}\frac{1}{[\varepsilon_{\rm DL}(0)+1]^2}\sum_{n\geq 0}\frac{f_n\gamma_n}{\omega_n^2}, \tag{48}$$

and for the Drude-metal half-space,

$$h(\mathbf{r},\mathbf{r}') = \frac{1}{4\pi\varepsilon_0}\frac{2k_BT}{\hbar}\frac{1}{|\mathbf{r}-\mathsf{M}\mathbf{r}'|}\frac{\gamma_m}{\omega_{\rm pm}^2}. \tag{49}$$

We use this surface-fluctuation kernel below to calculate the decoherence rate of electron beams near a metallic surface.

For a superconductor, the surface-fluctuation kernel follows from Eq. (47). In the static limit one obtains $h(\mathbf{r},\mathbf{r}') = 0$ since $n(\omega)\,\mathrm{Im}[2/[\varepsilon_{\rm sc}(\omega)+1]]$ vanishes. This means that there is no charge-induced decoherence of a slowly moving charge distribution in front of a pristine superconductor.

B. Half-space covered by a thin surface layer

In typical experimental situations, the surface may be covered by a thin dielectric surface layer. The presence of this layer can strongly affect the charge-induced decoherence and heating, even though its impact on the overall dielectric response of the surface is rather weak. Denoting the layer permittivity by $\varepsilon_s(\omega)$ and its thickness by d_s, one finds the imaginary part of the Green function for $\mathbf{r}$ and $\mathbf{r}'$ in vacuum,

$$\mathrm{Im}[g(\mathbf{r},\mathbf{r}',\omega)] = \frac{1}{4\pi\varepsilon_0}\int_0^\infty dk\,\mathrm{Im}\left(\frac{\xi_b(\omega)e^{-2kd_s}-\xi_v(\omega)}{1-\xi_v(\omega)\xi_b(\omega)e^{-2kd_s}}\right)e^{-k(\mathbf{r}+\mathbf{r}')\cdot\mathbf{e}_3}J_0\left(k\sqrt{[(\mathbf{r}-\mathbf{r}')\cdot\mathbf{e}_1]^2+[(\mathbf{r}-\mathbf{r}')\cdot\mathbf{e}_2]^2}\right), \tag{50}$$

where

$$\xi_b(\omega) = \frac{\varepsilon_s(\omega)-\varepsilon_b(\omega)}{\varepsilon_s(\omega)+\varepsilon_b(\omega)}, \tag{51}$$

$$\xi_v(\omega) = \frac{\varepsilon_s(\omega)-1}{\varepsilon_s(\omega)+1}. \tag{52}$$

Here, $J_0(\cdot)$ denotes the zeroth-order Bessel function. The full Green function is calculated in Appendix C 5.

For large distances, $\mathbf{r}\cdot\mathbf{e}_3 \gg d_s$ and $\mathbf{r}'\cdot\mathbf{e}_3 \gg d_s$, Eq. (50) can be expanded to first order in $kd_s \ll 1$, yielding the expression given in Table II. In the case of a low-permittivity dielectric layer on a metallic (or superconducting) bulk, $|\varepsilon_b(\omega)| \gg |\varepsilon_s(\omega)| \gtrsim 1$, the metal (or superconductor) effectively acts as a mirror. One then obtains

$$\mathrm{Im}[g(\mathbf{r},\mathbf{r}',\omega)] = -\frac{2}{4\pi\varepsilon_0}\frac{\mathrm{Im}[\varepsilon_b(\omega)]}{|\varepsilon_b(\omega)|^2}\frac{1}{|\mathbf{r}-\mathsf{M}\mathbf{r}'|} + \frac{2d_s}{4\pi\varepsilon_0}\frac{\mathrm{Im}[\varepsilon_s(\omega)]}{|\varepsilon_s(\omega)|^2}\mathbf{e}_3\cdot\frac{\partial}{\partial\mathbf{r}}\frac{1}{|\mathbf{r}-\mathsf{M}\mathbf{r}'|}. \tag{53}$$

For a dielectric layer characterized by the surface permittivity $\varepsilon_s(\omega) = \varepsilon_{\rm DL}(\omega)$ on top of a Drude metal, $\varepsilon_b(\omega) = \varepsilon_m(\omega)$, the general expression in Table II yields

$$h(\mathbf{r},\mathbf{r}') = \frac{1}{4\pi\varepsilon_0}\frac{2k_BT}{\hbar}\frac{\gamma_m}{\omega_{\rm pm}^2}\frac{1}{|\mathbf{r}-\mathsf{M}\mathbf{r}'|} - \frac{d_s}{4\pi\varepsilon_0}\frac{2k_BT}{\hbar} \times\left[\sum_{n\geq 0}\frac{f_n\gamma_n}{\omega_n^2} - \frac{2\gamma_m\varepsilon_{\rm DL}(0)}{\omega_{\rm pm}^2}\right] \times\frac{1}{\varepsilon_{\rm DL}^2(0)}\mathbf{e}_3\cdot\frac{\partial}{\partial\mathbf{r}}\frac{1}{|\mathbf{r}-\mathsf{M}\mathbf{r}'|}. \tag{54}$$

Here $\varepsilon_{\rm DL}(0) = 1+\sum_{n\geq 0}f_n$ is the static value of the surface response.

Replacing the metal by a superconductor, $\varepsilon_b(\omega) = \varepsilon_{\rm sc}(\omega)$, one obtains

$$h(\mathbf{r},\mathbf{r}') = -\frac{d_s}{4\pi\varepsilon_0}\frac{2k_BT}{\hbar}\frac{1}{\varepsilon_{\rm DL}^2(0)}\sum_{n\geq 0}\frac{f_n\gamma_n}{\omega_n^2}\mathbf{e}_3\cdot\frac{\partial}{\partial\mathbf{r}}\frac{1}{|\mathbf{r}-\mathsf{M}\mathbf{r}'|}, \tag{55}$$

which is equivalent to Eq. (54) for negligible damping $\gamma_m = 0$ in the bulk. Like in Eq. (53), the superconductor acts like a mirror for the fluctuations generated in the dielectric layer. This approximation is justified if the surface layer is thinner than the London penetration depth, which is the case for typical superconducting materials.

C. Electric field power spectral density

The surface noise kernel also characterizes the electric field fluctuations observed above thermal surfaces. As we

shall see below, the resulting electric field power spectral density (PSD) is closely related to the decoherence and heating rates of electric monopoles and dipoles.

The PSD at position $\mathbf{R}_0$ is defined as the Fourier transform of the autocorrelation function,

$$\mathsf{S}_{EE}(\mathbf{R}_0,\omega)=\frac{1}{2}\int_{-\infty}^{\infty}d\tau\,\langle\{\mathbf{E}(\mathbf{R}_0,t),\mathbf{E}(\mathbf{R}_0,t+\tau)\}\rangle\,e^{i\omega\tau}, \tag{56}$$

where $\mathbf{E}(\mathbf{r},t)$ denotes the electric field operator, described by the scalar potential (7), and $\{\cdot,\cdot\}$ is the dyadic anticommutator. For a thermal distribution, in the quasistatic limit one finds that

$$\mathsf{S}_{EE}(\mathbf{R}_0,\omega)=-2\hbar\left[n(\omega)+\frac{1}{2}\right]\frac{\partial}{\partial\mathbf{r}}\otimes\frac{\partial}{\partial\mathbf{r}'}\,\mathrm{Im}[g(\mathbf{r},\mathbf{r}',\omega)]\Big|_{\mathbf{r}=\mathbf{r}'=\mathbf{R}_0}, \tag{57}$$

which reduces for $\omega=0$ to

$$\mathsf{S}_{EE}(\mathbf{R}_0,\omega=0)=2\hbar\frac{\partial}{\partial\mathbf{r}}\otimes\frac{\partial}{\partial\mathbf{r}'}h(\mathbf{r},\mathbf{r}')\Big|_{\mathbf{r}=\mathbf{r}'=\mathbf{R}_0}. \tag{58}$$

For instance, a thin dielectric layer, as described by Eq. (53), gives rise to

$$\mathsf{S}_{EE}(\mathbf{R}_0,\omega)=\left[n(\omega)+\frac{1}{2}\right]\frac{\hbar}{4\pi\varepsilon_0}\left(\frac{\mathrm{Im}[\varepsilon_b(\omega)]}{|\varepsilon_b(\omega)|^2}\frac{1}{2|\mathbf{R}_0\cdot\mathbf{e}_3|^3}+\frac{\mathrm{Im}[\varepsilon_s(\omega)]}{|\varepsilon_s(\omega)|^2}\frac{3d_s}{4|\mathbf{R}_0\cdot\mathbf{e}_3|^4}\right)(\mathbb{1}+\mathbf{e}_3\otimes\mathbf{e}_3). \tag{59}$$

In the large temperature limit $k_BT/\hbar\omega\gg1$, this is equivalent to the expression given in Ref. [89]. On the other hand, the Drude-metal half-space with Eq. (46) yields, in the limit of small frequencies,

$$\mathsf{S}_{EE}(\mathbf{R}_0,0)=\frac{k_BT}{4\pi\varepsilon_0}\frac{\gamma_m}{2\omega_{\mathrm{pm}}^2}\frac{1}{|\mathbf{R}_0\cdot\mathbf{e}_3|^3}(\mathbb{1}+\mathbf{e}_3\otimes\mathbf{e}_3), \tag{60}$$

which is consistent with the calculations in Refs. [89,105,106]. As a final example, a Drude-Lorentz layer on a superconductor with Eq. (55) yields

$$\mathsf{S}_{EE}(\mathbf{R}_0,0)=\frac{k_BT}{4\pi\varepsilon_0}\frac{3d_s}{4|\mathbf{R}_0\cdot\mathbf{e}_3|^4}(\mathbb{1}+\mathbf{e}_3\otimes\mathbf{e}_3)\times\frac{1}{\varepsilon_{\mathrm{DL}}^2(0)}\sum_{n\geq0}\frac{f_n\gamma_n}{\omega_n^2}. \tag{61}$$

These examples illustrate that the presence of a thin dielectric layer induces the experimentally observed scaling

$$\mathsf{S}_{EE}(\mathbf{R}_0,\omega)\propto\frac{1}{d^4} \tag{62}$$

with $d=\mathbf{R}_0\cdot\mathbf{e}_3$ the distance to the surface. Importantly, this contribution from the layer dominates for typical electrode and surface layer materials [89]. We will see in the following section that this distance behavior translates to nanoparticle decoherence and heating rates.

D. Relevance of low-frequency surface excitations

Inserting the surface-fluctuation kernel into the master equation (25), for instance using Eq. (53), demonstrates that the magnitude of surface-induced decoherence is determined by the energy loss function $\mathrm{Im}[\varepsilon_r(\omega)]/|\varepsilon_r(\omega)|^2$ and by its thermal version

$$l(\omega)=n(\omega)\frac{\mathrm{Im}[\varepsilon_r(\omega)]}{|\varepsilon_r(\omega)|^2}. \tag{63}$$

The latter dominates the former for small frequencies [see Fig. 2(b)], and thus determines the high-temperature frequency behavior of the electric field PSD (59).

For instance, for a Drude-Lorentz dielectric (44) [Fig. 2(a)], the absolute value in the denominator of Eq. (63) can be approximated by its static value $\varepsilon_{\mathrm{DL}}(0)$, so that the function plateaus at

$$l(0)=\frac{k_BT}{\hbar\varepsilon_{\mathrm{DL}}^2(0)}\sum_{n\geq0}\frac{f_n\gamma_n}{\omega_n^2} \tag{64}$$

for frequencies much less than $\omega_n,\omega_n^2/\gamma_n$. Typically, high-frequency electronic transitions exhibit significantly larger weights f_n and thus dominate the static value of the dielectric permittivity. However, Eq. (63) can be enhanced by broad low-frequency contributions to the spectrum, each contributing with relative strength $f_n\gamma_n/\omega_n^2$. Such weak and broad absorption bands could, for instance, be due to weakly bound surface adsorbates [66,99].

Moreover, let us assume that these low-lying transitions give rise to a broad plateau in the absorption spectrum with mean imaginary dielectric response $\bar{\varepsilon}_{\mathrm{im}}$ [see Fig. 2(a)].

It then follows that the function $l(\omega)$ exhibits the experimentally observed $1/\omega$ frequency scaling [Fig. 2(b)]. Specifically, one obtains

$$l(\omega) \simeq \frac{k_B T}{\hbar} \frac{\bar{\varepsilon}_{\rm im}}{\varepsilon_{\rm DL}^2(0)} \frac{1}{\omega}. \tag{65}$$

This illustrates the decisive role played by the low-frequency dielectric response of the electrode surface in ion traps. As we shall see below, this frequency scaling carries over to the surface-induced decoherence and heating rates. We note that nonflat combinations of low-lying resonances can give rise to other power-law scalings [107].

V. HOW TO USE THE TOOLBOX

Having discussed how the particle charge distribution and the surface properties enter master equations (15) and (25), we now explain how one can identify the suitable master equation for a given experimental setting. This will be followed by two examples and a short discussion of relevant limiting cases, in which the master equations simplify to known results.

A. Finding the right master equation

To identify the appropriate master equation for a given physical situation requires comparing the involved timescales. These are determined by the setup, as described by the form and location of the particle charge distribution, its free dynamics, as well as the surface geometry, dielectric response, and temperature. Given this information, one proceeds as follows.

1. Specify the body-fixed charge distribution of the particle, e.g., in terms of its multipole moments, and estimate the characteristic timescales of the particle dynamics in absence of the surface.
2. Specify the surface response function, e.g., by experimental measurements or by a suitable model such as Eq. (44).
3. Check that electric field retardation is negligible and calculate the quasistatic Green function (5). If the surface is clean or covered by a thin dielectric layer, one can use the first or second row in Table II.
4. Estimate the resulting decay rate of surface-fluctuation correlations via Eqs. (8)–(10).

5.1. If the particle dynamics are much slower than the surface-fluctuation correlation time, use the slow-particle master equation (15).

   (a) If the particle charge distribution is characterized exclusively by its monopole, dipole, or quadrupole moment, one can use master equation *a*, *b*, or *c* in Table I.
   (b) Otherwise, insert the charge distribution into Eq. (15).

5.2. If both the free particle dynamics and the decay of surface-fluctuation correlations are much faster than the surface-induced particle dynamics, use the resonant master equation (25).

   (a) If the particle centre-of-mass is oscillating and its charge distribution is characterized solely by its monopole, dipole, or quadrupole moment, one can use master equation *d*, *e*, or *f* in Table I.
   (b) If the particle orientation is librating and its charge distribution is characterized solely by its dipole or quadrupole moment, one can use master equation *g* or *h* in Table I.
   (c) If the particle is rotating in a plane with approximately constant angular velocity and its charge distribution is characterized only by its dipole or quadrupole moment, one can use master equation *i* or *j* in Table I.
   (d) If the particle is simultaneously oscillating and librating or rotating, or for a general charge distribution, calculate the operators (20) and insert them into Eq. (25).

It is worth noting that, for a flat surface-fluctuation spectrum, $l(\omega_\ell) \simeq l(0)$, the resonant master equation (22) describes the same dynamics as the slow-particle master equation (12) if a rotating-wave approximation with respect to the surface-free particle dynamics is justified.

The next subsection shows that the Markov and quasistatic approximations are justified for typical state-of-the-art setups, ranging from trapped ions to molecules and nanoparticles. We then illustrate how to use the master equations in two examples, (i) a slowly rotating two-ion Coulomb crystal and (ii) a freely rotating polar molecule, both close to a surface covered by a thin dielectric layer. Finally, this section closes by discussing limiting situations in which the derived master equations reduce to known results.

B. Experimental adequacy of the description

Quasistatic approximation.—The quasistatic approximation applies if any retardation in the wave propagation from the source in the surface to the particle can be neglected. The experimentally observed distance scaling $\propto d^{-4}$ of the electric field noise [65,66,69–71] indicates that the predominant noise sources are longitudinal fields originating from a thin surface layer. Retardation effects can usually be neglected given that the time it takes a photon to travel through the surface layer of thickness d_s to the particle at distance d is much smaller than the characteristic timescale $1/\omega_0$ of the particle motion in the absence of the surface, $(\sqrt{|\varepsilon_s|}d_s + d)\omega_0/c \ll 1$. Since $|\varepsilon_s| \lesssim 40$ and $d_s \lesssim 5$ nm for typical surface contaminants [89], retardation is negligible for frequencies up to $\omega_0 = 30$ GHz

at $d = 1$ mm, as applies to typical setups with atoms [2,65,66], molecules [7–9], and nanoparticles [25,34,108–112]. In the absence of a thin surface layer, the quasistatic approximation is still justified as long as the skin depth δ is greater than the trapping height. For a Drude metal, one finds that $\delta^2 = \gamma_m c^2/\omega_0\omega_{\rm pm}^2$, yielding $\delta \approx 4.3$ mm for gold at kilohertz frequencies and $\delta \approx 140\ \mu$m at megahertz frequencies.

Born-Markov approximation.—The weak-coupling Born-Markov approximation is justified if the temporal correlations in the surface fluctuations are irrelevant for the particle dynamics. Rigorously, this requires the surface-induced particle relaxation to take place on a timescale much greater than that of temporal correlations. The surface-noise correlation timescale is dominated either by the thermal correlation time $\hbar/k_BT$ or by the width of the spectral density (8). For temperatures above 100 mK, the thermal correlation time falls below 100 ps, while the correlation timescale due to, e.g., the terahertz resonance in Fig. 2 reaches 1 ps at most. Similar timescales are obtained for typical metals, though low-lying overdamped surface resonances may dominate ($\gamma_n/\omega_n^2 \approx 10\ \mu$s for Fig. 2). These timescales can be compared to the particle-relaxation time, which lies in state-of-art setups in the range of up to milliseconds. In addition, the rigorous Born-Markov approximation requires the surface-free particle dynamics to be either much slower than the decay of surface correlations (slow-particle limit) or much faster than the particle-relaxation timescale (resonant limit). For instance, a rotating nanoparticle at 100 kHz is described by the slow-particle limit given the above surface properties, while the resonant limit applies for an oscillating ion at megahertz frequencies. We emphasize that even if the Born-Markov approximation is not justified formally, it often yields an adequate description given that non-Markovian modifications of the dynamics are often marginal [113].

C. Example 1: two-ion Coulomb crystal

We consider two equally charged ions with $q = e$, rotating with constant angular velocity $\omega_{\rm rot}$ at a constant interparticle distance $d = 5\ \mu$m around their center of mass $\mathbf{R}\cdot\mathbf{e}_3 = 100\ \mu$m above a flat surface with surface normal $\mathbf{e}_3$, motivated by the experiment of Ref. [25]. Choosing the reference charge distribution such that the interparticle axis is aligned with the surface normal, one has

$$\varrho_0(\mathbf{r}) = q\delta\left(\mathbf{r} - \frac{d}{2}\mathbf{e}_3\right) + q\delta\left(\mathbf{r} + \frac{d}{2}\mathbf{e}_3\right). \tag{66}$$

It is characterized not only by the monopole and quadrupole moments, but also exhibits higher charge moments. The direction of the interparticle charge axis at a given crystal orientation Ω is given by $\mathbf{n}_3 = \cos\alpha\sin\beta\mathbf{e}_1 + \sin\alpha\sin\beta\mathbf{e}_2 + \cos\beta\mathbf{e}_3$.

For a flat surface layer of thickness $d_s = 5$ nm at $T = 300$ K with the exemplary response of Fig. 2, exhibiting spectrally flat and weak features in the kilohertz to gigahertz range on a bulk metal, the quasistatic approximation is justified. This is because (i) retardation between the surface and the particle is negligible on the timescale of the particle motion and (ii) even the weak features with $\bar{\varepsilon}_{\rm im} \approx 1 \times 10^{-5}$ dominate the total noise, i.e., noise from the gold bulk as well as blackbody radiation from infinitely distant surfaces, at the particle frequencies and its small distance above the surface. In addition, the surface-fluctuation correlations (9) and (10) decay on a timescale that is determined by the spectral widths of $l(\omega)$ and $\mathrm{Im}[\varepsilon_r(\omega)]/|\varepsilon_r(\omega)|^2$. In Fig. 2 the width of $l(\omega)$ is approximately given by $\omega_2^2/\gamma_2 = 10^5\ \mathrm{s}^{-1}$. The width of the energy loss function is approximately given by the width of the underdamped high-frequency peak of $\gamma_5 = 10^{12}\ \mathrm{s}^{-1}$. The Markov approximation and Eq. (15) are justified since, for rotation frequencies $\omega_{\rm rot} \lesssim 100$ kHz, the crystal moves (and relaxes) much slower than those surface correlation timescales.

The resulting orientational decoherence rate (18) of the crystal with the surface-fluctuation kernel (55) is depicted in Fig. 3. We display the decoherence of a superposition between a fixed orientation (black dumbbell and dots) and all other possible orientations. The rate as a function of the

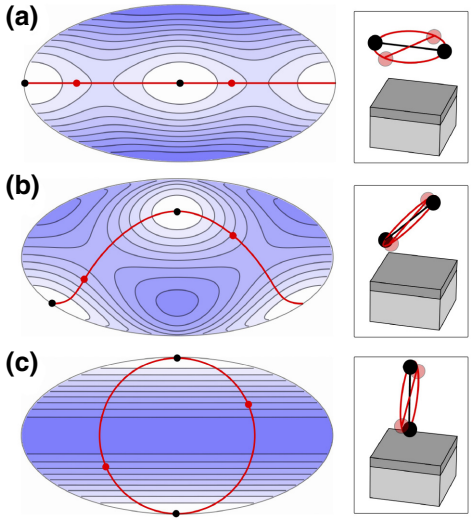

FIG. 3. Rotational decoherence rate of a two-ion Coulomb crystal [25] rotating around a fixed center-of-mass position near a dielectric layer deposited on bulk gold. (a) The contour plot in Mollweide projection displays the rate (18) for a superposition between two orientations with one parallel to the surface (black dumbbell and dots). The plot is normalized to the maximum decoherence rate of $\Gamma_{\rm max} = 3.7$ kHz (blue). Great-circle trajectories of the second branch are shown in red. In panels (b) and (c) the fixed orientation (black dumbbell) is set to 45° and 90° to the surface plane, respectively.

varying orientation is depicted in a contour plot in Mollweide projection. In superposition experiments, such as in Ref. [25], the varying orientation typically rotates on great circles (red).

D. Example 2: rotating polar molecule

Next, we consider a point dipole in a superposition of angular momentum states $|\ell, m\rangle$ (quantization axis $\boldsymbol{\epsilon}_3$) of the form $|\Psi\rangle = (|2,0\rangle + |1,0\rangle)/\sqrt{2}$ above a superconducting surface at the temperature $T = 100$ mK [7,10]. Following Ref. [7], we assume a dipole moment of $p = 4.36$ D, while all other charge moments vanish, and $\omega_0 = \hbar/I = 2\pi \times 5.5$ GHz, implying that $n(\omega_0) \approx 0.07 \ll 1$. At such low temperatures no energy states outside $\ell \in \{0,1,2\}$ get populated since $n(\omega_\ell) \simeq 0$ for all ℓ with $\omega_\ell = (\ell+1)\hbar/I$. Thus, the only operators needed to specify dissipator (25) are

$$c_\ell(\mathbf{r}) = -p \sum_{i=1}^{3} n_{\ell,i} \boldsymbol{\epsilon}_i \cdot \frac{\partial}{\partial \mathbf{r}} \delta(\mathbf{r} - \mathbf{R}_{\rm cm}). \tag{67}$$

Here we defined the operators

$$n_{0,i} = \left(n^{(i)}_{0011} |0,0\rangle\langle 1,1| + n^{(i)}_{0010} |0,0\rangle\langle 1,0| + n^{(i)}_{001-1} |0,0\rangle\langle 1,-1| \right), \tag{68a}$$

$$n_{1,i} = \left(n^{(i)}_{1120} |1,1\rangle\langle 2,0| + n^{(i)}_{1020} |1,0\rangle\langle 2,0| + n^{(i)}_{1-120} |1,-1\rangle\langle 2,0| \right). \tag{68b}$$

The coefficients $n^{(i)}_{\ell m \ell' m'}$ are given in Eq. (41).

Inserting Eq. (67) into Eq. (25) yields the dissipator

$$\mathcal{L}\rho = \frac{2p^2}{\hbar} \sum_{\ell=0}^{1} \sum_{i,j=1}^{3} h_{ij}(\mathbf{R}_{\rm cm}, \omega_\ell) \times \left(n_{\ell,i} \rho n^\dagger_{\ell,j} - \frac{1}{2} n^\dagger_{\ell,j} n_{\ell,i} \rho - \frac{1}{2} \rho n^\dagger_{\ell,j} n_{\ell,i} \right) \tag{69}$$

with the surface-fluctuation kernel

$$h_{ij}(\mathbf{R}_{\rm cm}, \omega_\ell) = -\left(\boldsymbol{\epsilon}_j \cdot \frac{\partial}{\partial \mathbf{r}} \right) \times \left(\boldsymbol{\epsilon}_i \cdot \frac{\partial}{\partial \mathbf{r}'} \right) \mathrm{Im}[g(\mathbf{r}, \mathbf{r}', \omega_\ell)] \Big|_{\mathbf{r}=\mathbf{r}'=\mathbf{R}_{\rm cm}}. \tag{70}$$

The particle is located at a distance of $\mathbf{R}_{\rm cm} \cdot \mathbf{e}_3 = 100$ nm [7] from the superconducting surface, with normal vector $\mathbf{e}_3$, which is covered by a thin dielectric layer. We assume a layer thickness of $d_s = 4$ nm and $\varepsilon_s(\omega_\ell) = 3 \times (1 + 0.001i)$, as is realistic for, e.g., an oxide layer [89,114]. This permittivity is of the same order of magnitude as the response shown in Fig. 2. At these frequencies, its value is dominated by the high-frequency peak rather than the low-frequency features. The quasistatic approximation of the electric fields is justified since (i) retardation between the surface and the particle is negligible and (ii) the noise

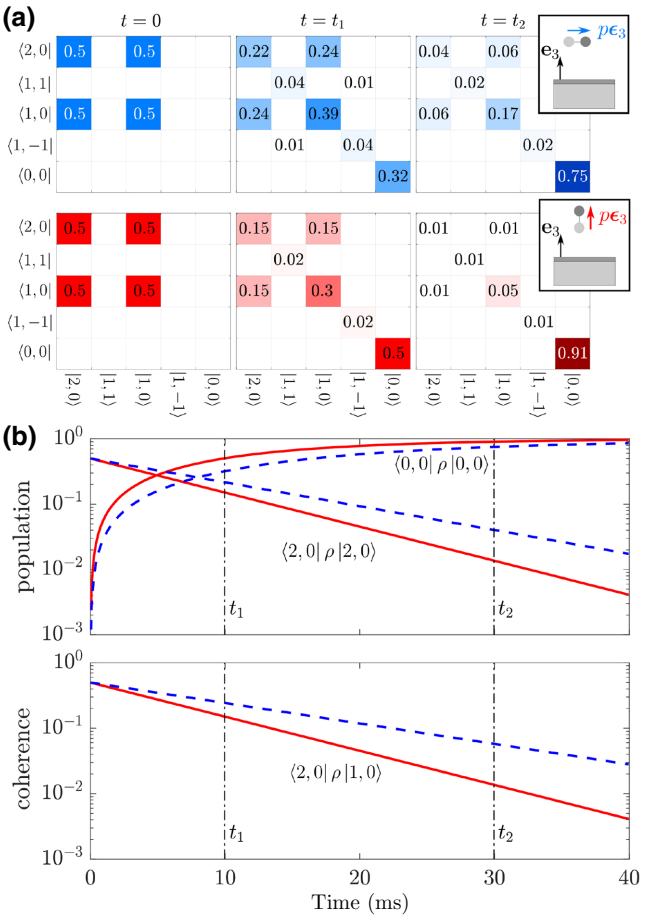

FIG. 4. Rotational decoherence of a point dipole near a superconducting surface. (a) The particle is initially prepared in an angular momentum superposition state with initial dipole $p\boldsymbol{\epsilon}_3$ pointing perpendicular (blue) or parallel (red) to the surface normal vector $\mathbf{e}_3$. The noise originating from the surface is dominated by a thin layer covering the superconducting device (see Sec. V). The dynamics governed by Eq. (69) are displayed via the density operator in the basis of the lowest angular momentum states $|\ell m\rangle$ (quantization axis $\boldsymbol{\epsilon}_3$) for the times $t = 0$, $t_1 = 10$ ms, and $t_2 = 30$ ms. Surface-induced dissipation relaxes the particle to its rotational ground state. (b) (top) While the ground-state population approaches unity for large times, the excited state population decreases at a constant rate. The latter differs in the two scenarios, marked in dashed blue and solid red, respectively. (b) (bottom) The coherence decay in (a) also occurs at a constant rate. Decoherence in the red case is stronger, since the field fluctuations are stronger in the direction of the surface normal.

from the layer dominates over blackbody radiation and noise from a realistic metal or superconductor bulk. As discussed in the previous example, the surface-fluctuation correlations of the spectrum shown in Fig. 2 decay at a rate of 10^5 s^{-1}. Consequently, the Markov approximation is justified because the particle decoheres much slower than surface correlations decay and than the particle rotates, as we show next.

In Fig. 4, we solve the master equation (11) with the dissipator (69), neglecting the coherent surface interaction. Using Eq. (53), we can approximate

$$h_{ij}(\mathbf{R}_{\rm cm},\omega_\ell) \simeq \frac{1}{4\pi\varepsilon_0}\frac{\mathrm{Im}[\varepsilon_s(\omega_\ell)]}{|\varepsilon_s(\omega_\ell)|^2}\frac{3d_s}{8|\mathbf{R}_{\rm cm}\cdot\mathbf{e}_3|^4} \times[\delta_{ij}+(\boldsymbol{\epsilon}_j\cdot\mathbf{e}_3)(\boldsymbol{\epsilon}_i\cdot\mathbf{e}_3)], \tag{71}$$

expressing that the noise is predominantly due to the surface layer. The initial state $\rho(0)=|\Psi\rangle\langle\Psi|$ generates a mean dipole moment that points along the $\boldsymbol{\epsilon}_3$ axis. In contrast, pure angular momentum states, or an incoherent mixture thereof, lead to a vanishing mean dipole. As displayed in Fig. 4, the decoherence rate crucially depends on the alignment between the dipole and the surface normal. The order of magnitude of the decoherence rate can be roughly estimated as $p^2\sum_i h_{ii}(\mathbf{R}_{\rm cm},\omega_\ell)/\hbar \approx 4\times10^2/\mathrm{s}$. This rate will increase for higher temperatures and a dielectric with a larger loss tangent, becoming relevant for hybrid quantum systems with polar molecules and superconducting devices [7,10]. Note that some of the coherences in Fig. 4 exhibit a nonmonotonic time dependence due to the Lindblad operators (68) not being diagonal in the angular momentum basis.

E. Relation to previous results

Electron beams near a metal surface.—In the slow-particle limit the decoherence rate of a monopole reduces to that calculated in Ref. [88]. Specifically, the decoherence rate follows from Table Ia and Eq. (17) together with the surface-fluctuation kernel of a Drude metal (49) as

$$\Gamma(\mathbf{R},\mathbf{R}') = \frac{1}{4\pi\varepsilon_0}\frac{q^2k_BT}{\hbar^2}\frac{2\gamma_m}{\omega_{\rm pm}^2}\left[\frac{1}{|\mathbf{R}-\mathsf{M}\mathbf{R}|}+\frac{1}{|\mathbf{R}'-\mathsf{M}\mathbf{R}'|} -2\frac{1}{|\mathbf{R}-\mathsf{M}\mathbf{R}'|}\right]. \tag{72}$$

For superposed electron beams traveling parallel to a metal surface with a fixed distance between the superposition branches, this is identical to the path decoherence predicted in Ref. [88] and measured in Ref. [74].

Motional decoherence of ions in quadrupole traps.—For a point monopole, the resonant master equation (25) reduces to that used for describing heating of ions levitated in quadrupole traps. Specifically, using row d in Table I at a trapping frequency $\omega_k=\omega_0$ and oscillation direction $\boldsymbol{\epsilon}_k=\boldsymbol{\epsilon}_0$, yields the ground-state heating rate $\Gamma_h(\omega_0)=q^2n(\omega_0)h_0(\mathbf{R}_{\rm eq})/m\omega_0$ [71,105]. For $k_BT/\hbar\omega_0 \gg 1$, as is the case for typical trapping conditions [71], the heating rate can be approximated by means of the electric field PSD (57),

$$\Gamma_h(\omega_0) \simeq \frac{q^2}{2m\hbar\omega_0}\boldsymbol{\epsilon}_0\cdot\mathsf{S}_{EE}(\mathbf{R}_{\rm eq},\omega_0)\boldsymbol{\epsilon}_0, \tag{73}$$

which exhibits the characteristic distance and frequency scalings discussed in Sec. IV.

Rotational heating of polar molecules.—Ground-state heating of dipolar rotors near surfaces has been studied in Ref. [87]. In order to verify that the two results agree, we evaluate the master equation (25) for a point dipole, neglecting all other multipole moments, at a fixed center-of-mass position with nondegenerate rotational states. Considering the quasistatic approximation (C5) in Ref. [87] shows that both theories coincide.

VI. DISCUSSION

Given the dielectric properties and geometry of the surface, the presented toolbox serves to predict quantitatively the induced heating and decoherence for a multitude of particle shapes and charge distributions. By disentangling the role of the particle from that of the surface, it provides novel tools for systematically studying the problem of surface-induced noise and decoherence in electric traps. In the following, we discuss a possible roadmap for future investigations, then comment on potential future extensions of the framework, and finally provide our conclusions.

A. Taming the surface noise

Characterizing the surface.—As a main feature of the presented toolbox, the material properties of the surface enter only via the dielectric response functions of the bulk and surface layer. *Ex situ* measurements of the low-frequency behavior of the dielectric material can therefore be used to predict its impact on the particle dynamics. Performing such measurements for different materials and surface contaminants will serve to identify the origin and strength of broad, low-frequency features in the dielectric permittivity.

Sensing field fluctuations.—The levitated particle acts as a highly sensitive probe of electric surface noise since the heating force felt by a monopole and the torque experienced by a dipole are fully characterized by the electric field PSD (57). Specifically, the decoherence rate of a slow monopole at position $\mathbf{R}_0$ in a superposition of size $\Delta\mathbf{R}=\mathbf{R}-\mathbf{R}'$ (with $|\mathbf{R}_0|\gg|\Delta\mathbf{R}|$) reads

$$\Gamma(\mathbf{R},\mathbf{R}') \simeq \frac{q^2}{2\hbar^2}\Delta\mathbf{R}\cdot\mathsf{S}_{EE}(\mathbf{R}_0,0)\Delta\mathbf{R}. \tag{74}$$

Such a quadratic dependence on $\Delta\mathbf{R}$ is accompanied by momentum diffusion, and thus heating, with diffusion tensor $q^2\mathsf{S}_{EE}(\mathbf{R}_0,0)/2$. Likewise, for orientational superpositions of a slow point dipole in a superposition of orientations Ω and Ω', the decoherence rate reads

$$\Gamma_{\Omega\Omega'}(\mathbf{R}_{\rm cm},\mathbf{R}_{\rm cm}) = \frac{1}{2\hbar^2}\Delta\mathbf{p}\cdot\mathsf{S}_{EE}(\mathbf{R}_{\rm cm},0)\Delta\mathbf{p} \tag{75}$$

with $\Delta\mathbf{p} = \mathbf{p}_\Omega - \mathbf{p}_{\Omega'}$. Again, this decoherence is associated with angular momentum diffusion and thus heating [115].

Sensing gradient fluctuations.—In more general situations, the electric field PSD does not suffice to describe the induced heating. For instance, the orientational decoherence and heating of a point quadrupole probes the PSD of the field gradient, a fourth-rank tensor, at its center-of-mass position. Likewise, the center-of-mass decoherence of a point dipole is determined by field gradient fluctuations characterized by the same tensor. For instance, the orientational decoherence of a point quadrupole at position $\mathbf{R}_{\rm cm}$ reads

$$\begin{aligned}\Gamma_{\Omega\Omega'}(\mathbf{R}_{\rm cm},\mathbf{R}_{\rm cm}) &= \frac{1}{36\hbar}\left[\frac{\partial}{\partial\mathbf{R}}\cdot(\mathsf{Q}_\Omega-\mathsf{Q}_{\Omega'})\frac{\partial}{\partial\mathbf{R}}\right]\\ &\times\left[\frac{\partial}{\partial\mathbf{R}'}\cdot(\mathsf{Q}_\Omega-\mathsf{Q}_{\Omega'})\frac{\partial}{\partial\mathbf{R}'}\right]h(\mathbf{R},\mathbf{R}')\Big|_{\mathbf{R}=\mathbf{R}'=\mathbf{R}_{\rm cm}}.\end{aligned} \tag{76}$$

Note that this equation exhibits a surface distance dependence distinct from the scaling in Eq. (59), showing that large-quadrupole particles might yield further insight into the origins of anomalous heating [66].

Probing nonlocal field correlations.—It follows from Eq. (18) that the center-of-mass decoherence rate of a spatially delocalized wavepacket depends on nonlocal noise correlations, rather than on the local electric field PSD. In particular, the decoherence rate remains bounded for large distances in the superposition, as observed in experiments with electron beams [74]. Creating and monitoring spatially extended superposition states thus enables deducing information on the surface noise that is not encoded in the heating rates, e.g., by utilizing modern parameter estimation techniques [116].

Modeling the dielectric response.—Identifying the microscopic origins of surface noise will require input from atomistic theoretical models. This encompasses accounting for the role of microscopic processes as sources and as mediators of electromagnetic noise. *Ab initio* calculations [97,98] and molecular-dynamics simulations [99] link microscopic models to the macroscopic dielectric response, which in turn serves as one input for the presented toolbox and can thus be tested experimentally.

Tailoring the surface response.—Once the mechanism of surface noise is understood, surface-induced decoherence may be suppressed by choosing materials with beneficial dielectric properties. Specific surface coatings may help suppress such noise at the relevant particle frequencies or prevent adsorption of surface contaminants. Plasma cleaning [117] and ion milling [118] of electrode surfaces in ion traps have shown that even slight surface modifications can have great impact on the noise level.

Geometry design.—As a further handle to reduce the impact of unavoidable surface fluctuations, one may adjust the surface geometry to modify the electric fields at the particle position. For instance, when working with dipolar particles, one can minimize field noise, as compared to field gradient noise, by a mirror-symmetric arrangement of short-circuited electrodes.

B. Extending the toolbox

The presented toolbox is based on a number of assumptions, namely the quasistatic approximation of the surface-induced field, the Born-Markov approximation for the particle dynamics, the rigid description of the particle charge distribution, and the neglect of magnetic surface effects, all of which is justified for typical ion and nanoparticle trapping experiments. That said, the toolbox could be extended in following ways.

Transverse electric field.—Taking the transverse field into account requires two steps. First, the Green tensor, which describes both the longitudinal and the transverse field propagation, must be calculated instead of the scalar Green function. Second, the coupling between the particle velocity and the transverse fields must be accounted for. Note that the impact of Thomson scattering, which describes scattering from the purely transverse field at vanishing particle velocity, is discussed in Appendix D, where it is shown that its impact is negligibly small compared to decoherence due to the longitudinal field and other experimentally relevant decoherence processes.

Anisotropic and nonlocal dielectrics.—To incorporate the possible anisotropy and nonlocality of surface materials requires using the tensorial and nonlocal dielectric response in the definition of the surface polarization operators [100] and the scalar Green function. While the subsequent calculation is presumably tedious, we expect the derivation presented in this paper to carry over to the generalized case.

Nonrigid charge distributions.—The fact that the bound charges inside the particle can fluctuate and react to fields emanating from the surface can be included in terms of the particle polarization. This adds to the dynamics (i) the Casimir-Polder interaction between the particle and the surface [91] as well as (ii) the associated decoherence channel [96]. This effect is expected to become relevant for weakly charged micron-sized dielectrics.

Magnetic effects.—Magnetic contributions to the particle-surface interaction can be taken into account by adding to the Hamiltonian the coupling of fluctuating surface magnetization currents to the charge distribution (see Appendix A 2). Likewise, if the particle exhibits permanent or fluctuating magnetic moments, their coupling to the surface polarization and magnetization fields can be included [91,95]. These extensions may serve to model the rotranslational heating of levitated magnets or superconductors close to surfaces [119–122], which are an alternative to electrically levitated particles [27,38]. Incorporating magnetic effects may also allow studying the impact of exotic surface responses, such as bianisotropic materials [123,124].

Rotranslational thermalization.—The dynamics of rotranslational damping are fully accounted for in the resonant limit. In the slow-particle limit, they can be described by including to first order the particle motion during the decay of surface-fluctuation correlations [101]. This adds to the master equation terms that are linear in the center-of-mass momentum and angular momentum operators. The resulting master equation describes rotranslational thermalization if it is of a specific form [125].

Non-Markovian effects.—If the surface-fluctuation correlations decay on a timescale comparable to that of the particle motion, the weak-coupling Born-Markov approximation loses justification, even though it may still provide a good description for most situations. The impact of colored noise and related non-Markovian effects can be taken into account via the method of influence functionals [101] or by using quantum Langevin equations [126]. The latter feature an operator-valued noise to describe the dynamics of selected observables. If necessitated by empirical evidence, such a treatment is possible in principle, though significantly more involved and less versatile.

C. Conclusions

The framework described in this article quantitatively predicts surface-induced rotational and translational decoherence and heating of extended objects with arbitrary shape and charge distribution. The quantum master equations (15) and (25) incorporate the surface properties in terms of (i) the dielectric permittivity, which is empirically accessible and microscopically computable, and (ii) the scalar Green function, which describes the field propagation in arbitrary geometries. Our work applies to a variety of state-of-the-art experimental setups, ranging from trapped ion setups [66] to hybrid quantum devices with charged atoms and molecules [10] to nanoparticles in electric and optical traps [38]. We expect the presented framework and the worked-out toolbox Table I to be instrumental for a wide class of future quantum experiments with charged objects of finite extension. We hope that this sets the stage for a concerted effort involving quantum physics, materials design, and device fabrication to tame the surface noise.

ACKNOWLEDGMENTS

This research is funded by the Deutsche Forschungsgemeinschaft (DFG, German Research Foundation)—411042854.

APPENDIX A: DERIVATION OF THE COUPLING HAMILTONIAN

This appendix derives the coupling Hamiltonian between the charged particle and the surface. We first derive the minimal coupling Hamiltonian (1) from the Lorentz force and torque laws for a moving and revolving rigid charge distribution. Inserting into this Hamiltonian the electromagnetic fields in terms of surface excitations then yields the surface-particle interaction Hamiltonian, which serves as a starting point for the derivation of the master equations.

1. Rotor-field coupling

To describe the classical dynamics of a particle in the electromagnetic field, we introduce the position $\mathbf{R}$ and the orientation via Euler angles $\Omega = \{\alpha, \beta, \gamma\}$ in the z-y'-z'' convention. The particle charge distribution at a given point $\mathbf{r}$ reads $\varrho(\mathbf{r}) = \varrho_0[\mathsf{R}_\Omega^{\mathrm{T}}(\mathbf{r} - \mathbf{R})]$. Here, ϱ_0 describes the charge distribution in the reference position and the rotation tensor R_Ω relates the space-fixed axes $\mathbf{e}_i$ to the principal axes $\mathbf{n}_i = \mathsf{R}_\Omega \mathbf{e}_i$. The angular velocity is defined via the kinematic relation $\dot{\mathsf{R}}_\Omega = \omega \times \mathsf{R}_\Omega$. The coupling Lagrangian,

$$L = E_{\mathrm{kin}} - \int d^3r \varrho(\mathbf{r})\phi(\mathbf{r},t) + \int d^3r \mathbf{j}(\mathbf{r}) \cdot \mathbf{A}(\mathbf{r},t), \quad \text{(A1)}$$

involves the charge distribution and the current density,

$$\mathbf{j}(\mathbf{r}) = \varrho_0[\mathsf{R}_\Omega^{\mathrm{T}}(\mathbf{r} - \mathbf{R})][\dot{\mathbf{R}} + \boldsymbol{\omega} \times (\mathbf{r} - \mathbf{R})], \quad \text{(A2)}$$

due to the rigid motion of the body.

We first show that this Lagrangian is consistent with the Lorentz force and torque laws. To demonstrate this equivalence, we use the fact that

$$\boldsymbol{\omega} = \dot{\alpha}\mathbf{e}_3 + \dot{\beta}\mathbf{e}_\xi + \dot{\gamma}\mathbf{n}_3 \quad \text{(A3)}$$

with $\mathbf{e}_\xi = -\sin\alpha\,\mathbf{e}_1 + \cos\alpha\,\mathbf{e}_2$. We employ Eq. (A3) to express the kinetic energy E_{kin} and the current density in terms of the Euler angles. We then transform the integrals

in Eq. (A1) to the body-fixed frame, yielding

$$L = \frac{1}{2}\boldsymbol{\omega}\cdot \mathrm{I}_\Omega \boldsymbol{\omega} + \frac{1}{2}m\dot{\mathbf{R}}^2 - \int d^3r \varrho_0(\mathbf{r})\phi(\mathbf{R}+\mathsf{R}_\Omega\mathbf{r},t) + \int d^3r \varrho_0(\mathbf{r})(\dot{\mathbf{R}}+\boldsymbol{\omega}\times\mathsf{R}_\Omega\mathbf{r})\cdot\mathbf{A}(\mathbf{R}+\mathsf{R}_\Omega\mathbf{r},t). \tag{A4}$$

The Lagrange equation for the center of mass

$$\frac{d}{dt}\frac{\partial L}{\partial \dot{\mathbf{R}}} - \frac{\partial L}{\partial \mathbf{R}} = 0 \tag{A5}$$

involves the total time derivative of the vector potential

$$\frac{d}{dt}\mathbf{A}(\mathbf{R}+\mathsf{R}_\Omega\mathbf{r},t) = (\dot{\mathbf{R}}+\boldsymbol{\omega}\times\mathsf{R}_\Omega\mathbf{r})\cdot\frac{\partial}{\partial\mathbf{R}_0}\mathbf{A}(\mathbf{R}_0,t) + \frac{\partial}{\partial t}\mathbf{A}(\mathbf{R}+\mathsf{R}_\Omega\mathbf{r},t) \tag{A6}$$

with $\mathbf{R}_0 = \mathbf{R}+\mathsf{R}_\Omega\mathbf{r}$. Using Eq. (A6), the Lagrange equation yields

$$m\ddot{\mathbf{R}} = \int d^3r \varrho_0(\mathbf{r})(\dot{\mathbf{R}}+\boldsymbol{\omega}\times\mathsf{R}_\Omega\mathbf{r})\times\mathbf{B}(\mathbf{R}+\mathsf{R}_\Omega\mathbf{r},t) + \int d^3r \varrho_0(\mathbf{r})\mathbf{E}(\mathbf{R}+\mathsf{R}_\Omega\mathbf{r},t), \tag{A7}$$

which describes the center-of-mass dynamics of an extended charge distribution in the presence of the electric and magnetic fields

$$\mathbf{E}(\mathbf{r},t) = -\frac{\partial}{\partial\mathbf{r}}\phi(\mathbf{r},t) - \frac{\partial}{\partial t}\mathbf{A}(\mathbf{r},t), \tag{A8}$$

$$\mathbf{B}(\mathbf{r},t) = \frac{\partial}{\partial\mathbf{r}}\times\mathbf{A}(\mathbf{r},t). \tag{A9}$$

The Lagrange equations for the Euler angles are more involved. First, we deduce some useful relations from the definition of the rotation matrix and Eq. (A3),

$$\frac{\partial}{\partial\dot{\mu}} = \mathbf{e}_\mu\cdot\frac{\partial}{\partial\boldsymbol{\omega}}, \tag{A10a}$$

$$\frac{\partial\mathsf{R}_\Omega}{\partial\mu} = \mathbf{e}_\mu\times\mathsf{R}_\Omega, \tag{A10b}$$

$$\frac{d\mathbf{e}_\mu}{dt} = \mathsf{R}_\Omega\frac{\partial}{\partial\mu}\mathsf{R}_\Omega^{\mathrm{T}}\boldsymbol{\omega}, \tag{A10c}$$

with $\mu\in\{\alpha,\beta,\gamma\}$ and $\mathbf{e}_\mu\in\{\mathbf{e}_3,\mathbf{e}_\xi,\mathbf{n}_3\}$. Note that $d\mathbf{e}_3/dt = 0$ since the space-fixed axis does not move. Let us start with the angle α,

$$\frac{d}{dt}\frac{\partial L}{\partial\dot{\alpha}} - \frac{\partial L}{\partial\alpha} = 0, \tag{A11}$$

and use Eq. (A10a) to write

$$\frac{d}{dt}\frac{\partial}{\partial\dot{\alpha}}\frac{1}{2}\boldsymbol{\omega}\cdot\mathrm{I}_\Omega\boldsymbol{\omega} = \frac{d}{dt}\mathbf{e}_3\cdot\mathrm{I}_\Omega\boldsymbol{\omega} = \mathbf{e}_3\cdot\frac{d}{dt}\mathrm{I}_\Omega\boldsymbol{\omega} + \frac{d\mathbf{e}_3}{dt}\cdot\mathrm{I}_\Omega\boldsymbol{\omega}. \tag{A12}$$

Since $\mathrm{I}_0 = \mathsf{R}_\Omega^{\mathrm{T}}\mathrm{I}_\Omega\mathsf{R}_\Omega$ is independent of the Euler angles, we find that

$$\frac{\partial}{\partial\alpha}\frac{1}{2}\boldsymbol{\omega}\cdot\mathrm{I}_\Omega\boldsymbol{\omega} = \frac{\partial}{\partial\alpha}\frac{1}{2}(\mathsf{R}_\Omega^{\mathrm{T}}\boldsymbol{\omega})\cdot\mathrm{I}_0(\mathsf{R}_\Omega^{\mathrm{T}}\boldsymbol{\omega}) = \frac{d\mathbf{e}_3}{dt}\cdot\mathrm{I}_\Omega\boldsymbol{\omega}, \tag{A13}$$

where we used Eq. (A10c). Combining Eqs. (A12) and (A13), one thus obtains the $\mathbf{e}_3$ component of the angular-momentum time derivative

$$\left(\frac{d}{dt}\frac{\partial}{\partial\dot{\alpha}} - \frac{\partial}{\partial\alpha}\right)\frac{1}{2}\boldsymbol{\omega}\cdot\mathrm{I}_\Omega\boldsymbol{\omega} = \mathbf{e}_3\cdot\frac{d}{dt}\mathrm{I}_\Omega\boldsymbol{\omega}. \tag{A14}$$

The term involving the scalar potential can be rewritten using Eq. (A10b),

$$\left(\frac{d}{dt}\frac{\partial}{\partial\dot{\alpha}} - \frac{\partial}{\partial\alpha}\right)\phi(\mathbf{R}+\mathsf{R}_\Omega\mathbf{r},t) = -\mathbf{e}_3\cdot(\mathsf{R}_\Omega\mathbf{r})\times\frac{\partial}{\partial\mathbf{R}_0}\phi(\mathbf{R}_0,t), \tag{A15}$$

again with $\mathbf{R}_0 = \mathbf{R}+\mathsf{R}_\Omega\mathbf{r}$. Likewise, we evaluate the term involving the vector potential. In a first step, we compute

$$\begin{aligned}\frac{d}{dt}\frac{\partial}{\partial\dot{\alpha}}[(\dot{\mathbf{R}}+\boldsymbol{\omega}\times\mathsf{R}_\Omega\mathbf{r})\cdot\mathbf{A}(\mathbf{R}+\mathsf{R}_\Omega\mathbf{r},t)] &= \frac{d}{dt}[\mathbf{e}_3\cdot(\mathsf{R}_\Omega\mathbf{r})\times\mathbf{A}(\mathbf{R}+\mathsf{R}_\Omega\mathbf{r},t)] \\ &= \mathbf{e}_3\cdot(\mathsf{R}_\Omega\mathbf{r})\times\frac{d}{dt}\mathbf{A}(\mathbf{R}+\mathsf{R}_\Omega\mathbf{r},t) + \mathbf{A}(\mathbf{R}+\mathsf{R}_\Omega\mathbf{r},t) \\ &\cdot\frac{d}{dt}\mathbf{e}_3\times(\mathsf{R}_\Omega\mathbf{r}),\end{aligned} \tag{A16}$$

where we used Eq. (A10a). Noting that

$$\frac{d}{dt}\mathbf{e}_3\times(\mathsf{R}_\Omega\mathbf{r}) = \frac{d}{dt}\frac{\partial}{\partial\alpha}\mathsf{R}_\Omega\mathbf{r} = \frac{\partial}{\partial\alpha}\boldsymbol{\omega}\times\mathsf{R}_\Omega\mathbf{r}, \tag{A17}$$

Eq. (A16) yields

$$\frac{d}{dt}\frac{\partial}{\partial\dot{\alpha}}[(\dot{\mathbf{R}}+\boldsymbol{\omega}\times\mathsf{R}_\Omega\mathbf{r})\cdot\mathbf{A}(\mathbf{R}+\mathsf{R}_\Omega\mathbf{r},t)] = \mathbf{e}_3\cdot(\mathsf{R}_\Omega\mathbf{r})\times\frac{d}{dt}\mathbf{A}(\mathbf{R}+\mathsf{R}_\Omega\mathbf{r},t)+\mathbf{A}(\mathbf{R}+\mathsf{R}_\Omega\mathbf{r},t)\cdot\frac{\partial}{\partial\alpha}\boldsymbol{\omega}\times(\mathsf{R}_\Omega\mathbf{r}). \tag{A18}$$

Subtracting the α derivative gives

$$\left(\frac{d}{dt}\frac{\partial}{\partial\dot{\alpha}}-\frac{\partial}{\partial\alpha}\right)[(\dot{\mathbf{R}}+\boldsymbol{\omega}\times\mathsf{R}_\Omega\mathbf{r})\cdot\mathbf{A}(\mathbf{R}+\mathsf{R}_\Omega\mathbf{r},t)] = \mathbf{e}_3\cdot(\mathsf{R}_\Omega\mathbf{r})\times\frac{d}{dt}\mathbf{A}(\mathbf{R}+\mathsf{R}_\Omega\mathbf{r},t)-(\dot{\mathbf{R}}+\boldsymbol{\omega}\times\mathsf{R}_\Omega\mathbf{r})\cdot\frac{\partial}{\partial\alpha}\mathbf{A}(\mathbf{R}+\mathsf{R}_\Omega\mathbf{r},t). \tag{A19}$$

With the help of Eq. (A10b) one finds that

$$\begin{aligned}\left(\frac{d}{dt}\frac{\partial}{\partial\dot{\alpha}}-\frac{\partial}{\partial\alpha}\right)&[(\dot{\mathbf{R}}+\boldsymbol{\omega}\times\mathsf{R}_\Omega\mathbf{r})\cdot\mathbf{A}(\mathbf{R}+\mathsf{R}_\Omega\mathbf{r},t)]\\ &=\mathbf{e}_3\cdot(\mathsf{R}_\Omega\mathbf{r})\times\frac{d}{dt}\mathbf{A}(\mathbf{R}+\mathsf{R}_\Omega\mathbf{r},t)\\ &\quad-\left(\mathbf{e}_3\cdot(\mathsf{R}_\Omega\mathbf{r})\times\frac{\partial}{\partial\mathbf{R}_0}\right)(\dot{\mathbf{R}}+\boldsymbol{\omega}\times\mathsf{R}_\Omega\mathbf{r})\cdot\mathbf{A}(\mathbf{R}_0,t)\\ &=\mathbf{e}_3\cdot(\mathsf{R}_\Omega\mathbf{r})\times\frac{\partial}{\partial t}\mathbf{A}(\mathbf{R}+\mathsf{R}_\Omega\mathbf{r},t)\\ &\quad-\mathbf{e}_3\cdot(\mathsf{R}_\Omega\mathbf{r})\times\left\{(\dot{\mathbf{R}}+\boldsymbol{\omega}\times\mathsf{R}_\Omega\mathbf{r})\right.\\ &\quad\left.\times\left[\frac{\partial}{\partial\mathbf{R}_0}\times\mathbf{A}(\mathbf{R}_0,t)\right]\right\},\end{aligned} \tag{A20}$$

where Eq. (A6) and the Graßmann identity have been used. We combine Eqs. (A14), (A15), and (A20) with the Lagrange equation for α to finally obtain

$$\mathbf{e}_3\cdot\frac{d}{dt}\mathsf{I}_\Omega\boldsymbol{\omega}=\mathbf{e}_3\cdot\int d^3r\varrho_0(\mathbf{r})(\mathsf{R}_\Omega\mathbf{r})\times[\mathbf{E}(\mathbf{R}+\mathsf{R}_\Omega\mathbf{r},t)+(\dot{\mathbf{R}}+\boldsymbol{\omega}\times\mathsf{R}_\Omega\mathbf{r})\times\mathbf{B}(\mathbf{R}+\mathsf{R}_\Omega\mathbf{r},t)]. \tag{A21}$$

This is the $\mathbf{e}_3$ component of the Lorentz torque acting on an extended charge distribution.

Since Eqs. (A10a)–(A10c) equally hold for β and γ, the corresponding Lagrange equations yield the analogue of Eq. (A21), but with $\mathbf{e}_3$ replaced by $\mathbf{e}_\xi$ and $\mathbf{n}_3$, respectively. Thus, we have demonstrated that the Lagrangian (A1) is indeed consistent with the Lorentz torque acting on an extended charge distribution,

$$\frac{d}{dt}\mathsf{I}_\Omega\boldsymbol{\omega}=\int d^3r\varrho_0(\mathbf{r})(\mathsf{R}_\Omega\mathbf{r})[\mathbf{E}(\mathbf{R}+\mathsf{R}_\Omega\mathbf{r},t)+(\dot{\mathbf{R}}+\boldsymbol{\omega}\times\mathsf{R}_\Omega\mathbf{r})\times\mathbf{B}(\mathbf{R}+\mathsf{R}_\Omega\mathbf{r},t)]. \tag{A22}$$

In order to obtain the Hamiltonian, we first define the canonical linear and angular momenta

$$\mathbf{P}=\frac{\partial L}{\partial\dot{\mathbf{R}}}=m\dot{\mathbf{R}}+\int d^3r\varrho_0(\mathbf{r})\mathbf{A}(\mathbf{R}+\mathsf{R}_\Omega\mathbf{r},t), \tag{A23}$$

$$\mathbf{J}=\frac{\partial L}{\partial\boldsymbol{\omega}}=\mathsf{I}_\Omega\boldsymbol{\omega}+\int d^3r\varrho_0(\mathbf{r})(\mathsf{R}_\Omega\mathbf{r})\times\mathbf{A}(\mathbf{R}+\mathsf{R}_\Omega\mathbf{r},t), \tag{A24}$$

and then perform a Legendre transformation. Here we used Eq. (A10a) and related the angular momentum vector to the canonical Euler momenta via $p_\alpha=\mathbf{e}_3\cdot\mathbf{J}$, $p_\beta=\mathbf{e}_\xi\cdot\mathbf{J}$, and $p_\gamma=\mathbf{n}_3\cdot\mathbf{J}$. The Legendre transformation

$$\begin{aligned}H&=\dot{\mathbf{R}}\cdot\mathbf{P}+\dot{\alpha}p_\alpha+\dot{\beta}p_\beta+\dot{\gamma}p_\gamma-L\\&=\dot{\mathbf{R}}\cdot\mathbf{P}+\boldsymbol{\omega}\cdot\mathbf{J}-L\end{aligned} \tag{A25}$$

yields Hamiltonian (1).

2. Macroscopic quantum electrodynamics

One central ingredient of macroscopic quantum electrodynamics is the Green tensor $\mathsf{G}(\mathbf{r},\mathbf{r}',\omega)$, giving the electromagnetic field at position $\mathbf{r}$ due to a source current located at $\mathbf{r}'$. In the presence of dispersive media with permittivity $\varepsilon_r(\mathbf{r},\omega)$ and permeability $\mu_r(\mathbf{r},\omega)$, it fulfills the defining equation

$$\frac{\partial}{\partial\mathbf{r}}\times\frac{1}{\mu_r(\mathbf{r},\omega)}\left[\frac{\partial}{\partial\mathbf{r}}\times\mathsf{G}(\mathbf{r},\mathbf{r}',\omega)\right]-\frac{\omega^2}{c^2}\varepsilon_r(\mathbf{r},\omega)\mathsf{G}(\mathbf{r},\mathbf{r}',\omega)=\mathbb{1}\delta(\mathbf{r}-\mathbf{r}'), \tag{A26}$$

along with the boundary condition $\mathsf{G}(\mathbf{r},\mathbf{r}',\omega)=\mathbb{0}$ for $|\mathbf{r}-\mathbf{r}'|\to\infty$. The electric field

$$\mathbf{E}(\mathbf{r},t)=\frac{1}{2\pi}\int_0^\infty d\omega\,\mathbf{E}(\mathbf{r},\omega)e^{-i\omega t}+\text{c.c.} \tag{A27}$$

due to the current density $\mathbf{j}(\mathbf{r},\omega)$ is then given by

$$\mathbf{E}(\mathbf{r},\omega)=i\mu_0\omega\int d^3r'\mathsf{G}(\mathbf{r},\mathbf{r}',\omega)\mathbf{j}(\mathbf{r}',\omega). \tag{A28}$$

If the current density obeys the fluctuation-dissipation theorem, one obtains [91]

$$\langle\mathbf{E}^*(\mathbf{r},\omega)\otimes\mathbf{E}(\mathbf{r},\omega')\rangle=4\pi k_BT\mu_0\omega\delta(\omega-\omega')\times\text{Im}[\mathsf{G}(\mathbf{r},\mathbf{r},\omega)]. \tag{A29}$$

The theory is quantized by expressing the current density in terms of quantum harmonic oscillators [91,100], the so-called polarization and magnetization oscillators $\mathbf{f}_\lambda(\mathbf{r},\omega)$, $\lambda \in \{e,m\}$. They obey the canonical commutation relations $[\mathbf{f}_\lambda(\mathbf{r},\omega),\mathbf{f}_{\lambda'}(\mathbf{r}',\omega')] = \mathbb{0}$ and $[\mathbf{f}_\lambda(\mathbf{r},\omega),\mathbf{f}^\dagger_{\lambda'}(\mathbf{r}',\omega')] = \mathbb{1}\delta_{\lambda,\lambda'}\delta(\mathbf{r}-\mathbf{r}')\delta(\omega-\omega')$. These oscillators are related to the (noise) polarization and magnetization of the medium through

$$\mathbf{P}_N(\mathbf{r},\omega) = i\sqrt{4\pi\hbar\varepsilon_0\,\mathrm{Im}[\varepsilon_r(\mathbf{r},\omega)]}\mathbf{f}_e(\mathbf{r},\omega), \tag{A30}$$

$$\mathbf{M}_N(\mathbf{r},\omega) = \sqrt{\frac{4\pi\hbar}{\mu_0}\frac{\mathrm{Im}[\mu_r(\mathbf{r},\omega)]}{|\mu_r(\mathbf{r},\omega)|^2}}\mathbf{f}_m(\mathbf{r},\omega), \tag{A31}$$

so that the associated noise current density

$$\mathbf{j}_N(\mathbf{r},\omega) = -i\omega\mathbf{P}_N(\mathbf{r},\omega) + \frac{\partial}{\partial\mathbf{r}}\times\mathbf{M}_N(\mathbf{r},\omega) \tag{A32}$$

acts as a source for the electromagnetic field. The free-field dynamics are governed by the Hamiltonian

$$H_f = \sum_{\lambda=e,m}\int d^3r\int_0^\infty d\omega\hbar\omega\mathbf{f}^\dagger_\lambda(\mathbf{r},\omega)\cdot\mathbf{f}_\lambda(\mathbf{r},\omega). \tag{A33}$$

In Coulomb gauge the electromagnetic potentials originating from the dielectric can be expressed through the (Schrödinger-picture) polarization and magnetization oscillators as [91,100]

$$\mathbf{A}(\mathbf{r}) = \sum_{\lambda=e,m}\int d^3r'\int_0^\infty d\omega\frac{1}{i\omega}{}^{\perp}\mathsf{G}_\lambda(\mathbf{r},\mathbf{r}',\omega)\mathbf{f}_\lambda(\mathbf{r}',\omega) + \mathrm{H.c.}, \tag{A34}$$

$$\phi(\mathbf{r}) = -\frac{1}{4\pi}\sum_{\lambda=e,m}\int d^3r'\int_0^\infty d\omega\int d^3s \times\frac{\mathbf{r}-\mathbf{s}}{|\mathbf{r}-\mathbf{s}|^3}\cdot\mathsf{G}_\lambda(\mathbf{s},\mathbf{r}',\omega)\mathbf{f}_\lambda(\mathbf{r}',\omega) + \mathrm{H.c.} \tag{A35}$$

Here

$${}^{\perp}\mathsf{G}_\lambda(\mathbf{r},\mathbf{r}',\omega) = \int d^3s\,\delta^\perp(\mathbf{r}-\mathbf{s})\mathsf{G}_\lambda(\mathbf{s},\mathbf{r}',\omega) \tag{A36}$$

is the left-transverse part of the tensors G_λ, which are related to the Green tensor,

$$\mathsf{G}_e(\mathbf{r},\mathbf{r}',\omega) = i\frac{\omega^2}{c^2}\sqrt{\frac{\hbar}{\pi\varepsilon_0}\mathrm{Im}[\varepsilon_r(\mathbf{r}',\omega)]}\mathsf{G}(\mathbf{r},\mathbf{r}',\omega), \tag{A37}$$

$$\mathsf{G}_m(\mathbf{r},\mathbf{r}',\omega) = i\frac{\omega}{c}\sqrt{\frac{\hbar}{\pi\varepsilon_0}\frac{\mathrm{Im}[\mu_r(\mathbf{r}',\omega)]}{|\mu_r(\mathbf{r}',\omega)|^2}}\left[\frac{\partial}{\partial\mathbf{r}'}\times\mathsf{G}(\mathbf{r}',\mathbf{r},\omega)\right]^{\mathrm{T}}. \tag{A38}$$

The transverse delta function is defined as

$$\delta^\perp(\mathbf{r}) = \frac{\partial}{\partial\mathbf{r}}\times\left(\frac{\partial}{\partial\mathbf{r}}\times\mathbb{1}\right)\frac{1}{4\pi r}. \tag{A39}$$

Expressing the Green tensor in terms of the scalar Green function $g(\mathbf{r},\mathbf{r}',\omega)$ (see Appendix C) shows that the vector potential vanishes, while the scalar potential is of the form (7). In the following, we formulate the theory in terms of the Green tensor to keep the discussion general. Simplifications associated with using the scalar Green function g are discussed along the way.

The quantized electric field (A28) thus reads

$$\mathbf{E}(\mathbf{r}) = \sum_{\lambda=e,m}\int d^3r'\int_0^\infty d\omega\mathsf{G}_\lambda(\mathbf{r},\mathbf{r}',\omega)\mathbf{f}_\lambda(\mathbf{r}',\omega) + \mathrm{H.c.} \tag{A40}$$

We note that in the presence of a particle, the field (A40) is not yet the physical electric field, since the Coulomb field of the particle charge in the absence of the dielectric medium has still to be added [91]. The dynamics generated by the minimal coupling Hamiltonian (1) and the free-field dynamics (A33) are consistent with the Maxwell equations, the Lorentz force and torque, and thermal field fluctuations in absorbing media.

In the following, we neglect the vector potential to get the total Hamiltonian

$$H = H_0 + H_f + H_{\mathrm{int}}, \tag{A41}$$

where the free Hamiltonian

$$H_0 = \frac{1}{2m}\mathbf{P}^2 + \frac{1}{2}\mathbf{J}\cdot\mathrm{I}_\Omega^{-1}\mathbf{J} + V_{\mathrm{ext}}(\mathbf{R},\Omega) \tag{A42}$$

involves the external potential $V_{\mathrm{ext}}(\mathbf{R},\Omega)$ and the particle-field interaction reads

$$H_{\mathrm{int}} = -\frac{1}{4\pi}\int d^3r\varrho_0(\mathbf{r})\sum_{\lambda=e,m}\int d^3r'\int_0^\infty d\omega\int d^3s \times\frac{\mathbf{R}+\mathsf{R}_\Omega\mathbf{r}-\mathbf{s}}{|\mathbf{R}+\mathsf{R}_\Omega\mathbf{r}-\mathbf{s}|^3}\cdot\mathsf{G}_\lambda(\mathbf{s},\mathbf{r}',\omega)\mathbf{f}_\lambda(\mathbf{r}',\omega) + \mathrm{H.c.} \tag{A43}$$

Here $\mathbf{R}$, $\mathbf{P}$, $\Omega = \{\alpha,\beta,\gamma\}$, $p_\alpha = \mathbf{e}_3\cdot\mathbf{J}$, $p_\beta = \mathbf{e}_\xi\cdot\mathbf{J}$, and $p_\gamma = \mathbf{n}_3\cdot\mathbf{J}$ are operators satisfying the canonical commutation relations of translation and rotation.

APPENDIX B: BORN-MARKOV APPROXIMATION

This section derives the two main master equations from the above-discussed interaction Hamiltonian. In a first step, we perform the weak-coupling approximation, and then evaluate the resulting Markovian master equation in the slow-particle limit and in the resonant limit.

1. Weak-coupling approximation

In the weak-coupling approximation, the time evolution of the interaction-picture density operator $\tilde{\rho}(t) = U_0^\dagger(t)\rho(t)U_0(t)$ with $U_0(t) = \exp\left[-it(H_0 + H_f)/\hbar\right]$ can be written as [101]

$$\frac{\partial\tilde{\rho}}{\partial t} \simeq \frac{1}{\hbar^2}\int_0^\infty d\tau\, \mathrm{tr}_B\{[\tilde{H}_{\mathrm{int}}(t), [\tilde{\rho}(t)\otimes\rho_B, \tilde{H}_{\mathrm{int}}(t-\tau)]]\}, \tag{B1}$$

where the bath density operator ρ_B determines the state of the field degrees of freedom, which are assumed to be uncorrelated with the particle state, while the bath correlation (surface-fluctuation correlation) is assumed to decay much faster than the particle-relaxation time. The interaction Hamiltonian (A43) in the interaction picture decomposes as

$$\tilde{H}_{\mathrm{int}}(t) = U_0^\dagger(t)H_{\mathrm{int}}U_0(t) = \int d^3s\mathbf{C}(\mathbf{s},t)\cdot\mathbf{b}(\mathbf{s},t), \tag{B2}$$

where we have defined the Coulomb field operator

$$\mathbf{C}(\mathbf{s},t) = U_0^\dagger(t)\int d^3r\varrho_0(\mathbf{r})\frac{\mathbf{s}-\mathbf{R}-\mathsf{R}_\Omega\mathbf{r}}{|\mathbf{s}-\mathbf{R}-\mathsf{R}_\Omega\mathbf{r}|^3}U_0(t) \tag{B3}$$

and the bath operator

$$\mathbf{b}(\mathbf{s},t) = \sum_{\lambda=e,m}\int d^3r'\int_0^\infty d\omega\mathsf{G}_\lambda(\mathbf{s},\mathbf{r}',\omega)\mathbf{f}_\lambda(\mathbf{r}',\omega)\frac{e^{-i\omega t}}{4\pi} + \mathrm{H.c.} \tag{B4}$$

We assume the bath state ρ_B to be thermal with respect to the free-field Hamiltonian, implying that $\langle\mathbf{f}_\lambda(\mathbf{r}',\omega)\rangle_B = 0$, where $\langle\cdot\rangle_B = \mathrm{tr}_B\{\cdot\rho_B\}$. The second moments of the bath oscillators are finite,

$$\langle\mathbf{f}_\lambda^\dagger(\mathbf{r},\omega)\otimes\mathbf{f}_{\lambda'}(\mathbf{r}',\omega')\rangle_B = n(\omega)\delta(\mathbf{r}-\mathbf{r}')\delta(\omega-\omega')\delta_{\lambda,\lambda'}\mathbb{1}, \tag{B5}$$

where we have introduced the Bose-Einstein distribution $n(\omega) = 1/[\exp(\hbar\omega/k_BT) - 1]$. The second moments determine the bath-operator autocorrelations,

$$\langle\mathbf{b}(\mathbf{s},t)\otimes\mathbf{b}(\mathbf{s}',t-\tau)\rangle_B = \frac{\mathsf{N}(\mathbf{s},\mathbf{s}',\tau) - i\mathsf{D}(\mathbf{s},\mathbf{s}',\tau)}{2}, \tag{B6}$$

$$\langle\mathbf{b}(\mathbf{s}',t-\tau)\otimes\mathbf{b}(\mathbf{s},t)\rangle_B = \frac{\mathsf{N}(\mathbf{s}',\mathbf{s},\tau) + i\mathsf{D}(\mathbf{s}',\mathbf{s},\tau)}{2}. \tag{B7}$$

These autocorrelations contain the tensorial dissipation kernel (9) and the tensorial noise kernel (10). Both are determined by the spectral density

$$\mathsf{J}(\mathbf{s},\mathbf{s}',\omega) = \frac{\mu_0}{\pi}\omega^2\,\mathrm{Im}[\mathsf{G}(\mathbf{s},\mathbf{s}',\omega)], \tag{B8}$$

as follows by using the relation [91]

$$\sum_{\lambda=e,m}\int d^3r'\,\mathsf{G}_\lambda(\mathbf{s},\mathbf{r}',\omega)\mathsf{G}_\lambda^{*\mathrm{T}}(\mathbf{s}',\mathbf{r}',\omega) = \frac{\hbar\mu_0}{\pi}\omega^2\,\mathrm{Im}[\mathsf{G}(\mathbf{s},\mathbf{s}',\omega)]. \tag{B9}$$

In addition, the Onsager reciprocity [91] of the Green tensor,

$$\mathsf{G}^{\mathrm{T}}(\mathbf{s},\mathbf{s}',\omega) = \mathsf{G}(\mathbf{s}',\mathbf{s},\omega), \tag{B10}$$

also applies to D, N, and J, while the Schwarz reflection principle of G leads to

$$\mathsf{J}(\mathbf{s},\mathbf{s}',-\omega) = -\mathsf{J}(\mathbf{s},\mathbf{s}',\omega). \tag{B11}$$

In summary, Eq. (B1) can be rewritten as

$$\frac{\partial\tilde{\rho}}{\partial t} = \frac{1}{\hbar^2}\int_0^\infty d\tau\int d^3sd^3s' \times\left(\frac{i}{2}\left[\mathbf{C}(\mathbf{s},t),\left\{\mathsf{D}(\mathbf{s},\mathbf{s}',\tau)\mathbf{C}(\mathbf{s}',t-\tau),\tilde{\rho}(t)\right\}\right] - \frac{1}{2}\left[\mathbf{C}(\mathbf{s},t),\left[\mathsf{N}(\mathbf{s},\mathbf{s}',\tau)\mathbf{C}(\mathbf{s}',t-\tau),\tilde{\rho}(t)\right]\right]\right). \tag{B12}$$

This non-Markovian evolution equation serves as a starting point to derive the Markovian master equations in two different limiting cases: the slow-particle limit and the resonant limit.

2. Slow-particle limit

If the free particle motion is slow, so that the autocorrelations D and N drop on a much shorter timescale than the

timescale over which the Coulomb field operator $\mathbf{C}(\mathbf{s}',t)$ changes, one can approximate

$$\mathbf{C}(\mathbf{s}',t-\tau)\simeq\mathbf{C}(\mathbf{s}',t). \tag{B13}$$

In this case, the time-integration in Eq. (B12) can be carried out, yielding

$$\int_0^\infty d\tau\,\mathsf{D}(\mathbf{s},\mathbf{s}',\tau)=\frac{2\hbar}{(4\pi)^2}\frac{\mu_0}{\pi}\int_0^\infty d\omega\,\omega\,\mathrm{Im}[\mathsf{G}(\mathbf{s},\mathbf{s}',\omega)], \tag{B14}$$

$$\int_0^\infty d\tau\,\mathsf{N}(\mathbf{s},\mathbf{s}',\tau)=\frac{2k_BT\mu_0}{(4\pi)^2}\lim_{\omega\downarrow0}\omega\,\mathrm{Im}[\mathsf{G}(\mathbf{s},\mathbf{s}',\omega)]. \tag{B15}$$

Transforming Eq. (B12) back to the Schrödinger picture one obtains

$$\begin{aligned}\frac{\partial\rho}{\partial t}=&-\frac{i}{\hbar}[H_0+H_{\mathrm{SI}},\rho]+\frac{2k_BT\mu_0}{(4\pi)^2\hbar^2}\int d^3sd^3s'\\&\times\left(\mathbf{C}(\mathbf{s},0)\cdot\rho\lim_{\omega\downarrow0}\omega\,\mathrm{Im}\left[\mathsf{G}(\mathbf{s},\mathbf{s}',\omega)\right]\mathbf{C}(\mathbf{s}',0)\right.\\&\left.-\frac{1}{2}\left\{\mathbf{C}(\mathbf{s},0)\cdot\lim_{\omega\downarrow0}\omega\,\mathrm{Im}\left[\mathsf{G}(\mathbf{s},\mathbf{s}',\omega)\right]\mathbf{C}(\mathbf{s}',0),\rho\right\}\right),\end{aligned} \tag{B16}$$

where we have introduced the coherent surface interaction (Lamb shift)

$$\begin{aligned}H_{\mathrm{SI}}=&-\frac{1}{(4\pi)^2}\frac{\mu_0}{\pi}\int d^3sd^3s'\mathbf{C}(\mathbf{s},0)\\&\cdot\int_0^\infty d\omega\omega\,\mathrm{Im}[\mathsf{G}(\mathbf{s},\mathbf{s}',\omega)]\mathbf{C}(\mathbf{s}',0).\end{aligned} \tag{B17}$$

The frequency integral included in Eq. (B17) can be rewritten as an integral over the whole frequency axis,

$$\int_0^\infty d\omega\omega\,\mathrm{Im}[\mathsf{G}(\mathbf{s},\mathbf{s}',\omega)]=\frac{1}{2i}\mathsf{P}\int_{-\infty}^\infty d\omega\omega\mathsf{G}(\mathbf{s},\mathbf{s}',\omega), \tag{B18}$$

where P denotes the Cauchy principal value. Using contour integration, exploiting the facts that the Green tensor is holomorphic in the upper complex frequency plane, that it approaches $\mathsf{G}(\mathbf{s},\mathbf{s}',\omega)\sim-c^2\mathbb{1}\delta(\mathbf{s}-\mathbf{s}')/\omega^2$ for large ω [91], and that it is longitudinal with Eq. (C5) for ω towards zero, the integral can be evaluated as

$$\begin{aligned}\frac{1}{2i}\mathsf{P}\int_{-\infty}^\infty d\omega\,\omega\mathsf{G}(\mathbf{s},\mathbf{s}',\omega)=&-\frac{\pi}{2\mu_0}\frac{\partial}{\partial\mathbf{s}}\otimes\frac{\partial}{\partial\mathbf{s}'}g(\mathbf{s},\mathbf{s}',0)\\&+\frac{\pi c^2}{2}\mathbb{1}\delta(\mathbf{s}-\mathbf{s}').\end{aligned} \tag{B19}$$

Consequently, the surface-interaction Hamiltonian contains the negative electrostatic self-energy of the rigid particle charge distribution and an additional contribution due to the electrostatic interaction of particle and the dielectric,

$$\begin{aligned}H_{\mathrm{SI}}=\frac{1}{2}\int d^3sd^3s'\Bigg[&-\frac{\varrho_0(\mathbf{s})\varrho_0(\mathbf{s}')}{4\pi\varepsilon_0|\mathbf{s}-\mathbf{s}'|}\\&+\varrho_0[\mathsf{R}_\Omega^{\mathrm{T}}(\mathbf{s}-\mathbf{R})]\varrho_0[\mathsf{R}_\Omega^{\mathrm{T}}(\mathbf{s}'-\mathbf{R})]g(\mathbf{s},\mathbf{s}',0)\Bigg].\end{aligned} \tag{B20}$$

The self-energy, given by the first term, is independent of the particle operators $\mathbf{R}$ and R_Ω and thus does not have an impact on the particle dynamics in the slow-particle limit.

The second term gives the image-charge interaction. It is the potential energy of a classical charge distribution due to the presence of a dielectric surface. For instance, a monopole with $\varrho_0(\mathbf{r})=q\delta(\mathbf{r}-\mathbf{R})$ in front of a Drude-metal half-space (see Table III in Appendix C 4) with permittivity (46), experiences the image potential

$$H_{\mathrm{SI}}=-\frac{1}{2}\frac{q^2}{4\pi\epsilon_0}\frac{1}{|2\mathbf{R}\cdot\mathbf{e}_3|}. \tag{B21}$$

Note that Eq. (B20) correctly describes the classically expected image potential, even though the total state is uncorrelated, because the second-order perturbative Born-Markov approximation still accounts for particle-induced displacement of the polarization oscillators.

The master equation (B16) can be brought into Lindblad form using relation (B9):

$$\begin{aligned}\frac{\partial\rho}{\partial t}=&-\frac{i}{\hbar}[H_0+H_{\mathrm{SI}},\rho]+\frac{\varepsilon_0}{\hbar}\lim_{\omega\downarrow0}\frac{2k_BT}{\hbar\omega}\int d^3r\Bigg[\frac{\mathrm{Im}[\varepsilon_r(\mathbf{r},\omega)]}{|\varepsilon_r(\mathbf{r},\omega)|^2}\\&\times\left(\mathbf{L}_e(\mathbf{r})\cdot\rho\mathbf{L}_e^\dagger(\mathbf{r})-\frac{1}{2}\{\mathbf{L}_e^\dagger(\mathbf{r})\cdot\mathbf{L}_e(\mathbf{r}),\rho\}\right)\\&+\frac{\mathrm{Im}[\mu_r(\mathbf{r},\omega)]}{|\mu_r(\mathbf{r},\omega)|^2}\left(\mathbf{L}_m(\mathbf{r})\cdot\rho\mathbf{L}_m^\dagger(\mathbf{r})\right.\\&\left.-\frac{1}{2}\{\mathbf{L}_m^\dagger(\mathbf{r})\cdot\mathbf{L}_m(\mathbf{r}),\rho\}\right)\Bigg]\end{aligned} \tag{B22}$$

with Lindblad operators

$$\mathbf{L}_e(\mathbf{r})=\lim_{\omega\downarrow0}\frac{\mu_0\omega^2}{4\pi}\varepsilon_r(\mathbf{r},\omega)\int d^3s\mathsf{G}(\mathbf{r},\mathbf{s},\omega)\mathbf{C}(\mathbf{s},0), \tag{B23}$$

$$\mathbf{L}_m(\mathbf{r})=\lim_{\omega\downarrow0}\frac{\mu_0\omega c}{4\pi}\int d^3s\frac{\partial}{\partial\mathbf{r}}\times\mathsf{G}(\mathbf{r},\mathbf{s},\omega)\mathbf{C}(\mathbf{s},0). \tag{B24}$$

TABLE III. The Green function for a dielectric half-space with $\varepsilon_r(\omega)$ for $\mathbf{r}\cdot\mathbf{e}_3 < 0$ and vacuum for $\mathbf{r}\cdot\mathbf{e}_3 > 0$.

$g(\mathbf{r},\mathbf{r}',\omega)$	$\mathbf{r}\cdot\mathbf{e}_3 < 0$	$0 < \mathbf{r}\cdot\mathbf{e}_3$
$\mathbf{r}'\cdot\mathbf{e}_3 < 0$	$\frac{1}{4\pi\varepsilon_0\varepsilon_r(\omega)}\left(\frac{1}{\lvert\mathbf{r}-\mathbf{r}'\rvert} - \frac{1-\varepsilon_r(\omega)}{1+\varepsilon_r(\omega)}\frac{1}{\lvert\mathbf{r}-\mathsf{M}\mathbf{r}'\rvert}\right)$	$\frac{1}{4\pi\varepsilon_0}\frac{2}{1+\varepsilon_r(\omega)}\frac{1}{\lvert\mathbf{r}-\mathbf{r}'\rvert}$
$0 < \mathbf{r}'\cdot\mathbf{e}_3$	$\frac{1}{4\pi\varepsilon_0}\frac{2}{1+\varepsilon_r(\omega)}\frac{1}{\lvert\mathbf{r}-\mathbf{r}'\rvert}$	$\frac{1}{4\pi\varepsilon_0}\left(\frac{1}{\lvert\mathbf{r}-\mathbf{r}'\rvert} + \frac{1-\varepsilon_r(\omega)}{1+\varepsilon_r(\omega)}\frac{1}{\lvert\mathbf{r}-\mathsf{M}\mathbf{r}'\rvert}\right)$

In the quasistatic approximation, the Green tensor is longitudinal and takes the form (C5). As a result, $\mathbf{L}_m(\mathbf{r}) = 0$, so that the master equation simplifies to

$$\frac{\partial\rho}{\partial t} = -\frac{i}{\hbar}[H_0 + H_{\mathrm{SI}}, \rho] + \frac{\varepsilon_0}{\hbar}\lim_{\omega\downarrow 0}\frac{2k_BT}{\hbar\omega}\int d^3r\,\frac{\mathrm{Im}[\varepsilon_r(\mathbf{r},\omega)]}{|\varepsilon_r(\mathbf{r},\omega)|^2}\left(\mathbf{L}_e(\mathbf{r})\cdot\rho\mathbf{L}_e^\dagger(\mathbf{r}) - \frac{1}{2}\{\mathbf{L}_e^\dagger(\mathbf{r})\cdot\mathbf{L}_e(\mathbf{r}),\rho\}\right) \tag{B25}$$

with

$$\mathbf{L}_e(\mathbf{r}) = \int d^3s\varrho_0[\mathsf{R}_\Omega^{\mathrm{T}}(\mathbf{s}-\mathbf{R})]\lim_{\omega\downarrow 0}\varepsilon_r(\mathbf{r},\omega)\frac{\partial}{\partial\mathbf{r}}g(\mathbf{r},\mathbf{s},\omega), \tag{B26}$$

where we have performed a partial integration. The charge distribution enters through

$$\frac{\partial}{\partial\mathbf{s}}\cdot\mathbf{C}(\mathbf{s},0) = 4\pi\varrho_0[\mathsf{R}_\Omega^{\mathrm{T}}(\mathbf{s}-\mathbf{R})], \tag{B27}$$

as a direct consequence of definition (B3).

Having shown that the master equation has Lindblad form, we can again use Eq. (6) to simplify the master equation in the quasistatic limit, yielding Eq. (15). This equation may also be obtained directly by inserting the quasistatic Green tensor (C5) into Eq. (B16) and subsequently carrying out partial integrations.

3. Resonant limit

A Markovian master equation can also be derived in the limit that the free particle dynamics are much faster than the bath-induced particle-relaxation time. We start from the non-Markovian evolution equation (B12) and expand the Coulomb field operator (B3) in eigenoperators $\mathbf{C}_\ell(\mathbf{s})$ of the free evolution,

$$\mathbf{C}(\mathbf{s},t) = \mathbf{C}_0(\mathbf{s}) + \left(\sum_{\omega_\ell>0}\mathbf{C}_\ell(\mathbf{s})e^{-i\omega_\ell t} + \mathrm{H.c.}\right). \tag{B28}$$

The index ℓ covers all positive energy differences $\hbar\omega_\ell$. We express

$$\mathbf{C}_\ell(\mathbf{s}) = \sum_{\substack{n,m\\ E_m-E_n=\hbar\omega_\ell>0}}\mathbf{C}_{nm}(\mathbf{s})\,|\Psi_n\rangle\langle\Psi_m|\,, \tag{B29}$$

$$\mathbf{C}_0(\mathbf{s}) = \sum_{\substack{n,m\\ E_m-E_n=0}}\mathbf{C}_{nm}(\mathbf{s})\,|\Psi_n\rangle\langle\Psi_m| \tag{B30}$$

through the eigenstates $|\Psi_n\rangle$ of H_0 with energies E_n and coefficients

$$\mathbf{C}_{nm}(\mathbf{s}) = \langle\Psi_n|\int d^3r\varrho_0(\mathbf{r})\frac{\mathbf{s}-\mathbf{R}-\mathsf{R}_\Omega\mathbf{r}}{|\mathbf{s}-\mathbf{R}-\mathsf{R}_\Omega\mathbf{r}|^3}\,|\Psi_m\rangle\,. \tag{B31}$$

The operators $c_\ell(\mathbf{s})$ in Eq. (20) expand the charge distribution,

$$U_0^\dagger(t)\varrho_0[\mathsf{R}_\Omega^{\mathrm{T}}(\mathbf{r}-\mathbf{R})]U_0(t) = c_0(\mathbf{r}) + \left(\sum_{\omega_\ell>0}c_\ell(\mathbf{r})e^{-i\omega_\ell t} + \mathrm{H.c.}\right), \tag{B32}$$

and are thus related to Eq. (B28) via

$$c_\ell(\mathbf{r}) = \frac{1}{4\pi}\frac{\partial}{\partial \mathbf{r}}\cdot \mathbf{C}_\ell(\mathbf{r}) = \sum_{\substack{n,m \\ E_m - E_n = \hbar\omega_\ell > 0}} c_{nm}(\mathbf{r})\,|\Psi_n\rangle\langle\Psi_m|\,, \tag{B33a}$$

$$c_0(\mathbf{r}) = \frac{1}{4\pi}\frac{\partial}{\partial \mathbf{r}}\cdot \mathbf{C}_0(\mathbf{r}) = \sum_{\substack{n,m \\ E_m - E_n = 0}} c_{nm}(\mathbf{r})\,|\Psi_n\rangle\langle\Psi_m|\,, \tag{B33b}$$

where the coefficients read

$$c_{nm}(\mathbf{r}) = \langle\Psi_n|\,\varrho_0[\mathsf{R}_\Omega^{\mathrm{T}}(\mathbf{r}-\mathbf{R})]\,|\Psi_m\rangle\,. \tag{B34}$$

We define the Fourier integrals of the damping and noise kernel,

$$\Gamma_{\mathsf{D}}(\mathbf{s},\mathbf{s}',\omega) = \int_0^\infty d\tau\, \mathsf{D}(\mathbf{s},\mathbf{s}',\tau)e^{i\omega\tau} = \frac{i\hbar\pi}{(4\pi)^2}\mathsf{J}(\mathbf{s},\mathbf{s}',\omega) + \frac{\hbar}{(4\pi)^2}\mathsf{P}\int_{-\infty}^\infty d\omega'\frac{\mathsf{J}(\mathbf{s},\mathbf{s}',\omega')}{\omega'-\omega} \tag{B35}$$

and

$$\Gamma_{\mathsf{N}}(\mathbf{s},\mathbf{s}',\omega) = \int_0^\infty d\tau\, \mathsf{N}(\mathbf{s},\mathbf{s}',\tau)e^{i\omega\tau} = \frac{\hbar\pi}{(4\pi)^2}\mathsf{J}(\mathbf{s},\mathbf{s}',\omega)\coth\left(\frac{\hbar\omega}{2k_BT}\right) - \frac{i\hbar}{(4\pi)^2}\mathsf{P}\int_{-\infty}^\infty d\omega'\frac{\mathsf{J}(\mathbf{s},\mathbf{s}',\omega')}{\omega'-\omega}\coth\left(\frac{\hbar\omega'}{2k_BT}\right), \tag{B36}$$

in order to write

$$\left[\int_0^\infty d\tau\, \mathsf{N}(\mathbf{s},\mathbf{s}',\tau)\mathbf{C}(\mathbf{s}',t-\tau),\tilde{\rho}(t)\right] = \sum_{\omega_\ell>0}\left[\Gamma_{\mathsf{N}}(\mathbf{s},\mathbf{s}',\omega_\ell)\mathbf{C}_\ell(\mathbf{s}')e^{-i\omega_\ell t} + \Gamma_{\mathsf{N}}(\mathbf{s},\mathbf{s}',-\omega_\ell)\mathbf{C}_\ell^\dagger(\mathbf{s}')e^{i\omega_\ell t},\tilde{\rho}(t)\right]. \tag{B37}$$

Here we have assumed that the time-independent term in Eq. (B28), $\mathbf{C}_0(\mathbf{s})$, is a c number, as it is the case in all situations discussed in the main text. The case of an operator-valued $\mathbf{C}_0(\mathbf{s})$ could be included along the lines of the derivation in the slow-particle limit in Sec. B 2.

With Eq. (B37) we find that

$$\begin{aligned}&\left[\mathbf{C}(\mathbf{s},t),\left[\int_0^\infty d\tau\, \mathsf{N}(\mathbf{s},\mathbf{s}',\tau)\mathbf{C}(\mathbf{s}',t-\tau),\tilde{\rho}(t)\right]\right]\\ &\quad= \left[\sum_{\omega_n>0}\mathbf{C}_n(\mathbf{s})e^{-i\omega_n t} + \mathrm{H.c.},\left[\sum_{\omega_\ell>0}\Gamma_{\mathsf{N}}(\mathbf{s},\mathbf{s}',\omega_\ell)\mathbf{C}_\ell(\mathbf{s}')e^{-i\omega_\ell t} + \sum_{\omega_\ell>0}\Gamma_{\mathsf{N}}(\mathbf{s},\mathbf{s}',-\omega_\ell)\mathbf{C}_\ell^\dagger(\mathbf{s}')e^{i\omega_\ell t},\tilde{\rho}(t)\right]\right].\end{aligned} \tag{B38}$$

If the free particle dynamics are fast, so that all frequencies and frequency differences are much larger than the rate at which the density operator $\tilde{\rho}(t)$ relaxes, we can carry out the rotating-wave approximation and cancel all rapidly oscillating terms. This yields

$$\begin{aligned}&\int_0^\infty d\tau\left[\mathbf{C}(\mathbf{s},t),\left[\mathsf{N}(\mathbf{s},\mathbf{s}',\tau)\mathbf{C}(\mathbf{s}',t-\tau),\tilde{\rho}(t)\right]\right]\\ &\quad\simeq \sum_{\omega_\ell>0}\left[\mathbf{C}_\ell^\dagger(\mathbf{s}),\left[\Gamma_{\mathsf{N}}(\mathbf{s},\mathbf{s}',\omega_\ell)\mathbf{C}_\ell(\mathbf{s}'),\tilde{\rho}(t)\right]\right] + \sum_{\omega_\ell>0}\left[\mathbf{C}_\ell(\mathbf{s}),\left[\Gamma_{\mathsf{N}}(\mathbf{s},\mathbf{s}',-\omega_\ell)\mathbf{C}_\ell^\dagger(\mathbf{s}'),\tilde{\rho}(t)\right]\right].\end{aligned} \tag{B39}$$

Along the same lines one finds that

$$\begin{aligned}&\int_0^\infty d\tau\left[\mathbf{C}(\mathbf{s},t),\left\{\mathsf{D}(\mathbf{s},\mathbf{s}',\tau)\mathbf{C}(\mathbf{s}',t-\tau),\tilde{\rho}(t)\right\}\right]\\ &\quad\simeq \sum_{\omega_\ell>0}\left[\mathbf{C}_\ell^\dagger(\mathbf{s}),\left\{\Gamma_{\mathsf{D}}(\mathbf{s},\mathbf{s}',\omega_\ell)\mathbf{C}_\ell(\mathbf{s}'),\tilde{\rho}(t)\right\}\right] + \sum_{\omega_\ell>0}\left[\mathbf{C}_\ell(\mathbf{s}),\left\{\Gamma_{\mathsf{D}}(\mathbf{s},\mathbf{s}',-\omega_\ell)\mathbf{C}_\ell^\dagger(\mathbf{s}'),\tilde{\rho}(t)\right\}\right].\end{aligned} \tag{B40}$$

Inserting Eqs. (B39) and (B40) with Eqs. (B35) and (B36) into Eq. (B12) and transforming back to the Schrödinger picture yields a Markovian master equation,

$$\frac{\partial\rho}{\partial t} = -\frac{i}{\hbar}[H_0 + H_{\rm SI}, \rho] + \frac{1}{8\pi\hbar}\int d^3s d^3s' \sum_{\omega_\ell>0}\Bigg([n(\omega_\ell)+1]\Big[\mathbf{C}_\ell(\mathbf{s})\cdot\rho\mathsf{J}(\mathbf{s},\mathbf{s}',\omega_\ell)\mathbf{C}_\ell^\dagger(\mathbf{s}') - \frac{1}{2}\{\mathbf{C}_\ell^\dagger(\mathbf{s})\cdot\mathsf{J}(\mathbf{s},\mathbf{s}',\omega_\ell)\mathbf{C}_\ell(\mathbf{s}'),\rho\}\Big] + n(\omega_\ell)\Big[\mathbf{C}_\ell^\dagger(\mathbf{s})\cdot\rho\mathsf{J}(\mathbf{s},\mathbf{s}',\omega_\ell)\mathbf{C}_\ell(\mathbf{s}') - \frac{1}{2}\{\mathbf{C}_\ell(\mathbf{s})\cdot\mathsf{J}(\mathbf{s},\mathbf{s}',\omega_\ell)\mathbf{C}_\ell^\dagger(\mathbf{s}'),\rho\}\Big]\Bigg), \tag{B41}$$

after a rearrangement that uses the symmetries in ω, $\mathbf{s}$, and $\mathbf{s}'$. Here

$$H_{\rm SI} = \frac{1}{(4\pi)^2}\int d^3s d^3s' \sum_{\omega_\ell>0} \mathsf{P}\int_{-\infty}^{\infty} d\omega \frac{1}{\omega_\ell-\omega}\big([n(\omega)+1]\mathbf{C}_\ell^\dagger(\mathbf{s})\cdot\mathsf{J}(\mathbf{s},\mathbf{s}',\omega)\mathbf{C}_\ell(\mathbf{s}') - n(\omega)\mathbf{C}_\ell(\mathbf{s})\cdot\mathsf{J}(\mathbf{s},\mathbf{s}',\omega)\mathbf{C}_\ell^\dagger(\mathbf{s}')\big) \tag{B42}$$

describes the coherent surface interaction in the resonant limit. The two principal-value integrals can be evaluated using contour integration. We express the imaginary part of the Green tensor through the total Green tensor and use the Schwarz reflection principle to then exploit that the Green tensor is holomorphic in the positive imaginary plane. Accounting for the pole at $\omega=\omega_\ell$, all the poles of $n(\omega)$ in the positive imaginary plane and at $\omega=0$, and for the behavior of the integrand at infinity, the two integrals yield

$$\mathsf{P}\int_{-\infty}^{\infty} d\omega \frac{1}{\omega_\ell-\omega}\mathsf{J}(\mathbf{s},\mathbf{s}',\omega) = -\mu_0 c^2 \mathbb{1}\delta(\mathbf{s}-\mathbf{s}') - \mu_0\omega_\ell^2 \mathrm{Re}[\mathsf{G}(\mathbf{s},\mathbf{s}',\omega_\ell)] \tag{B43a}$$

and

$$\mathsf{P}\int_{-\infty}^{\infty} d\omega \frac{1}{\omega_\ell-\omega} n(\omega)\mathsf{J}(\mathbf{s},\mathbf{s}',\omega) = \frac{\mu_0 c^2}{2}\mathbb{1}\delta(\mathbf{s}-\mathbf{s}') - \mu_0\omega_\ell^2 n(\omega_\ell)\mathrm{Re}[\mathsf{G}(\mathbf{s},\mathbf{s}',\omega_\ell)] + \frac{\mu_0\omega_{\rm th}}{2\pi\omega_\ell}\lim_{\omega\to 0}\omega^2\mathsf{G}(\mathbf{s},\mathbf{s}',\omega) - \frac{\mu_0\omega_{\rm th}\omega_\ell}{\pi}\sum_{m=1}^{\infty}\frac{(\omega_{\rm th}m)^2}{\omega_\ell^2+(\omega_{\rm th}m)^2}\mathsf{G}(\mathbf{s},\mathbf{s}',i\omega_{\rm th}m). \tag{B43b}$$

Here $\omega_{\rm th} = 2\pi k_B T/\hbar$ denotes the thermal Matsubara frequency. In the limit $T\to 0$ the Matsubara frequency summation transforms into an ordinary integral that is independent of temperature. In the quasistatic limit (C5) one then obtains Eq. (24).

Similar to the slow-particle limit we now briefly give the result for a particle in front of a perfectly conducting half-space. The quasistatic Green tensor (C5) in front of a perfectly conducting half space (see Table III in Appendix C 4) reads

$$\mathsf{G}(\mathbf{s},\mathbf{s}',\omega) = -\frac{c^2}{\omega^2}\frac{1}{4\pi}\frac{\partial}{\partial\mathbf{s}}\otimes\frac{\partial}{\partial\mathbf{s}'}\frac{1}{|\mathbf{s}-\mathbf{s}'|} + \frac{c^2}{\omega^2}\frac{1}{4\pi}\frac{\partial}{\partial\mathbf{s}}\otimes\frac{\partial}{\partial\mathbf{s}'}\frac{1}{|\mathbf{s}-\mathsf{M}\mathbf{s}'|}, \tag{B44}$$

yielding for Eqs. (B43a) and (B43b) temperature-independent expressions,

$$\mathsf{P}\int_{-\infty}^{\infty} d\omega \frac{1}{\omega_\ell-\omega}\mathsf{J}(\mathbf{s},\mathbf{s}',\omega) = -\mu_0 c^2\delta^\perp(\mathbf{s}-\mathbf{s}') - \mu_0 c^2\frac{1}{4\pi}\frac{\partial}{\partial\mathbf{s}}\otimes\frac{\partial}{\partial\mathbf{s}'}\frac{1}{|\mathbf{s}-\mathsf{M}\mathbf{s}'|}, \tag{B45a}$$

$$\mathsf{P}\int_{-\infty}^{\infty} d\omega \frac{1}{\omega_\ell-\omega} n(\omega)\mathsf{J}(\mathbf{s},\mathbf{s}',\omega) = \frac{\mu_0 c^2}{2}\delta^\perp(\mathbf{s}-\mathbf{s}') + \frac{\mu_0 c^2}{2}\frac{1}{4\pi}\frac{\partial}{\partial\mathbf{s}}\otimes\frac{\partial}{\partial\mathbf{s}'}\frac{1}{|\mathbf{s}-\mathsf{M}\mathbf{s}'|}. \tag{B45b}$$

The surface-interaction Hamiltonian (B42) can now be evaluated. The transverse delta function does not contribute and one finds that

$$H_{\rm SI} = -\frac{1}{2}\frac{1}{4\pi\varepsilon_0}\sum_{\omega_\ell>0}\int d^3s d^3s' \frac{1}{|\mathbf{s}-\mathsf{M}\mathbf{s}'|}\{c_\ell^\dagger(\mathbf{s}), c_\ell(\mathbf{s}')\}, \tag{B46}$$

after a partial integration by use of Eq. (B33). A small-amplitude oscillating monopole with Eq. (30) and a single frequency ω_0, oscillation direction $\boldsymbol{\epsilon}_0$, and annihilation operator a_0 is consequently exposed to the potential

$$H_{\rm SI} = -\frac{q^2}{4\pi\varepsilon_0}\frac{\hbar}{2m\omega_0}\frac{1}{(2\mathbf{R}_{\rm eq}\cdot\mathbf{e}_3)^3}[1+(\boldsymbol{\epsilon}_0\cdot\mathbf{e}_3)^2]a_0^\dagger a_0. \tag{B47}$$

Here $\mathbf{e}_3$ is the surface normal. This quantum potential could also be derived by taking the classical image-charge potential of an extended charge distribution, promoting the charge distribution to an operator, accounting for the small-amplitude oscillations of the monopole, and carrying out a rotating-wave approximation.

To demonstrate that Eq. (B41) has Lindblad form, we use Eq. (B9) to obtain

$$\begin{aligned}\frac{\partial\rho}{\partial t} = &-\frac{i}{\hbar}[H_0+H_{\rm SI},\rho] + \frac{\varepsilon_0}{\hbar}\sum_{\omega_\ell>0}\int d^3r\frac{{\rm Im}[\varepsilon_r(\mathbf{r},\omega_\ell)]}{|\varepsilon_r(\mathbf{r},\omega_\ell)|^2}\Bigg[[n(\omega_\ell)+1]\left(\mathbf{L}_\ell^e(\mathbf{r})\cdot\rho\mathbf{L}_\ell^{e\dagger}(\mathbf{r}) - \frac{1}{2}\{\mathbf{L}_\ell^{e\dagger}(\mathbf{r})\cdot\mathbf{L}_\ell^e(\mathbf{r}),\rho\}\right)\\
&+ n(\omega_\ell)\left(\mathbf{L}_\ell^{e\dagger}(\mathbf{r})\cdot\rho\mathbf{L}_\ell^e(\mathbf{r}) - \frac{1}{2}\{\mathbf{L}_\ell^e(\mathbf{r})\cdot\mathbf{L}_\ell^{e\dagger}(\mathbf{r}),\rho\}\right)\Bigg] + \frac{\varepsilon_0}{\hbar}\sum_{\omega_\ell>0}\int d^3r\frac{{\rm Im}[\mu_r(\mathbf{r},\omega_\ell)]}{|\mu_r(\mathbf{r},\omega_\ell)|^2}\\
&\times\Bigg[[n(\omega_\ell)+1]\left(\mathbf{L}_\ell^m(\mathbf{r})\cdot\rho\mathbf{L}_\ell^{m\dagger}(\mathbf{r}) - \frac{1}{2}\{\mathbf{L}_\ell^{m\dagger}(\mathbf{r})\cdot\mathbf{L}_\ell^m(\mathbf{r}),\rho\}\right)\\
&+ n(\omega_\ell)\left(\mathbf{L}_\ell^{m\dagger}(\mathbf{r})\cdot\rho\mathbf{L}_\ell^m(\mathbf{r}) - \frac{1}{2}\{\mathbf{L}_\ell^m(\mathbf{r})\cdot\mathbf{L}_\ell^{m\dagger}(\mathbf{r}),\rho\}\right)\Bigg]\end{aligned} \tag{B48}$$

with Lindblad operators

$$\mathbf{L}_\ell^e(\mathbf{r}) = \frac{\sqrt{2}\mu_0\omega_\ell^2}{4\pi}\varepsilon_r(\mathbf{r},\omega_\ell)\int d^3s\,\mathsf{G}(\mathbf{r},\mathbf{s},\omega_\ell)\mathbf{C}_\ell(\mathbf{s}), \tag{B49}$$

$$\mathbf{L}_\ell^m(\mathbf{r}) = \frac{\sqrt{2}\mu_0\omega_\ell c}{4\pi}\int d^3s\frac{\partial}{\partial\mathbf{r}}\times\mathsf{G}(\mathbf{r},\mathbf{s},\omega_\ell)\mathbf{C}_\ell(\mathbf{s}). \tag{B50}$$

In case of a longitudinal Green tensor of the form (C5), $\mathbf{L}_\ell^m(\mathbf{r}) = 0$, and the Lindblad master equation reduces to

$$\begin{aligned}\frac{\partial\rho}{\partial t} = &-\frac{i}{\hbar}[H_0+H_{\rm SI},\rho] + \frac{\varepsilon_0}{\hbar}\sum_{\omega_\ell>0}\int d^3r\,\frac{{\rm Im}[\varepsilon_r(\mathbf{r},\omega_\ell)]}{|\varepsilon_r(\mathbf{r},\omega_\ell)|^2}\Bigg[[n(\omega_\ell)+1]\left(\mathbf{L}_\ell^e(\mathbf{r})\cdot\rho\mathbf{L}_\ell^{e\dagger}(\mathbf{r}) - \frac{1}{2}\{\mathbf{L}_\ell^{e\dagger}(\mathbf{r})\cdot\mathbf{L}_\ell^e(\mathbf{r}),\rho\}\right)\\
&+ n(\omega_\ell)\left(\mathbf{L}_\ell^{e\dagger}(\mathbf{r})\cdot\rho\mathbf{L}_\ell^e(\mathbf{r}) - \frac{1}{2}\{\mathbf{L}_\ell^e(\mathbf{r})\cdot\mathbf{L}_\ell^{e\dagger}(\mathbf{r}),\rho\}\right)\Bigg].\end{aligned} \tag{B51}$$

The rates are positive since ${\rm Im}[\varepsilon_r(\mathbf{r},\omega_\ell)] \geq 0$.

To simplify the Lindblad master equation (B51) to a scalar form, we can insert the quasistatic Green tensor (C5),

$$\mathbf{L}_\ell^e(\mathbf{r}) = \sqrt{2}\int d^3s c_\ell(\mathbf{s})\varepsilon_r(\mathbf{r},\omega_\ell)\frac{\partial}{\partial\mathbf{r}}g(\mathbf{r},\mathbf{s},\omega_\ell). \tag{B52}$$

Here the Lindblad operators do not depend on the $\mathbf{C}_\ell(\mathbf{s})$, but instead involve the operators $c_\ell(\mathbf{s})$ used to expand the charge distribution. We use relation (6) to finally arrive at Eq. (25). Similar to the slow-particle limit, this equation may also be obtained directly by inserting the quasistatic Green tensor (C5) into Eq. (B41) and subsequently carrying out partial integrations.

APPENDIX C: QUASISTATIC APPROXIMATION OF THE GREEN TENSOR

Depending on the material response $\varepsilon_r(\mathbf{r},\omega)$, the frequency, and the distance $|\mathbf{r}-\mathbf{r}'|$, retardation effects in the propagation of the electromagnetic field to the particle can be neglected. In this quasistatic limit, the Fourier-transformed electric field

$$\mathbf{E}(\mathbf{r},\omega)=\int_{-\infty}^{\infty}dt\mathbf{E}(\mathbf{r},t)e^{i\omega t} \tag{C1}$$

generated by an arbitrary charge distribution $\varrho(\mathbf{r},\omega)$ follows as the solution of the quasistatic Maxwell equations

$$\frac{\partial}{\partial\mathbf{r}}\cdot\varepsilon_0\varepsilon_r(\mathbf{r},\omega)\mathbf{E}(\mathbf{r},\omega)=\varrho(\mathbf{r},\omega), \tag{C2a}$$

$$\frac{\partial}{\partial\mathbf{r}}\times\mathbf{E}(\mathbf{r},\omega)=0. \tag{C2b}$$

The charge distribution is related to the current density by the continuity equation

$$-i\omega\varrho(\mathbf{r},\omega)+\frac{\partial}{\partial\mathbf{r}}\cdot\mathbf{j}(\mathbf{r},\omega)=0. \tag{C3}$$

Expressing the electric field in terms of the Green tensor and using Eq. (A28), the quasistatic Maxwell equations (C2) can be rewritten as

$$\frac{\partial}{\partial\mathbf{r}}\cdot\varepsilon_r(\mathbf{r},\omega)\mathsf{G}(\mathbf{r},\mathbf{r}',\omega)=-\frac{c^2}{\omega^2}\frac{\partial}{\partial\mathbf{r}}\delta(\mathbf{r}-\mathbf{r}'), \tag{C4a}$$

$$\frac{\partial}{\partial\mathbf{r}}\times\mathsf{G}(\mathbf{r},\mathbf{r}',\omega)=\mathbf{0}. \tag{C4b}$$

They are solved by

$$\mathsf{G}(\mathbf{r},\mathbf{r}',\omega)=-\frac{1}{\mu_0\omega^2}\frac{\partial}{\partial\mathbf{r}}\otimes\frac{\partial}{\partial\mathbf{r}'}g(\mathbf{r},\mathbf{r}',\omega), \tag{C5}$$

where the scalar Green function $g(\mathbf{r},\mathbf{r}',\omega)$ is the solution of

$$\frac{\partial}{\partial\mathbf{r}}\cdot\left[\varepsilon_0\varepsilon_r(\mathbf{r},\omega)\frac{\partial}{\partial\mathbf{r}}g(\mathbf{r},\mathbf{r}',\omega)\right]=-\delta(\mathbf{r}-\mathbf{r}'). \tag{C6}$$

Comparing Eqs. (C6) and (A26) shows that the complexity of the problem is considerably reduced. It follows from the defining equation (C6) and from the Schwarz reflection principle for the dielectric response that the Schwarz reflection principle holds for the Green function $g^*(\mathbf{r},\mathbf{r}',\omega)=g(\mathbf{r},\mathbf{r}',-\omega^*)$.

The boundary conditions of the problem can be deduced by inserting Eq. (C5) into the electric field (A28) and carrying out a partial integration,

$$\begin{aligned}\mathbf{E}(\mathbf{r},\omega)&=\frac{i}{\omega}\int d^3r'\left[\frac{\partial}{\partial\mathbf{r}}g(\mathbf{r},\mathbf{r}',\omega)\right]\frac{\partial}{\partial\mathbf{r}'}\cdot\mathbf{j}(\mathbf{r}',\omega)\\&=-\int d^3r'\left[\frac{\partial}{\partial\mathbf{r}}g(\mathbf{r},\mathbf{r}',\omega)\right]\varrho(\mathbf{r}',\omega).\end{aligned} \tag{C7}$$

To ensure that the electric field vanishes infinitely far from the source, one requires that $\partial g(\mathbf{r},\mathbf{r}',\omega)/\partial\mathbf{r}=0$ for $|\mathbf{r}-\mathbf{r}'|\to\infty$. Equation (C6) determines $g(\mathbf{r},\mathbf{r}',\omega)$ up to a constant, so that we can set $g(\mathbf{r},\mathbf{r}',\omega)=0$ for $|\mathbf{r}-\mathbf{r}'|\to\infty$, as is beneficial for partial integration. From Eq. (C7) we can see that $g(\mathbf{r},\mathbf{r}',\omega)$ yields the quasielectrostatic potential at $\mathbf{r}$ of a test charge located at $\mathbf{r}'$ oscillating in magnitude with ω. Inserting Eq. (C5) into the scalar potential (A35), a subsequent partial integration yields, after transforming to the interaction picture, the simplified form (7).

1. Continuity at an interface

At an interface $\varepsilon_r(\mathbf{r},\omega)$ changes discontinuously, so that the defining equation (C6) implies continuity conditions. These conditions will be used in Appendices C 4 and C 5 to derive the scalar Green function of the dielectric half-space and the dielectric layer configuration.

For example, for a flat interface between two homogeneous dielectrics with $\varepsilon_r(\mathbf{r},\omega)=\varepsilon_<$ for $\mathbf{r}\cdot\mathbf{e}_3<0$ and $\varepsilon_r(\mathbf{r},\omega)=\varepsilon_>$ for $\mathbf{r}\cdot\mathbf{e}_3>0$, volume integration at the boundary gives the condition

$$\varepsilon_>\mathbf{e}_3\cdot\frac{\partial}{\partial\mathbf{r}}g(\mathbf{r}_>,\mathbf{r}',\omega)=\varepsilon_<\mathbf{e}_3\cdot\frac{\partial}{\partial\mathbf{r}}g(\mathbf{r}_<,\mathbf{r}',\omega), \tag{C8a}$$

where $\mathbf{r}_>$ and $\mathbf{r}_<$ approach the surface from above and below. This expresses the continuity of the displacement field's normal component.

Likewise, by integrating over a loop through the interface we find the continuity for the electric field's parallel component

$$\mathbf{e}_\parallel\cdot\frac{\partial}{\partial\mathbf{r}}g(\mathbf{r}_>,\mathbf{r}',\omega)=\mathbf{e}_\parallel\cdot\frac{\partial}{\partial\mathbf{r}}g(\mathbf{r}_<,\mathbf{r}',\omega), \tag{C8b}$$

where $\mathbf{e}_\parallel$ is perpendicular to $\mathbf{e}_3$.

2. Symmetry of the Green function

To prove the relation (6), we first show that

$$g(\mathbf{r},\mathbf{r}',\omega) = g(\mathbf{r}',\mathbf{r},\omega). \tag{C9}$$

This symmetry follows directly from multiplying Eq. (C6) by $g(\mathbf{s},\mathbf{r},\omega)$ and integrating over $\mathbf{r}$ to obtain

$$\varepsilon_0 \int d^3r\, g(\mathbf{s},\mathbf{r},\omega)\frac{\partial}{\partial \mathbf{r}}\cdot\left[\varepsilon_r(\mathbf{r},\omega)\frac{\partial}{\partial \mathbf{r}}g(\mathbf{r},\mathbf{r}',\omega)\right] = -g(\mathbf{s},\mathbf{r}',\omega). \tag{C10}$$

Two partial integrations then yield

$$\varepsilon_0 \int d^3r \left(\frac{\partial}{\partial \mathbf{r}}\cdot\left[\varepsilon_r(\mathbf{r},\omega)\frac{\partial}{\partial \mathbf{r}}g(\mathbf{s},\mathbf{r},\omega)\right]\right) g(\mathbf{r},\mathbf{r}',\omega) = -g(\mathbf{s},\mathbf{r}',\omega). \tag{C11}$$

This equation is valid for all $\mathbf{s}$, $\mathbf{r}'$, and ω, so that

$$\varepsilon_0\frac{\partial}{\partial \mathbf{r}}\cdot\left[\varepsilon_r(\mathbf{r},\omega)\frac{\partial}{\partial \mathbf{r}}g(\mathbf{s},\mathbf{r},\omega)\right] = -\delta(\mathbf{r}-\mathbf{s}) \tag{C12}$$

must hold. Renaming $\mathbf{s}$ by $\mathbf{r}'$ and comparing the equation with Eq. (C6) shows that $g(\mathbf{r},\mathbf{r}',\omega)$ and $g(\mathbf{r}',\mathbf{r},\omega)$ solve the same defining equation with the same boundary conditions and, thus, that they are equal.

3. A useful relation

We are now in the position to prove Eq. (6). We start with the defining equation

$$\varepsilon_0\frac{\partial}{\partial \mathbf{s}}\cdot\left[\varepsilon_r(\mathbf{s},\omega)\frac{\partial}{\partial \mathbf{s}}g(\mathbf{s},\mathbf{r}',\omega)\right] = -\delta(\mathbf{s}-\mathbf{r}'), \tag{C13}$$

multiply it by $g^*(\mathbf{r},\mathbf{s},\omega)$, integrate over $\mathbf{s}$, and perform a partial integration to find that

$$\varepsilon_0 \int d^3s\varepsilon_r(\mathbf{s},\omega)\left(\frac{\partial}{\partial \mathbf{s}}g^*(\mathbf{r},\mathbf{s},\omega)\right)\cdot\left(\frac{\partial}{\partial \mathbf{s}}g(\mathbf{s},\mathbf{r}',\omega)\right) = g^*(\mathbf{r},\mathbf{r}',\omega). \tag{C14}$$

Then taking the complex conjugate of the defining equation

$$\varepsilon_0\frac{\partial}{\partial \mathbf{s}}\cdot\left[\varepsilon_r^*(\mathbf{s},\omega)\frac{\partial}{\partial \mathbf{s}}g^*(\mathbf{s},\mathbf{r},\omega)\right] = -\delta(\mathbf{s}-\mathbf{r}), \tag{C15}$$

multiplying by $g(\mathbf{s},\mathbf{r}',\omega)$, integrating over $\mathbf{s}$, and performing a partial integration yields

$$\varepsilon_0 \int d^3s\varepsilon_r^*(\mathbf{s},\omega)\left(\frac{\partial}{\partial \mathbf{s}}g^*(\mathbf{s},\mathbf{r},\omega)\right)\cdot\left(\frac{\partial}{\partial \mathbf{s}}g(\mathbf{s},\mathbf{r}',\omega)\right) = g(\mathbf{r},\mathbf{r}',\omega). \tag{C16}$$

Symmetry (C9) leads to

$$\varepsilon_0 \int d^3s\varepsilon_r^*(\mathbf{s},\omega)\left(\frac{\partial}{\partial \mathbf{s}}g^*(\mathbf{r},\mathbf{s},\omega)\right)\cdot\left(\frac{\partial}{\partial \mathbf{s}}g(\mathbf{s},\mathbf{r}',\omega)\right) = g(\mathbf{r},\mathbf{r}',\omega). \tag{C17}$$

We then subtract Eqs. (C14) and (C17) to find that

$$\mathrm{Im}[g(\mathbf{r},\mathbf{r}',\omega)] = -\varepsilon_0 \int d^3s\,\mathrm{Im}[\varepsilon_r(\mathbf{s},\omega)]\left(\frac{\partial}{\partial \mathbf{s}}g^*(\mathbf{r},\mathbf{s},\omega)\right)\cdot\left(\frac{\partial}{\partial \mathbf{s}}g(\mathbf{s},\mathbf{r}',\omega)\right). \tag{C18}$$

Subsequent complex conjugation yields Eq. (6).

4. Homogeneous half-space

We now use these results to derive the Green function $g(\mathbf{r},\mathbf{r}',\omega)$ for the dielectric half-space. For a space-filling dielectric $\varepsilon_r(\omega)$, the defining equation (5) is solved by the particular solution

$$g(\mathbf{r},\mathbf{r}',\omega) = \frac{1}{4\pi\varepsilon_0\varepsilon_r(\omega)}\frac{1}{|\mathbf{r}-\mathbf{r}'|}, \tag{C19}$$

which fulfills the boundary condition at infinity.

For the half-space geometry depicted in Table II, where we assume a vacuum for $\mathbf{r}\cdot\mathbf{e}_3 > 0$, while for $\mathbf{r}\cdot\mathbf{e}_3 < 0$, we set $\varepsilon_r(\mathbf{r},\omega) = \varepsilon_r(\omega)$ to be the response of an arbitrary homogeneous dielectric. With $\mathbf{r}'\cdot\mathbf{e}_3 > 0$ in vacuum, the solution can be obtained from the ansatz

$$g(\mathbf{r},\mathbf{r}',\omega) = \frac{1}{4\pi\varepsilon_0}\frac{1}{|\mathbf{r}-\mathbf{r}'|} + \frac{b_1}{4\pi\varepsilon_0}\frac{1}{|\mathbf{r}-\mathsf{M}\mathbf{r}'|}, \quad \mathbf{r}\cdot\mathbf{e}_3 > 0, \tag{C20a}$$

$$g(\mathbf{r},\mathbf{r}',\omega) = \frac{b_2}{4\pi\varepsilon_0}\frac{1}{|\mathbf{r}-\mathbf{r}'|}, \quad \mathbf{r}\cdot\mathbf{e}_3 < 0, \tag{C20b}$$

with the mirror tensor $\mathsf{M} = \mathbb{1} - 2\mathbf{e}_3\otimes\mathbf{e}_3$. The second term in Eq. (C20a) is a homogeneous solution, since $\mathbf{e}_3\cdot\mathsf{M}\mathbf{r}' < 0$. Continuity at the interface (C8) implies that

$$b_1 = \frac{1-\varepsilon_r(\omega)}{1+\varepsilon_r(\omega)}, \tag{C21a}$$

$$b_2 = \frac{2}{1+\varepsilon_r(\omega)}. \tag{C21b}$$

The homogeneous solution can be interpreted as the potential due to the presence of an image charge. The same calculation for $\mathbf{r}'\cdot\mathbf{e}_3 < 0$ in the dielectric yields the entire Green function given in Table III.

5. Half-space covered by a surface layer

We next derive the Green function $g(\mathbf{r},\mathbf{r}',\omega)$ in a geometry consisting of a vacuum half-space with $\varepsilon_r(\mathbf{r},\omega) = 1$ for $\mathbf{r}\cdot\mathbf{e}_3 > 0$, a dielectric layer with $\varepsilon_r(\mathbf{r},\omega) = \varepsilon_s(\omega)$ for $-d_s < \mathbf{r}\cdot\mathbf{e}_3 < 0$, and a dielectric half-space with $\varepsilon_r(\mathbf{r},\omega) = \varepsilon_b(\omega)$ for $\mathbf{r}\cdot\mathbf{e}_3 < -d_s$; see Table II.

In a geometry with two interfaces, an infinite number of image charges appears. We now use a compact formulation by expanding the particular solution (C19) in exponential functions [127],

$$\frac{1}{|\mathbf{r}-\mathbf{r}'|} = \int_0^\infty dk\, J_0(k\Delta r) e^{-k|(\mathbf{r}-\mathbf{r}')\cdot\mathbf{e}_3|} \tag{C22}$$

with the in-plane distance $\Delta r^2 = [(\mathbf{r}-\mathbf{r}')\cdot\mathbf{e}_1]^2 + [(\mathbf{r}-\mathbf{r}')\cdot\mathbf{e}_2]^2$. One can show that

$$\frac{\partial}{\partial\mathbf{r}}\cdot\frac{\partial}{\partial\mathbf{r}} e^{\pm k\mathbf{r}\cdot\mathbf{e}_3} J_0(k\Delta r) = 0, \tag{C23}$$

so that we can make the ansatz

$$g(\mathbf{r},\mathbf{r}',\omega) = \frac{1}{4\pi\varepsilon_0}\int_0^\infty dk g_k(\mathbf{r},\mathbf{r}',\omega) J_0(k\Delta r) \tag{C24}$$

with the $g_k(\mathbf{r},\mathbf{r}',\omega)$ given in Table IV. Then Eq. (C24) solves the defining differential equation (C6) in all regions of constant $\varepsilon_r(\mathbf{r},\omega)$ and accounts for the boundary condition at infinity and symmetry (C9). The coefficients c_1 to c_{10} appearing in Table IV can be determined by using the continuity at the interface, Eqs. (C8a) and (C8b). Defining

$$\xi_b(\omega) = \frac{\varepsilon_s(\omega)-\varepsilon_b(\omega)}{\varepsilon_s(\omega)+\varepsilon_b(\omega)}, \tag{C25a}$$

$$\xi_v(\omega) = \frac{\varepsilon_s(\omega)-1}{\varepsilon_s(\omega)+1}, \tag{C25b}$$

the coefficients read

$$c_1 = \frac{\xi_b(\omega)e^{-2kd_s}-\xi_v(\omega)}{1-\xi_b(\omega)\xi_v(\omega)e^{-2kd_s}}, \tag{C26a}$$

$$c_2 = \frac{1-\xi_v(\omega)}{1-\xi_b(\omega)\xi_v(\omega)e^{-2kd_s}}, \tag{C26b}$$

$$c_3 = \frac{[1-\xi_v(\omega)]\xi_b(\omega)e^{-2kd_s}}{1-\xi_b(\omega)\xi_v(\omega)e^{-2kd_s}}, \tag{C26c}$$

$$c_4 = \frac{[1-\xi_v(\omega)][1+\xi_b(\omega)]}{1-\xi_b(\omega)\xi_v(\omega)e^{-2kd_s}}, \tag{C26d}$$

$$c_5 = \frac{\xi_v(\omega)\xi_b(\omega)e^{-2kd_s}}{1-\xi_b(\omega)\xi_v(\omega)e^{-2kd_s}}, \tag{C26e}$$

$$c_6 = \frac{\xi_v(\omega)}{1-\xi_b(\omega)\xi_v(\omega)e^{-2kd_s}}, \tag{C26f}$$

$$c_7 = \frac{\xi_b(\omega)e^{-2kd_s}}{1-\xi_b(\omega)\xi_v(\omega)e^{-2kd_s}}, \tag{C26g}$$

$$c_8 = \frac{1+\xi_b(\omega)}{1-\xi_b(\omega)\xi_v(\omega)e^{-2kd_s}}, \tag{C26h}$$

$$c_9 = \frac{[1+\xi_b(\omega)]\xi_v(\omega)}{1-\xi_b(\omega)\xi_v(\omega)e^{-2kd_s}}, \tag{C26i}$$

$$c_{10} = \frac{\xi_v(\omega)-\xi_b(\omega)e^{2kd_s}}{1-\xi_b(\omega)\xi_v(\omega)e^{-2kd_s}}, \tag{C26j}$$

some of which can also be found in Refs. [89,127]. Expanding the denominators in Eqs. (C26) using the geometric series yields an infinite sum of image potentials for the layer configuration.

APPENDIX D: DECOHERENCE DUE TO THOMSON SCATTERING

1. Thomson scattering in the presence of dielectrics

In this section, we calculate decoherence due to the $\mathbf{A}^2$ terms in Hamiltonian (1). We show that these terms can be associated with scattering decoherence due to Thomson scattering, i.e., the radiation due to the acceleration of a charge in an external electromagnetic field. Since the scattering cross section is small for massive particles, this decoherence will turn out to be negligible.

We start by taking the coupling Hamiltonian (1) and the free-field Hamiltonian H_f and only keeping coupling terms that involve the square of the vector potential,

$$H = H_0 + H_f + H_{\text{int}} \tag{D1}$$

with

$$H_{\text{int}} = \frac{1}{2}\int d^3r d^3r' \varrho_0[\mathsf{R}_\Omega^{\mathrm{T}}(\mathbf{r}-\mathbf{R})]\varrho_0[\mathsf{R}_\Omega^{\mathrm{T}}(\mathbf{r}'-\mathbf{R})]\mathbf{A}(\mathbf{r}) \cdot \mathsf{T}(\mathbf{r},\mathbf{r}')\mathbf{A}(\mathbf{r}'). \tag{D2}$$

The free particle Hamiltonian H_0 is given by Eq. (A42) and $\mathbf{A}(\mathbf{r})$ can be found in Eq. (A34). Here, the tensor

$$\mathsf{T}(\mathbf{r},\mathbf{r}') = \frac{1}{m}\mathbb{1} - (\mathbf{r}-\mathbf{R})\times\mathrm{I}_\Omega^{-1}\times(\mathbf{r}'-\mathbf{R}) \tag{D3}$$

depends on the mass and the inertia tensor. The interaction Hamiltonian describes a coupling of the field operators $\mathbf{f}_\lambda(\mathbf{r},\omega)$ due to the presence of the particle.

TABLE IV. The Green function for a geometry consisting of a vacuum half-space with $\varepsilon_r(\mathbf{r},\omega)=1$ for $0<\mathbf{r}\cdot\mathbf{e}_3$, a dielectric layer with $\varepsilon_r(\mathbf{r},\omega)=\varepsilon_s(\omega)$ for $-d_s<\mathbf{r}\cdot\mathbf{e}_3<0$, and a dielectric half-space with $\varepsilon_r(\mathbf{r},\omega)=\varepsilon_b(\omega)$ for $\mathbf{r}\cdot\mathbf{e}_3<-d_s$. For the table, we defined $z=\mathbf{r}\cdot\mathbf{e}_3$ and $z'=\mathbf{r}'\cdot\mathbf{e}_3$. For the dependence of the Green function on $g_k(\mathbf{r},\mathbf{r}',\omega)$, see Eq. (C24).

$g_k(\mathbf{r},\mathbf{r}',\omega)$	$z<-d_s$	$-d_s<z<0$	$0<z$
$z'<-d_s$	$\frac{1}{\varepsilon_b(\omega)}(e^{-k\lvert z-z'\rvert}+c_{10}e^{k(z+z')})$	$\frac{1}{\varepsilon_s(\omega)}(c_8e^{-k(z-z')}+c_9e^{k(z+z')})$	$c_4e^{-k(z-z')}$
$-d_s<z'<0$	$\frac{1}{\varepsilon_s(\omega)}(c_8e^{k(z-z')}+c_9e^{k(z+z')})$	$[e^{-k\lvert z-z'\rvert}+c_5e^{k(z-z')}+c_6e^{k(z+z')}+c_5e^{-k(z-z')}+c_7e^{-k(z+z')}]\frac{1}{\varepsilon_s(\omega)}$	$c_2e^{-k(z-z')}+c_3e^{-k(z+z')}$
$0<z'$	$c_4e^{k(z-z')}$	$c_2e^{k(z-z')}+c_3e^{-k(z+z')}$	$e^{-k\lvert z-z'\rvert}+c_1e^{-k(z+z')}$

As above, we define the bath operator

$$\mathbf{b}(\mathbf{s},t)=\sum_{\lambda=e,m}\int d^3r'\int_0^\infty d\omega\frac{1}{i\omega}\mathsf{G}_\lambda(\mathbf{s},\mathbf{r}',\omega)\mathbf{f}_\lambda(\mathbf{r}',\omega)e^{-i\omega t}+\text{H.c.},\tag{D4}$$

and the tensor-valued particle operator that depends on the particle charge,

$$\mathsf{C}(\mathbf{s},\mathbf{s}',t)=U_0^\dagger(t)\int d^3rd^3r'\varrho_0[\mathsf{R}_\Omega^{\mathrm{T}}(\mathbf{r}-\mathbf{R})]\varrho_0[\mathsf{R}_\Omega^{\mathrm{T}}(\mathbf{r}'-\mathbf{R})]\delta^\perp(\mathbf{r}-\mathbf{s})\mathsf{T}(\mathbf{r},\mathbf{r}')\delta^\perp(\mathbf{r}'-\mathbf{s}')U_0(t).\tag{D5}$$

Here, the transverse delta function, given by Eq. (A39), arises from the transverse part of the Green tensor included in the vector potential.

The interaction Hamiltonian in the interaction picture reads

$$\tilde{H}_{\mathrm{int}}(t)=\frac{1}{2}\int d^3sd^3s'\mathbf{b}(\mathbf{s},t)\cdot\mathsf{C}(\mathbf{s},\mathbf{s}',t)\mathbf{b}(\mathbf{s}',t).\tag{D6}$$

In the weak coupling limit, one has to evaluate

$$\begin{aligned}\int_0^\infty d\tau\,\mathrm{tr}_B\{[\tilde{H}_{\mathrm{int}}(t),[\tilde{H}_{\mathrm{int}}(t-\tau),\tilde{\rho}(t)\otimes\rho_B]]\}&=\frac{1}{4}\int d^3s_1d^3s_1'd^3s_2d^3s_2'\sum_{i_1i_1'i_2i_2'}\int_0^\infty d\tau\\&\times\Big(-\frac{i}{2}[C_{i_1i_1'}(\mathbf{s}_1,\mathbf{s}_1',t),\{D_{i_1i_1'i_2i_2'}(\mathbf{s}_1,\mathbf{s}_1',\mathbf{s}_2,\mathbf{s}_2',\tau)C_{i_2i_2'}(\mathbf{s}_2,\mathbf{s}_2',t-\tau),\tilde{\rho}(t)\}]\\&+\frac{1}{2}[C_{i_1i_1'}(\mathbf{s}_1,\mathbf{s}_1',t),[N_{i_1i_1'i_2i_2'}(\mathbf{s}_1,\mathbf{s}_1',\mathbf{s}_2,\mathbf{s}_2',\tau)C_{i_2i_2'}(\mathbf{s}_2,\mathbf{s}_2',t-\tau),\tilde{\rho}(t)]]\Big),\end{aligned}\tag{D7}$$

involving the dissipation kernel [101]

$$\begin{aligned}D_{i_1i_1'i_2i_2'}(\mathbf{s}_1,\mathbf{s}_1',\mathbf{s}_2,\mathbf{s}_2',\tau)&=i\langle b_{i_1}(\mathbf{s}_1,t)b_{i_1'}(\mathbf{s}_1',t)b_{i_2}(\mathbf{s}_2,t-\tau)b_{i_2'}(\mathbf{s}_2',t-\tau)\\&\quad-b_{i_2}(\mathbf{s}_2,t-\tau)b_{i_2'}(\mathbf{s}_2',t-\tau)b_{i_1}(\mathbf{s}_1,t)b_{i_1'}(\mathbf{s}_1',t)\rangle_B\end{aligned}\tag{D8}$$

and the noise kernel

$$\begin{aligned}N_{i_1i_1'i_2i_2'}(\mathbf{s}_1,\mathbf{s}_1',\mathbf{s}_2,\mathbf{s}_2',\tau)&=\langle b_{i_1}(\mathbf{s}_1,t)b_{i_1'}(\mathbf{s}_1',t)b_{i_2}(\mathbf{s}_2,t-\tau)b_{i_2'}(\mathbf{s}_2',t-\tau)\\&\quad+b_{i_2}(\mathbf{s}_2,t-\tau)b_{i_2'}(\mathbf{s}_2',t-\tau)b_{i_1}(\mathbf{s}_1,t)b_{i_1'}(\mathbf{s}_1',t)\rangle_B.\end{aligned}\tag{D9}$$

Here, $\langle\cdot\rangle_B=\mathrm{tr}_B\{\cdot\rho_B\}$ is the expectation value of bath operators. The indices refer to the components of the vectors $\mathbf{b}(\mathbf{s},t)$ and tensors $\mathsf{C}(\mathbf{s},\mathbf{s}',t)$.

In order to calculate the decoherence rate, one has to determine the dissipator $\mathcal{L}_{\mathrm{Th}}$ from the double commutator in Eq. (D7). In the slow-particle limit

$$C_{i_2 i_2'}(\mathbf{s}_2, \mathbf{s}_2', t-\tau) \approx C_{i_2 i_2'}(\mathbf{s}_2, \mathbf{s}_2', t), \tag{D10}$$

and after transforming back to the Schrödinger picture we find that

$$\mathcal{L}_{\mathrm{Th}}\rho = -\frac{1}{8\hbar^2}\int d^3s_1 d^3s_1' d^3s_2 d^3s_2' \times \sum_{i_1 i_1' i_2 i_2'} \left[C_{i_1 i_1'}(\mathbf{s}_1, \mathbf{s}_1'), \left[\int_0^\infty d\tau N_{i_1 i_1' i_2 i_2'}(\mathbf{s}_1, \mathbf{s}_1', \mathbf{s}_2, \mathbf{s}_2', \tau) C_{i_2 i_2'}(\mathbf{s}_2, \mathbf{s}_2'), \rho\right]\right], \tag{D11}$$

where $C_{i_1 i_1'}(\mathbf{s}, \mathbf{s}') := C_{i_1 i_1'}(\mathbf{s}, \mathbf{s}', 0)$. The Born-Markov approximation assumed here is justified if the particle operator $\mathsf{C}(\mathbf{s}, \mathbf{s}', t)$ evolves slowly in comparison to the timescale on which the dissipation kernel decays.

To calculate the noise kernel, we first evaluate the fourth-order thermal oscillator correlation function. Correlation functions involving unequal numbers of daggered and undaggered operators vanish. As the only nontrivial correlation function, we find that

$$\begin{aligned}
&\langle [\mathbf{f}_{\lambda_1}^\dagger(\mathbf{r}_1, \omega_1)]_{j_1} [\mathbf{f}_{\lambda_1'}^\dagger(\mathbf{r}_1', \omega_1')]_{j_1'} [\mathbf{f}_{\lambda_2}(\mathbf{r}_2, \omega_2)]_{j_2} [\mathbf{f}_{\lambda_2'}(\mathbf{r}_2', \omega_2')]_{j_2'} \rangle \\
&= n(\omega_1) n(\omega_1') \Big[\delta(\mathbf{r}_1 - \mathbf{r}_2)\delta(\mathbf{r}_1' - \mathbf{r}_2')\delta(\omega_1 - \omega_2)\delta(\omega_1' - \omega_2')\delta_{\lambda_1\lambda_2}\delta_{\lambda_1'\lambda_2'}\delta_{j_1 j_2}\delta_{j_1' j_2'} \\
&+ \delta(\mathbf{r}_1 - \mathbf{r}_2')\delta(\mathbf{r}_1' - \mathbf{r}_2)\delta(\omega_1 - \omega_2')\delta(\omega_1' - \omega_2)\delta_{\lambda_1\lambda_2'}\delta_{\lambda_1'\lambda_2}\delta_{j_1 j_2'}\delta_{j_1' j_2}\Big],
\end{aligned} \tag{D12}$$

while all other correlation functions follow from the commutation relations; see above Eq. (A33).

A tedious but straightforward calculation yields

$$\begin{aligned}
N_{i_1 i_1' i_2 i_2'}(\mathbf{s}_1, \mathbf{s}_1', \mathbf{s}_2, \mathbf{s}_2', \tau) &= 2\hbar^2 \int_0^\infty d\omega_1 d\omega_1' \frac{1}{\omega_1^2 \omega_1'^2} J_{i_1' i_1}(\mathbf{s}_1', \mathbf{s}_1, \omega_1) J_{i_2' i_2}(\mathbf{s}_2', \mathbf{s}_2, \omega_1')[2n(\omega_1) + 1][2n(\omega_1') + 1] \\
&+ \hbar^2 \int_0^\infty d\omega_1 d\omega_1' \frac{1}{\omega_1^2 \omega_1'^2} [J_{i_2 i_1}(\mathbf{s}_2, \mathbf{s}_1, \omega_1) J_{i_2' i_1'}(\mathbf{s}_2', \mathbf{s}_1', \omega_1') + J_{i_2' i_1}(\mathbf{s}_2', \mathbf{s}_1, \omega_1) J_{i_2 i_1'}(\mathbf{s}_2, \mathbf{s}_1', \omega_1')] \\
&\times \{[2n(\omega_1) + 2n(\omega_1') + 4n(\omega_1) n(\omega_1')] \cos[(\omega_1 - \omega_1')\tau] \\
&+ [2n(\omega_1) + 2n(\omega_1') + 4n(\omega_1) n(\omega_1') + 2] \cos[(\omega_1 + \omega_1')\tau]\},
\end{aligned} \tag{D13}$$

using relation (B9) and the definition of the spectral density (B8) and its components $J_{ii'}(\mathbf{s}, \mathbf{s}', \omega)$.

The first term in Eq. (D13) is independent of time and arises from those contributions $[\mathbf{f}_\lambda^\dagger(\mathbf{r}, \omega)]_j [\mathbf{f}_\lambda(\mathbf{r}, \omega)]_j$ and $[\mathbf{f}_\lambda(\mathbf{r}, \omega)]_j [\mathbf{f}_\lambda^\dagger(\mathbf{r}, \omega)]_j$ in the interaction Hamiltonian (D2) that are equal in all indices and arguments. To avoid the time integral in the slow-particle limit from diverging, we drop the time-independent terms in Eq. (D13). This procedure does not affect the particle-induced coupling in Eq. (D2) of field degrees of freedom $\mathbf{f}_\lambda(\mathbf{r}, \omega)$ with different indices and arguments. It is justified by the fact that in vacuum the resulting master equation coincides with the scattering master equation [128] obtained by means of the Thompson scattering amplitudes; see Eq. (D28).

The integral of the noise kernel without the time-independent contribution yields

$$\begin{aligned}
&\int_0^\infty d\tau N_{i_1 i_1' i_2 i_2'}(\mathbf{s}_1, \mathbf{s}_1', \mathbf{s}_2, \mathbf{s}_2', \tau) \\
&= \int_0^\infty d\omega \frac{4\pi\hbar^2}{\omega^4} [J_{i_2 i_1}(\mathbf{s}_2, \mathbf{s}_1, \omega) J_{i_2' i_1'}(\mathbf{s}_2', \mathbf{s}_1', \omega) + J_{i_2' i_1}(\mathbf{s}_2', \mathbf{s}_1, \omega) J_{i_2 i_1'}(\mathbf{s}_2, \mathbf{s}_1', \omega)] n(\omega)[n(\omega) + 1].
\end{aligned} \tag{D14}$$

Inserting Eq. (D14) into Eq. (D11), using

$$\mathsf{C}(\mathbf{s}, \mathbf{s}') = \int d^3r d^3r' \varrho_0[\mathsf{R}_\Omega^{\mathrm{T}}(\mathbf{r} - \mathbf{R})] \varrho_0[\mathsf{R}_\Omega^{\mathrm{T}}(\mathbf{r}' - \mathbf{R})] \delta^\perp(\mathbf{r} - \mathbf{s}) \mathsf{T}(\mathbf{r}, \mathbf{r}') \delta^\perp(\mathbf{r}' - \mathbf{s}'), \tag{D15}$$

and the symmetries $\mathsf{J}^{\mathrm{T}}(\mathbf{s},\mathbf{s}',\omega)=\mathsf{J}(\mathbf{s}',\mathbf{s},\omega)$, $\mathsf{C}^{\mathrm{T}}(\mathbf{s},\mathbf{s}')=\mathsf{C}(\mathbf{s}',\mathbf{s})$, one arrives at

$$\mathcal{L}_{\mathrm{Th}}\rho=\int_0^\infty d\omega\frac{2\pi}{\omega^4}n(\omega)[n(\omega)+1]\int d^3s_1d^3s_2\ \mathrm{Tr}\left[\mathsf{L}(\mathbf{s}_1,\mathbf{s}_2,\omega)\rho\mathsf{L}(\mathbf{s}_2,\mathbf{s}_1,\omega)-\frac{1}{2}\{\mathsf{L}(\mathbf{s}_1,\mathbf{s}_2,\omega)\mathsf{L}(\mathbf{s}_2,\mathbf{s}_1,\omega),\rho\}\right] \tag{D16}$$

with

$$\mathsf{L}(\mathbf{s}_1,\mathbf{s}_2,\omega)=\int d^3s\mathsf{J}(\mathbf{s}_1,\mathbf{s},\omega)\mathsf{C}(\mathbf{s},\mathbf{s}_2). \tag{D17}$$

Here $\mathrm{Tr}[\cdot]$ is the tensor trace. The dissipator $\mathcal{L}_{\mathrm{Th}}$ describes decoherence of a particle with arbitrary charge distribution near a dielectric medium due to the $\mathbf{A}^2$ term in the coupling Hamiltonian. The properties of the dielectric enter through the spectral density $\mathsf{J}(\mathbf{s},\mathbf{s}',\omega)$, while the particle properties enter through the operator $\mathsf{C}(\mathbf{s},\mathbf{s}')$.

2. Free-space Thomson scattering

We are now in a position to describe decoherence due to free-space Thompson scattering by inserting into Eq. (D16) the free-space Green tensor

$$\mathsf{G}(\mathbf{r},\mathbf{r}',\omega)=\frac{c^2}{(2\pi)^3}\lim_{\epsilon\downarrow 0}\int d^3k\left(\mathbb{1}-\frac{c\mathbf{k}}{\omega+i\epsilon}\otimes\frac{c\mathbf{k}}{\omega+i\epsilon}\right)\frac{e^{i\mathbf{k}\cdot(\mathbf{r}-\mathbf{r}')}}{c^2k^2-(\omega+i\epsilon)^2}. \tag{D18}$$

Carrying out a cyclic permutation inside the trace, we obtain

$$\begin{aligned}&\int d^3s_1d^3s_2\ \mathrm{Tr}[\mathsf{L}(\mathbf{s}_1,\mathbf{s}_2,\omega)\,\rho\,\mathsf{L}(\mathbf{s}_2,\mathbf{s}_1,\omega)]\\&=\int d^3r_1d^3r_1'd^3r_2d^3r_2'\varrho_0[\mathsf{R}_\Omega^{\mathrm{T}}(\mathbf{r}_1-\mathbf{R})]\varrho_0[\mathsf{R}_\Omega^{\mathrm{T}}(\mathbf{r}_1'-\mathbf{R})]\\&\times\mathrm{Tr}[{}^{\perp}\mathsf{J}^{\perp}(\mathbf{r}_2',\mathbf{r}_1,\omega)\mathsf{T}(\mathbf{r}_1,\mathbf{r}_1')\rho{}^{\perp}\mathsf{J}^{\perp}(\mathbf{r}_1',\mathbf{r}_2,\omega)\mathsf{T}(\mathbf{r}_2,\mathbf{r}_2')]\varrho_0[\mathsf{R}_\Omega^{\mathrm{T}}(\mathbf{r}_2-\mathbf{R})]\varrho_0[\mathsf{R}_\Omega^{\mathrm{T}}(\mathbf{r}_2'-\mathbf{R})].\end{aligned} \tag{D19}$$

Here, ${}^{\perp}\mathsf{J}^{\perp}(\mathbf{r},\mathbf{r}',\omega)\equiv\mu_0\omega^2\,\mathrm{Im}{}^{\perp}\mathsf{G}^{\perp}(\mathbf{r},\mathbf{r}',\omega)/\pi$ is the left-and-right transverse of the spectral density (B8). It can be obtained from

$$\begin{aligned}{}^{\perp}\mathsf{G}^{\perp}(\mathbf{r},\mathbf{r}',\omega)&\equiv\int d^3sd^3s'\delta^{\perp}(\mathbf{r}-\mathbf{s})\mathsf{G}(\mathbf{s},\mathbf{s}',\omega)\delta^{\perp}(\mathbf{r}'-\mathbf{s}')\\&=-\lim_{\epsilon\downarrow 0}\frac{c^2}{(2\pi)^3}\int d^3k\frac{e^{i\mathbf{k}\cdot(\mathbf{r}-\mathbf{r}')}}{c^2k^2-(\omega+i\epsilon)^2}\frac{\mathbf{k}}{k}\times\left(\frac{\mathbf{k}}{k}\times\mathbb{1}\right),\end{aligned} \tag{D20}$$

where we have used Eq. (D18) with the Fourier-representation of the transverse δ distribution (A39),

$$\delta^{\perp}(\mathbf{r}-\mathbf{r}')=-\frac{1}{(2\pi)^3}\int d^3k\frac{\mathbf{k}}{k}\times\left(\frac{\mathbf{k}}{k}\times\mathbb{1}\right)e^{i\mathbf{k}\cdot(\mathbf{r}-\mathbf{r}')}. \tag{D21}$$

Noting that

$$\lim_{\epsilon\downarrow 0}\left(\frac{c^2k^2}{c^2k^2-(\omega+i\epsilon)^2}-\frac{c^2k^2}{c^2k^2-(\omega-i\epsilon)^2}\right)=\frac{i\pi\omega}{c}\delta\left(k-\frac{\omega}{c}\right) \tag{D22}$$

and $d^3k=dkk^2d^2n$ with $\mathbf{k}=k\mathbf{n}$, this yields

$${}^{\perp}\mathsf{J}^{\perp}(\mathbf{r},\mathbf{r}',\omega)=-\frac{\mu_0\omega^3}{2c(2\pi)^3}\int d^2n\mathbf{n}\times(\mathbf{n}\times\mathbb{1})e^{i(\omega/c)\mathbf{n}\cdot(\mathbf{r}-\mathbf{r}')}. \tag{D23}$$

Next, one inserts Eq. (D23) into Eq. (D19), defines the orientation-dependent form-factor operators

$$F(\mathbf{k}) = \int d^3r \varrho_0(\mathbf{r}) e^{i\mathbf{k}\cdot\mathsf{R}_\Omega\mathbf{r}} = F^\dagger(-\mathbf{k}), \tag{D24a}$$

$$\mathbf{F}(\mathbf{k}) = \int d^3r \varrho_0(\mathbf{r}) e^{i\mathbf{k}\cdot\mathsf{R}_\Omega\mathbf{r}} \mathsf{R}_\Omega\mathbf{r} = \mathbf{F}^\dagger(-\mathbf{k}), \tag{D24b}$$

and uses the facts that

$$\mathbf{n}\times(\mathbf{n}\times\mathbb{1}) = \mathbf{n}\otimes\mathbf{n} - \mathbb{1} = -[\mathbf{n}\otimes\mathbf{n} - \mathbb{1}][\mathbf{n}\otimes\mathbf{n} - \mathbb{1}], \tag{D25}$$

$$\mathbf{n}'\times(\mathbf{n}'\times\mathbb{1}) = -\sum_{j=1}^{2} \boldsymbol{\epsilon}_j'\otimes\boldsymbol{\epsilon}_j', \tag{D26}$$

with $\boldsymbol{\epsilon}_1'$, $\boldsymbol{\epsilon}_2'$ forming an orthonormal basis with $\mathbf{n}'$ (like the two polarization vectors of a plane wave traveling in direction $\mathbf{n}'$). With these definitions and Eq. (D3) one can write

$$\begin{aligned}\int d^3s_1 d^3s_2\ \mathrm{Tr}[\mathsf{L}(\mathbf{s}_1,\mathbf{s}_2,\omega)\rho\mathsf{L}(\mathbf{s}_2,\mathbf{s}_1,\omega)] = \left(\frac{\mu_0\omega^3}{2c(2\pi)^3}\right)^2 \int d^2n d^2n' \sum_{j=1}^{2} \mathrm{Tr}\Bigg\{[\mathbf{n}\otimes\mathbf{n}-\mathbb{1}]\Bigg[\mathbb{1}\frac{F(-\omega\mathbf{n}/c)F(\omega\mathbf{n}'/c)}{m}\\ - \mathbf{F}(-\omega\mathbf{n}/c)\times\mathrm{I}_\Omega^{-1}\times\mathbf{F}(\omega\mathbf{n}'/c)\Bigg]\boldsymbol{\epsilon}_j'\otimes\boldsymbol{\epsilon}_j' e^{i(\omega/c)(\mathbf{n}'-\mathbf{n})\cdot\mathbf{R}}\rho e^{-i(\omega/c)(\mathbf{n}'-\mathbf{n})\cdot\mathbf{R}}\Bigg[\mathbb{1}\frac{F^\dagger(\omega\mathbf{n}'/c)F^\dagger(-\omega\mathbf{n}/c)}{m}\\ - \mathbf{F}^\dagger(\omega\mathbf{n}'/c)\times\mathrm{I}_\Omega^{-1}\times\mathbf{F}^\dagger(-\omega\mathbf{n}/c)\Bigg][\mathbf{n}\otimes\mathbf{n}-\mathbb{1}]\Bigg\}.\end{aligned} \tag{D27}$$

Here, one can identify the orientation-dependent scatting amplitude of Thomson scattering

$$\mathbf{F}_j(\mathbf{k},\mathbf{k}') = \frac{1}{4\pi\epsilon_0 c^2}\left[\frac{\mathbf{k}}{k}\otimes\frac{\mathbf{k}}{k} - \mathbb{1}\right]\left[\mathbb{1}\frac{F(-\mathbf{k})F(\mathbf{k}')}{m} - \mathbf{F}(-\mathbf{k})\times\mathrm{I}_\Omega^{-1}\times\mathbf{F}(\mathbf{k}')\right]\boldsymbol{\epsilon}_j' \tag{D28}$$

of an electromagnetic wave with incoming wave vector $\mathbf{k}'$ and polarization $\boldsymbol{\epsilon}_j'$, elastically scattered at a rigid charge distribution to an outgoing direction with wave vector $\mathbf{k}$, as can be derived from classical electrodynamics [129]. With this, Eq. (D27) can be simplified to

$$\begin{aligned}&\int d^3s_1 d^3s_2\ \mathrm{Tr}[\mathsf{L}(\mathbf{s}_1,\mathbf{s}_2,\omega)\rho\mathsf{L}(\mathbf{s}_2,\mathbf{s}_1,\omega)]\\ &= \left(\frac{\omega^3}{c(2\pi)^2}\right)^2 \int d^2n d^2n' \sum_{j=1}^{2} \mathrm{Tr}\left\{\mathbf{F}_j\left(\frac{\omega}{c}\mathbf{n},\frac{\omega}{c}\mathbf{n}'\right)e^{i(\omega/c)(\mathbf{n}'-\mathbf{n})\cdot\mathbf{R}}\rho\otimes\mathbf{F}_j^\dagger\left(\frac{\omega}{c}\mathbf{n},\frac{\omega}{c}\mathbf{n}'\right)e^{-i(\omega/c)(\mathbf{n}'-\mathbf{n})\cdot\mathbf{R}}\right\}\\ &= \left(\frac{\omega^3}{c(2\pi)^2}\right)^2 \int d^2n d^2n' \sum_{j=1}^{2} \mathbf{F}_j\left(\frac{\omega}{c}\mathbf{n},\frac{\omega}{c}\mathbf{n}'\right)e^{i(\omega/c)(\mathbf{n}'-\mathbf{n})\cdot\mathbf{R}}\rho\cdot\mathbf{F}_j^\dagger\left(\frac{\omega}{c}\mathbf{n},\frac{\omega}{c}\mathbf{n}'\right)e^{-i(\omega/c)(\mathbf{n}'-\mathbf{n})\cdot\mathbf{R}}.\end{aligned} \tag{D29}$$

Defining the Lindblad operators

$$\mathbf{L}_j(\mathbf{k},\mathbf{k}') = e^{i(\mathbf{k}'-\mathbf{k})\cdot\mathbf{R}}\mathbf{F}_j(\mathbf{k},\mathbf{k}') \tag{D30}$$

with symmetry $\mathbf{L}_j(\mathbf{k},\mathbf{k}') = \mathbf{L}_j^\dagger(-\mathbf{k},-\mathbf{k}')$, we can write the total dissipator (D16) as

$$\mathcal{L}_{\rm Th}\rho = \int_0^\infty dk \frac{ck^2}{(2\pi)^3} n(ck)[n(ck)+1] \times \int d^2n d^2n' \sum_{j=1}^{2} \left[\mathbf{L}_j(k\mathbf{n}, k\mathbf{n}') \cdot \rho \mathbf{L}_j^\dagger(k\mathbf{n}, k\mathbf{n}') - \frac{1}{2}\{\mathbf{L}_j^\dagger(k\mathbf{n}, k\mathbf{n}') \cdot \mathbf{L}_j(k\mathbf{n}, k\mathbf{n}'), \rho\} \right]. \tag{D31}$$

The dissipator (D31) is of the typical form to describe scattering decoherence. The Lindblad operators are given by plane waves multiplied by the scattering amplitude, while the prefactor accounts for the statistics of the scattering incidents. The dissipator is consistent with the dissipator derived in the monitoring approach [128,130].

3. Thomson-scattering decoherence of a point monopole

To estimate decoherence of a point monopole $\varrho_0(\mathbf{r}) = q\delta(\mathbf{r})$, we use the fact that the transverse electromagnetic field, and thus the vector potential, dominates the particle-surface interaction for distances larger than the wavelength, e.g., the thermal wavelength $2\pi\hbar c/k_B T$. For simplicity, we thus assume the particle to be located in free space, where Eq. (D31) applies. For the point particle, the scattering amplitude (D28) reduces to

$$\mathbf{F}_j(k\mathbf{n}, k\mathbf{n}') = \frac{q^2}{4\pi\epsilon_0 c^2 m}[\mathbf{n}\otimes\mathbf{n} - \mathbb{1}]\boldsymbol{\epsilon}_j', \tag{D32}$$

which fulfills

$$\sum_{j=1}^{2} \mathbf{F}_j(k\mathbf{n}, k\mathbf{n}') \cdot \mathbf{F}_j^\dagger(k\mathbf{n}, k\mathbf{n}') = \left(\frac{q^2}{4\pi\epsilon_0 c^2 m}\right)^2 [1 + (\mathbf{n}\cdot\mathbf{n}')^2]. \tag{D33}$$

Thus, the coherences in the position basis decrease according to $\langle\mathbf{R}|\,\mathcal{L}_{\rm Th}\rho\,|\mathbf{R}'\rangle = -\Gamma_{\rm Th}(\mathbf{R},\mathbf{R}')\,\langle\mathbf{R}|\,\rho\,|\mathbf{R}'\rangle$ with decoherence rate

$$\Gamma_{\rm Th}(\mathbf{R},\mathbf{R}') = \left(\frac{q^2}{4\pi\epsilon_0 c^2 m}\right)^2 \int_0^\infty dk \frac{ck^2}{(2\pi)^3} n(ck)[n(ck)+1] \times \int d^2n d^2n' [1 + (\mathbf{n}\cdot\mathbf{n}')^2](1 - e^{ik(\mathbf{n}'-\mathbf{n})\cdot(\mathbf{R}-\mathbf{R}')}). \tag{D34}$$

We express the spherical integrals through the spherical Bessel functions of the first kind $j_n(x)$,

$$\Gamma_{\rm Th}(\mathbf{R},\mathbf{R}') = \left(\frac{q^2}{4\pi\epsilon_0 c^2 m}\right)^2 \int_0^\infty dk \frac{2ck^2}{\pi} n(ck)[n(ck)+1] \times \left\{\frac{4}{3} - 2\left[\left(j_0(x) - \frac{j_1(x)}{x}\right)^2 + 2\frac{j_1^2(x)}{x^2}\right]\right\}, \tag{D35}$$

where $x = k|\mathbf{R}-\mathbf{R}'|$. The rate vanishes for $|\mathbf{R}-\mathbf{R}'| = 0$, while for separations $|\mathbf{R}-\mathbf{R}'|$ much larger than the thermal wavelength, it saturates at the value

$$\Gamma_\infty = \left(\frac{q^2}{4\pi\epsilon_0 c^3 m}\right)^2 \frac{8\pi}{9}\left(\frac{k_B T}{\hbar}\right)^3. \tag{D36}$$

The impact of decoherence due to the $\mathbf{A}^2$ term can now be evaluated explicitly. For example, a single electron in vacuum at temperature $T = 300$ K is subject to a decoherence rate of

$$\Gamma_\infty \approx 1.5 \times 10^{-5}\ \mathrm{s}^{-1},$$

which is negligible in comparison to the decoherence due to the longitudinal field. This is a consequence of the tiny scattering cross section of Thomson scattering, which is even smaller for nanoparticles with their reduced ratio of q^2/m.

[1] C. Monroe, W. C. Campbell, L.-M. Duan, Z.-X. Gong, A. V. Gorshkov, P. W. Hess, R. Islam, K. Kim, N. M. Linke, G. Pagano, P. Richerme, C. Senko, and N. Y. Yao, Programmable quantum simulations of spin systems with trapped ions, Rev. Mod. Phys. **93**, 025001 (2021).

[2] N. P. de Leon, K. M. Itoh, D. Kim, K. K. Mehta, T. E. Northup, H. Paik, B. Palmer, N. Samarth, S. Sangtawesin, and D. Steuerman, Materials challenges and opportunities for quantum computing hardware, Science **372**, eabb2823 (2021).

[3] K. A. Gilmore, M. Affolter, R. J. Lewis-Swan, D. Barberena, E. Jordan, A. M. Rey, and J. J. Bollinger, Quantum-enhanced sensing of displacements and electric fields with two-dimensional trapped-ion crystals, Science **373**, 673 (2021).

[4] M. Cetina, L. Egan, C. Noel, M. Goldman, D. Biswas, A. Risinger, D. Zhu, and C. Monroe, Quantum Gates on Individually Addressed Atomic Qubits Subject to Noisy Transverse Motion, PRX Quantum **3**, 010334 (2022).

[5] J. Zhang, P. Hess, A. Kyprianidis, P. Becker, A. Lee, J. Smith, G. Pagano, I.-D. Potirniche, A. C. Potter, A. Vishwanath, *et al.*, Observation of a discrete time crystal, Nature **543**, 217 (2017).

[6] A. Kyprianidis, F. Machado, W. Morong, P. Becker, K. S. Collins, D. V. Else, L. Feng, P. W. Hess, C. Nayak, G. Pagano, *et al.*, Observation of a prethermal discrete time crystal, Science **372**, 1192 (2021).

[7] A. André, D. DeMille, J. M. Doyle, M. D. Lukin, S. E. Maxwell, P. Rabl, R. J. Schoelkopf, and P. Zoller, A coherent all-electrical interface between polar molecules and mesoscopic superconducting resonators, Nat. Phys. **2**, 636 (2006).

[8] P. Rabl, D. DeMille, J. M. Doyle, M. D. Lukin, R. Schoelkopf, and P. Zoller, Hybrid Quantum Processors: Molecular Ensembles as Quantum Memory for Solid State Circuits, Phys. Rev. Lett. **97**, 033003 (2006).

[9] P. Rabl and P. Zoller, Molecular dipolar crystals as high-fidelity quantum memory for hybrid quantum computing, Phys. Rev. A **76**, 042308 (2007).

[10] Z.-L. Xiang, S. Ashhab, J. You, and F. Nori, Hybrid quantum circuits: Superconducting circuits interacting with other quantum systems, Rev. Mod. Phys. **85**, 623 (2013).

[11] V. V. Albert, J. P. Covey, and J. Preskill, Robust encoding of a qubit in a molecule, Phys. Rev. X **10**, 031050 (2020).

[12] R. Sawant, J. A. Blackmore, P. D. Gregory, J. Mur-Petit, D. Jaksch, J. Aldegunde, J. M. Hutson, M. Tarbutt, and S. L. Cornish, Ultracold polar molecules as qudits, New J. Phys. **22**, 013027 (2020).

[13] W. C. Campbell and E. R. Hudson, Dipole-Phonon Quantum Logic with Trapped Polar Molecular Ions, Phys. Rev. Lett. **125**, 120501 (2020).

[14] P. D. Gregory, J. A. Blackmore, S. L. Bromley, J. M. Hutson, and S. L. Cornish, Robust storage qubits in ultracold polar molecules, Nat. Phys. **17**, 1149 (2021).

[15] R. V. Krems, Cold controlled chemistry, Phys. Chem. Chem. Phys. **10**, 4079 (2008).

[16] S. Ospelkaus, K.-K. Ni, D. Wang, M. De Miranda, B. Neyenhuis, G. Quéméner, P. Julienne, J. Bohn, D. Jin, and J. Ye, Quantum-state controlled chemical reactions of ultracold potassium-rubidium molecules, Science **327**, 853 (2010).

[17] G. Quemener and P. S. Julienne, Ultracold molecules under control!, Chem. Rev. **112**, 4949 (2012).

[18] N. Balakrishnan, Perspective: Ultracold molecules and the dawn of cold controlled chemistry, J. Chem. Phys. **145**, 150901 (2016).

[19] M.-G. Hu, Y. Liu, M. A. Nichols, L. Zhu, G. Quéméner, O. Dulieu, and K.-K. Ni, Nuclear spin conservation enables state-to-state control of ultracold molecular reactions, Nat. Chem. **13**, 435 (2021).

[20] H. Hirzler, R. Lous, E. Trimby, J. Pérez-Ríos, A. Safavi-Naini, and R. Gerritsma, Observation of Chemical Reactions between a Trapped Ion and Ultracold Feshbach Dimers, Phys. Rev. Lett. **128**, 103401 (2022).

[21] T. Zelevinsky, S. Kotochigova, and J. Ye, Precision Test of Mass-Ratio Variations with Lattice-Confined Ultracold Molecules, Phys. Rev. Lett. **100**, 043201 (2008).

[22] J. J. Hudson, D. M. Kara, I. Smallman, B. E. Sauer, M. R. Tarbutt, and E. A. Hinds, Improved measurement of the shape of the electron, Nature **473**, 493 (2011).

[23] D. DeMille, J. M. Doyle, and A. O. Sushkov, Probing the frontiers of particle physics with tabletop-scale experiments, Science **357**, 990 (2017).

[24] M. Safronova, D. Budker, D. DeMille, D. F. J. Kimball, A. Derevianko, and C. W. Clark, Search for new physics with atoms and molecules, Rev. Mod. Phys. **90**, 025008 (2018).

[25] E. Urban, N. Glikin, S. Mouradian, K. Krimmel, B. Hemmerling, and H. Haeffner, Coherent Control of the Rotational Degree of Freedom of a Two-Ion Coulomb Crystal, Phys. Rev. Lett. **123**, 133202 (2019).

[26] D. Budker, P. W. Graham, H. Ramani, F. Schmidt-Kaler, C. Smorra, and S. Ulmer, Millicharged Dark Matter Detection with Ion Traps, PRX Quantum **3**, 010330 (2022).

[27] C. Gonzalez-Ballestero, M. Aspelmeyer, L. Novotny, R. Quidant, and O. Romero-Isart, Levitodynamics: Levitation and control of microscopic objects in vacuum, Science **374**, eabg3027 (2021).

[28] M. Perdriat, C. Pellet-Mary, P. Huillery, L. Rondin, and G. Hétet, Spin-mechanics with nitrogen-vacancy centers and trapped particles, Micromachines **12**, 651 (2021).

[29] D. Goldwater, B. A. Stickler, L. Martinetz, T. E. Northup, K. Hornberger, and J. Millen, Levitated electromechanics: All-electrical cooling of charged nano-and microparticles, Quantum Sci. Technol. **4**, 024003 (2019).

[30] L. Magrini, P. Rosenzweig, C. Bach, A. Deutschmann-Olek, S. G. Hofer, S. Hong, N. Kiesel, A. Kugi, and M. Aspelmeyer, Optimal quantum control of mechanical motion at room temperature: Ground-state cooling, Nature **595**, 373 (2021).

[31] F. Tebbenjohanns, M. L. Mattana, M. Rossi, M. Frimmer, and L. Novotny, Quantum control of a nanoparticle optically levitated in cryogenic free space, Nature **595**, 378 (2021).

[32] M. Arndt and K. Hornberger, Testing the limits of quantum mechanical superpositions, Nat. Phys. **10**, 271 (2014).

[33] J. Millen and B. A. Stickler, Quantum experiments with microscale particles, Contemp. Phys. **61**, 155 (2020).

[34] L. Martinetz, K. Hornberger, J. Millen, M. Kim, and B. A. Stickler, Quantum electromechanics with levitated nanoparticles, npj Quantum Inf. **6**, 101 (2020).

[35] D. Carney, H. Häffner, D. C. Moore, and J. M. Taylor, Trapped Electrons and Ions as Particle Detectors, Phys. Rev. Lett. **127**, 061804 (2021).

[36] M. Lemeshko, R. V. Krems, J. M. Doyle, and S. Kais, Manipulation of molecules with electromagnetic fields, Mol. Phys. **111**, 1648 (2013).

[37] C. P. Koch, M. Lemeshko, and D. Sugny, Quantum control of molecular rotation, Rev. Mod. Phys. **91**, 035005 (2019).

[38] B. A. Stickler, K. Hornberger, and M. Kim, Quantum rotations of nanoparticles, Nat. Rev. Phys. **3**, 589 (2021).

[39] D. DeMille, Quantum Computation with Trapped Polar Molecules, Phys. Rev. Lett. **88**, 067901 (2002).

[40] E. R. Hudson and W. C. Campbell, Dipolar quantum logic for freely rotating trapped molecular ions, Phys. Rev. A **98**, 040302 (2018).

[41] T. M. Hoang, Y. Ma, J. Ahn, J. Bang, F. Robicheaux, Z.-Q. Yin, and T. Li, Torsional Optomechanics of a Levitated Nonspherical Nanoparticle, Phys. Rev. Lett. **117**, 123604 (2016).

[42] S. Kuhn, A. Kosloff, B. A. Stickler, F. Patolsky, K. Hornberger, M. Arndt, and J. Millen, Full rotational control of levitated silicon nanorods, Optica **4**, 356 (2017).

[43] S. Kuhn, B. A. Stickler, A. Kosloff, F. Patolsky, K. Hornberger, M. Arndt, and J. Millen, Optically driven

ultra-stable nanomechanical rotor, Nat. Commun. **8**, 1670 (2017).
[44] M. Rashid, M. Toroš, A. Setter, and H. Ulbricht, Precession Motion in Levitated Optomechanics, Phys. Rev. Lett. **121**, 253601 (2018).
[45] R. Reimann, M. Doderer, E. Hebestreit, R. Diehl, M. Frimmer, D. Windey, F. Tebbenjohanns, and L. Novotny, GHz Rotation of an Optically Trapped Nanoparticle in Vacuum, Phys. Rev. Lett. **121**, 033602 (2018).
[46] J. Ahn, Z. Xu, J. Bang, Y.-H. Deng, T. M. Hoang, Q. Han, R.-M. Ma, and T. Li, Optically Levitated Nanodumbbell Torsion Balance and GHz Nanomechanical Rotor, Phys. Rev. Lett. **121**, 033603 (2018).
[47] J. Ahn, Z. Xu, J. Bang, P. Ju, X. Gao, and T. Li, Ultrasensitive torque detection with an optically levitated nanorotor, Nat. Nanotechnol. **15**, 89 (2020).
[48] J. Bang, T. Seberson, P. Ju, J. Ahn, Z. Xu, X. Gao, F. Robicheaux, and T. Li, Five-dimensional cooling and nonlinear dynamics of an optically levitated nanodumbbell, Phys. Rev. Res. **2**, 043054 (2020).
[49] J. Schäfer, H. Rudolph, K. Hornberger, and B. A. Stickler, Cooling Nanorotors by Elliptic Coherent Scattering, Phys. Rev. Lett. **126**, 163603 (2021).
[50] F. van der Laan, F. Tebbenjohanns, R. Reimann, J. Vijayan, L. Novotny, and M. Frimmer, Sub-Kelvin Feedback Cooling and Heating Dynamics of an Optically Levitated Librator, Phys. Rev. Lett. **127**, 123605 (2021).
[51] Y. Jin, J. Yan, S. J. Rahman, J. Li, X. Yu, and J. Zhang, 6 GHz hyperfast rotation of an optically levitated nanoparticle in vacuum, Photonics Res. **9**, 1344 (2021).
[52] T. Delord, P. Huillery, L. Nicolas, and G. Hétet, Spin-cooling of the motion of a trapped diamond, Nature **580**, 56 (2020).
[53] T. Delord, P. Huillery, L. Schwab, L. Nicolas, L. Lecordier, and G. Hétet, Ramsey Interferences and Spin Echoes from Electron Spins Inside a Levitating Macroscopic Particle, Phys. Rev. Lett. **121**, 053602 (2018).
[54] D. C. Moore and A. A. Geraci, Searching for new physics using optically levitated sensors, Quantum Sci. Technol. **6**, 014008 (2021).
[55] C. C. Rusconi, V. Pöchhacker, K. Kustura, J. I. Cirac, and O. Romero-Isart, Quantum Spin Stabilized Magnetic Levitation, Phys. Rev. Lett. **119**, 167202 (2017).
[56] B. A. Stickler, B. Papendell, S. Kuhn, B. Schrinski, J. Millen, M. Arndt, and K. Hornberger, Probing macroscopic quantum superpositions with nanorotors, New J. Phys. **20**, 122001 (2018).
[57] Y. Ma, K. E. Khosla, B. A. Stickler, and M. Kim, Quantum Persistent Tennis Racket Dynamics of Nanorotors, Phys. Rev. Lett. **125**, 053604 (2020).
[58] R. Kaltenbaek, M. Arndt, M. Aspelmeyer, P. F. Barker, A. Bassi, J. Bateman, A. Belenchia, J. Bergé, S. Bose, C. Braxmaier, *et al.*, MAQRO–BPS 2023 research campaign whitepaper, ArXiv:2202.01535 (2022).
[59] L. Tian, P. Rabl, R. Blatt, and P. Zoller, Interfacing Quantum-Optical and Solid-State Qubits, Phys. Rev. Lett. **92**, 247902 (2004).
[60] A. S. Sørensen, C. H. van der Wal, L. I. Childress, and M. D. Lukin, Capacitive Coupling of Atomic Systems to Mesoscopic Conductors, Phys. Rev. Lett. **92**, 063601 (2004).
[61] L. Martinetz, K. Hornberger, and B. A. Stickler, Electric trapping and circuit cooling of charged nanorotors, New J. Phys. **23**, 093001 (2021).
[62] D. An, A. M. Alonso, C. Matthiesen, and H. Häffner, Coupling Two Laser-Cooled Ions via a Room-Temperature Conductor, Phys. Rev. Lett. **128**, 063201 (2022).
[63] A. Negretti, P. Treutlein, and T. Calarco, Quantum computing implementations with neutral particles, Quantum Inf. Process. **10**, 721 (2011).
[64] G. Kurizki, P. Bertet, Y. Kubo, K. Mølmer, D. Petrosyan, P. Rabl, and J. Schmiedmayer, Quantum technologies with hybrid systems, PNAS **112**, 3866 (2015).
[65] C. D. Bruzewicz, J. Chiaverini, R. McConnell, and J. M. Sage, Trapped-ion quantum computing: Progress and challenges, Appl. Phys. Rev. **6**, 021314 (2019).
[66] K. R. Brown, J. Chiaverini, J. M. Sage, and H. Häffner, Materials challenges for trapped-ion quantum computers, Nat. Rev. Mater. **6**, 892 (2021).
[67] D. J. Wineland, C. Monroe, W. M. Itano, D. Leibfried, B. E. King, and D. M. Meekhof, Experimental issues in coherent quantum-state manipulation of trapped atomic ions, J. Res. Natl. Inst. Stand. Technol. **103**, 259 (1998).
[68] D. Leibfried, R. Blatt, C. Monroe, and D. Wineland, Quantum dynamics of single trapped ions, Rev. Mod. Phys. **75**, 281 (2003).
[69] D. Hite, Y. Colombe, A. C. Wilson, D. Allcock, D. Leibfried, D. Wineland, and D. Pappas, Surface science for improved ion traps, MRS Bull. **38**, 826 (2013).
[70] C. Monroe and J. Kim, Scaling the ion trap quantum processor, Science **339**, 1164 (2013).
[71] M. Brownnutt, M. Kumph, P. Rabl, and R. Blatt, Ion-trap measurements of electric-field noise near surfaces, Rev. Mod. Phys. **87**, 1419 (2015).
[72] P. Sonnentag and F. Hasselbach, Measurement of Decoherence of Electron Waves and Visualization of the Quantum-Classical Transition, Phys. Rev. Lett. **98**, 200402 (2007).
[73] P. J. Beierle, L. Zhang, and H. Batelaan, Experimental test of decoherence theory using electron matter waves, New J. Phys. **20**, 113030 (2018).
[74] N. Kerker, R. Röpke, L.-M. Steinert, A. Pooch, and A. Stibor, Quantum decoherence by Coulomb interaction, New J. Phys. **22**, 063039 (2020).
[75] J. Anglin, J. Paz, and W. Zurek, Deconstructing decoherence, Phys. Rev. A **55**, 4041 (1997).
[76] P. Machnikowski, Theory of which path dephasing in single electron interference due to trace in conductive environment, Phys. Rev. B **73**, 155109 (2006).
[77] A. Howie, Mechanisms of decoherence in electron microscopy, Ultramicroscopy **111**, 761 (2011).
[78] A. Safavi-Naini, P. Rabl, P. Weck, and H. Sadeghpour, Microscopic model of electric-field-noise heating in ion traps, Phys. Rev. A **84**, 023412 (2011).
[79] A. Safavi-Naini, E. Kim, P. Weck, P. Rabl, and H. Sadeghpour, Influence of monolayer contamination on electric-field-noise heating in ion traps, Phys. Rev. A **87**, 023421 (2013).

[80] E. Kim, A. Safavi-Naini, D. Hite, K. McKay, D. Pappas, P. Weck, and H. Sadeghpour, Electric-field noise from carbon-adatom diffusion on a Au (110) surface: First-principles calculations and experiments, Phys. Rev. A **95**, 033407 (2017).

[81] V. Sandoghdar, C. Sukenik, E. Hinds, and S. Haroche, Direct Measurement of the van der Waals Interaction Between an Atom and Its Images in a Micron-Sized Cavity, Phys. Rev. Lett. **68**, 3432 (1992).

[82] Q. A. Turchette, B. King, D. Leibfried, D. Meekhof, C. Myatt, M. Rowe, C. Sackett, C. Wood, W. Itano, C. Monroe, *et al.*, Heating of trapped ions from the quantum ground state, Phys. Rev. A **61**, 063418 (2000).

[83] R. Dubessy, T. Coudreau, and L. Guidoni, Electric field noise above surfaces: A model for heating-rate scaling law in ion traps, Phys. Rev. A **80**, 031402 (2009).

[84] G. H. Low, P. F. Herskind, and I. L. Chuang, Finite-geometry models of electric field noise from patch potentials in ion traps, Phys. Rev. A **84**, 053425 (2011).

[85] C. Noel, M. Berlin-Udi, C. Matthiesen, J. Yu, Y. Zhou, V. Lordi, and H. Häffner, Electric-field noise from thermally activated fluctuators in a surface ion trap, Phys. Rev. A **99**, 063427 (2019).

[86] J. M. Wylie and J. Sipe, Quantum electrodynamics near an interface, Phys. Rev. A **30**, 1185 (1984).

[87] S. Y. Buhmann, M. Tarbutt, S. Scheel, and E. Hinds, Surface-induced heating of cold polar molecules, Phys. Rev. A **78**, 052901 (2008).

[88] S. Scheel and S. Y. Buhmann, Path decoherence of charged and neutral particles near surfaces, Phys. Rev. A **85**, 030101 (2012).

[89] M. Kumph, C. Henkel, P. Rabl, M. Brownnutt, and R. Blatt, Electric-field noise above a thin dielectric layer on metal electrodes, New J. Phys. **18**, 023020 (2016).

[90] M. Teller, D. A. Fioretto, P. C. Holz, P. Schindler, V. Messerer, K. Schüppert, Y. Zou, R. Blatt, J. Chiaverini, J. Sage, *et al.*, Heating of a Trapped Ion Induced by Dielectric Materials, Phys. Rev. Lett. **126**, 230505 (2021).

[91] S. Y. Buhmann, *Dispersion Forces I—Macroscopic Quantum Electrodynamics and Ground-State Casimir, Casimir-Polder and van der Waals Forces* (Springer, Berlin, 2012).

[92] S. Y. Buhmann, *Dispersion Forces II—Many-Body Effects, Excited Atoms, Finite Temperature and Quantum Friction* (Springer, Berlin, 2012).

[93] P. C. Holz, K. Lakhmanskiy, D. Rathje, P. Schindler, Y. Colombe, and R. Blatt, Electric field noise in a high-temperature superconducting surface ion trap, Phys. Rev. B **104**, 064513 (2021).

[94] B.-S. K. Skagerstam, U. Hohenester, A. Eiguren, and P. K. Rekdal, Spin Decoherence in Superconducting Atom Chips, Phys. Rev. Lett. **97**, 070401 (2006).

[95] H. Pino, J. Prat-Camps, K. Sinha, B. P. Venkatesh, and O. Romero-Isart, On-chip quantum interference of a superconducting microsphere, Quantum Sci. Technol. **3**, 025001 (2018).

[96] K. Sinha and Y. Subaşı, Quantum Brownian motion of a particle from Casimir-Polder interactions, Phys. Rev. A **101**, 032507 (2020).

[97] S. Botti, A. Schindlmayr, R. Del Sole, and L. Reining, Time-dependent density-functional theory for extended systems, Rep. Prog. Phys. **70**, 357 (2007).

[98] Y. Ping, D. Rocca, and G. Galli, Electronic excitations in light absorbers for photoelectrochemical energy conversion: First principles calculations based on many body perturbation theory, Chem. Soc. Rev. **42**, 2437 (2013).

[99] B. L. Foulon, K. G. Ray, C.-E. Kim, Y. Liu, B. M. Rubenstein, and V. Lordi, $1/\omega$ electric-field noise in surface ion traps from correlated adsorbate dynamics, Phys. Rev. A **105**, 013107 (2022).

[100] S. Scheel and S. Y. Buhmann, Macroscopic quantum electrodynamics—concepts and applications, Acta Phys. Slovaca **58**, 675 (2008).

[101] H.-P. Breuer and F. Petruccione, *The Theory of Open Quantum Systems* (Oxford University Press, Oxford, England, 2002).

[102] J. D. Jackson, *Classical Electrodynamics* (Wiley, New York, 1999).

[103] F. London and H. London, The electromagnetic equations of the supraconductor, Proc. R. Soc. A: Math. Phys. Eng. Sci. **149**, 71 (1935).

[104] U. Hohenester, A. Eiguren, S. Scheel, and E. Hinds, Spin-flip lifetimes in superconducting atom chips: Bardeen-Cooper-Schrieffer versus Eliashberg theory, Phys. Rev. A **76**, 033618 (2007).

[105] C. Henkel, S. Pötting, and M. Wilkens, Loss and heating of particles in small and noisy traps, Appl. Phys. B **69**, 379 (1999).

[106] Note however that the quasistatic approximation of the electric field emanating from the metal ceases to be valid for distances larger than the skin depth δ, with $\delta^2 = c^2\gamma_m/\omega\omega_{\mathrm{pm}}^2$ [89,105].

[107] A. K. Jonscher, The 'universal' dielectric response, Nature **267**, 673 (1977).

[108] T. Delord, L. Nicolas, L. Schwab, and G. Hétet, Electron spin resonance from NV centers in diamonds levitating in an ion trap, New J. Phys. **19**, 033031 (2017).

[109] P. Nagornykh, J. E. Coppock, J. P. Murphy, and B. Kane, Optical and magnetic measurements of gyroscopically stabilized graphene nanoplatelets levitated in an ion trap, Phys. Rev. B **96**, 035402 (2017).

[110] D. S. Bykov, P. Mestres, L. Dania, L. Schmöger, and T. E. Northup, Direct loading of nanoparticles under high vacuum into a Paul trap for levitodynamical experiments, Appl. Phys. Lett. **115**, 034101 (2019).

[111] F. Tebbenjohanns, M. Frimmer, A. Militaru, V. Jain, and L. Novotny, Cold damping of an Optically Levitated Nanoparticle to Microkelvin Temperatures, Phys. Rev. Lett. **122**, 223601 (2019).

[112] G. P. Conangla, F. Ricci, M. T. Cuairan, A. W. Schell, N. Meyer, and R. Quidant, Optimal Feedback Cooling of a Charged Levitated Nanoparticle with Adaptive Control, Phys. Rev. Lett. **122**, 223602 (2019).

[113] H.-P. Breuer, E.-M. Laine, J. Piilo, and B. Vacchini, Colloquium: Non-Markovian dynamics in open quantum systems, Rev. Mod. Phys. **88**, 021002 (2016).

[114] W. B. Westphal and A. Sils, Dielectric constant and loss data, MIT Technical Report AFML-74-250, Part III, 1977.

[115] B. Papendell, B. A. Stickler, and K. Hornberger, Quantum angular momentum diffusion of rigid bodies, New J. Phys. **19**, 122001 (2017).

[116] M. Papič and I. de Vega, Neural-network-based qubit-environment characterization, Phys. Rev. A **105**, 022605 (2022).

[117] R. McConnell, C. Bruzewicz, J. Chiaverini, and J. Sage, Reduction of trapped-ion anomalous heating by in situ surface plasma cleaning, Phys. Rev. A **92**, 020302 (2015).

[118] D. A. Hite, Y. Colombe, A. C. Wilson, K. R. Brown, U. Warring, R. Jördens, J. D. Jost, K. McKay, D. Pappas, D. Leibfried, *et al.*, 100-Fold Reduction of Electric-Field Noise in an Ion Trap Cleaned with In Situ Argon-Ion-Beam Bombardment, Phys. Rev. Lett. **109**, 103001 (2012).

[119] J. Gieseler, A. Kabcenell, E. Rosenfeld, J. Schaefer, A. Safira, M. J. Schuetz, C. Gonzalez-Ballestero, C. C. Rusconi, O. Romero-Isart, and M. D. Lukin, Single-Spin Magnetomechanics with Levitated Micromagnets, Phys. Rev. Lett. **124**, 163604 (2020).

[120] A. Vinante, P. Falferi, G. Gasbarri, A. Setter, C. Timberlake, and H. Ulbricht, Ultralow Mechanical Damping with Meissner-Levitated Ferromagnetic Microparticles, Phys. Rev. Appl. **13**, 064027 (2020).

[121] K. Streltsov, J. S. Pedernales, and M. B. Plenio, Ground-State Cooling of Levitated Magnets in Low-Frequency Traps, Phys. Rev. Lett. **126**, 193602 (2021).

[122] M. G. Latorre, A. Paradkar, D. Hambraeus, G. Higgins, and W. Wieczorek, A chip-based superconducting magnetic trap for levitating superconducting microparticles, IEEE Trans. Appl. Supercond. **32**, 1 (2022).

[123] C. Caloz and Z.-L. Deck-Léger, Spacetime metamaterials—part I: General concepts, IEEE Trans. Antennas Propag. **68**, 1569 (2019).

[124] C. Caloz and Z.-L. Deck-Leger, Spacetime metamaterials—part II: Theory and applications, IEEE Trans. Antennas Propag. **68**, 1583 (2019).

[125] B. A. Stickler, B. Schrinski, and K. Hornberger, Rotational Friction and Diffusion of Quantum Rotors, Phys. Rev. Lett. **121**, 040401 (2018).

[126] C. Gardiner and P. Zoller, *Quantum Noise: A Handbook of Markovian and non-Markovian Quantum Stochastic Methods with Applications to Quantum Optics* (Springer Science & Business Media, Luxembourg, 2004).

[127] M. Kleefstra and G. Herman, Influence of the image force on the band gap in semiconductors and insulators, J. Appl. Phys. **51**, 4923 (1980).

[128] B. A. Stickler, B. Papendell, and K. Hornberger, Spatio-orientational decoherence of nanoparticles, Phys. Rev. A **94**, 033828 (2016).

[129] L. Martinetz, Ph.D. thesis, University of Duisburg-Essen, 2022 (to be published).

[130] K. Hornberger, Monitoring approach to open quantum dynamics using scattering theory, Europhys. Lett. **77**, 50007 (2007).